Institute for Theoretical Physics, University of Wrocław

European Organization For Nuclear Research
CERN - AB Department

# Beam Dynamics in the Muon Front End of a Neutrino Factory



Doctoral thesis by:
Jarosław Pasternak

Supervisors:
Dr B. Autin, CERN
Prof. dr hab. J. Sobczyk, UWr

Wrocław, Poland
23. 12. 2004

**Abstract**

The general concept of the neutrino factory is discussed and the fundamental tools in accelerator physics are introduced. The beam dynamics in the muon front end is extensively discussed with particular attention to the application of concepts like RF phase rotation, magnetic bunch compression, bunching and ionization cooling. Examples of front end designs based on these methods are presented.

*Martusi, Hubercikowi, Karolkowi*

# Contents

# List of Symbols

$\Delta m^2_{ij}$ - the mass squared difference between the ith and the jth neutrino mass eigenstates.
$U_{fm}$ - the Makki, Nakagawa and Sakata (MSN)neutrino mixing matrix.
$P(\nu_f \rightarrow \nu_g)$ - the probability of the neutrino oscillation from neutrino with the $f$ flavor state into a neutrino with the $g$ flavor state.
$L_{osc}$ - the neutrino oscillation wave-length.
$\theta_{ij}$ - the neutrino mixing angle.
$s_{ij}$ , $c_{ij}$ - $sin\theta_{ij}$ and $cos\theta_{ij}$ the parameters in the MSN mixing matrix.
$\delta_{CP}$ - the CP violating phase in the MSN matrix.
$f_o(\bar{x})$ and $f_1(\bar{x})$ - the flux functions in muon decay.
$P$ - the muon polarization.
$\theta$ - the angle between the neutrino momentum vector and the muon spin direction in the muon rest frame.
J - the Jarlskog determinant.
$\mathcal{L}_M$ - the Maxwell Lagrangian.
$m_{0,\pi,\mu}$ - the rest mass of (a particle, pion, muon).
c - the speed of light in vacuum.
$\vec{r}(x, y, z)$ - the particle position vector.
$\vec{v}(x, y, z)$ - the particle speed vector.
e - the elementary charge.
$\vec{A}$ - the electromagnetic vector potential.
$\phi$ - the electromagnetic scalar potential.
$\vec{p_c}$ - the canonical momentum of a particle.
$\vec{p}$ - the mechanical momentum of a particle.
$\gamma$ - the relativistic gamma factor of a particle.
$\beta$ - the vector of relativistic beta factors $(\beta_x, \beta_y, \beta_z)$ of a particle.
$\mathcal{H}_M$ - the Maxwell Hamiltonian.
$E_{tot}$ - the total energy of a particle.
$p_{ic}$, $q_{ic}$ and $P_{ic}$ , $Q_{ic}$ - the old and new generalized coordinates before and after the canonical transformation.
$\mathcal{K}_M$ - the new Hamiltonian after the canonical transformation.
$k(\vec{s})$ - the curvature vector.
k - the absolute value of curvature vector.
$\rho$ - the radius of curvature of a particle path.
$u_1$, $u_2$ and $u_3$ - the unit vectors defining the Frenet basis.

$\mathcal{H}_{\mathcal{CS}M}$ - the Courant-Snyder Hamiltonian.
$F_L$ - the Lorentz force.
$\vec{B}$ - the magnetic field vector.
$\vec{E}$ - the electric field vector.
K - the quadrupole focusing strenth.
m - the sextupole focusing strenth.
C, S , C', S' - cosine-like, sine-like transfer matrix elements and their derivatives with respect to s.
$\alpha_x$, $\beta_x$, $\gamma_x$ - the Twiss functions.
$\mu$, $\mu_0$ - the betatron phase and its initial value.
$\nu$ , $Q$ - the tune.
$\epsilon$, $\epsilon_x$, $\epsilon_y$, $\epsilon_t$, $\epsilon_l$, $\epsilon_n$ - the emittance (horizontal, vertical, transverse, longitudinal, normalized)
$D_1$, $D_1'$ - dispersion driving matrix elements in the $3 \times 3$ tranfer matrix
D, D', $D_x$, $D_x'$, $D_y$, $D_y'$ - the dispersion function and its derivative, horizontal, vertical.
$\gamma_T$ - the gamma transition factor.
$\alpha_c$ - the momentum compaction factor.
T - the revolution time (time of passage).
f - the focusing length.
g - the quadrupole gradient.
$l_q$ - the quadrupole length.
$\phi_L$ - the Larmor angle.
$\phi$, $\phi_s$ - the synchrotron phase, the synchronous phase ( the synchrotron phase for the synchronous particle).
W - the kinetic energy.
$f_{RF}$, $\omega_{RF}$ - the RF frequency.
h - the harmonic number.
$\beta_s$, $\gamma_s$ - the relativistic fators for synchronous particle.
$T_t$ -the transit time factor.
$\Lambda_s$ - the sychrotron wavelength.
$\Omega_s$ - the sychrotron frequency.
$\zeta$, $\zeta_x$ - chromaticity, horizontal chromaticity.
$T_{RF}$ - the synchrotron period.
$\tau_\pi$, $\tau_\mu$ - pion, muon lifetime.
$E_1$, $P_1$ - pion decay factors.
$X_0$ - radiation length
d - absorber thickness.

$P^A$, $P^{RF}$, $P^W$ - the absorber, RF cavities, wedge absorbers packing factors.
$T_c$ - the cooling time.
$L_c$ - the cooling length.
$\delta'$ - the wedge absorber angle.
$\Psi$ - the kicker angle.
$B_{4D}$ - 4D brightness.
$B_a(\phi_s)$ - the bucket area as a function of synchronous phase.

# Chapter 1

# Introduction

The neutrino factory was proposed as a laboratory for precise neutrino oscillation physics. In particular, the measurement of leptonic CP violation can be addressed by neutrino factory experiments. In chapter 2 we briefly describe neutrino oscillation physics, methods of measurement in the neutrino factory and the general concept of the machine. The theory of accelerator physics is introduced in chapters 3, 4 and 5. The input muon beam and definition of the muon front end are the subjects of chapter 6. Longitudinal bunch manipulations such as phase rotation, magnetic compression and bunching are extensively discussed in chapter 7. The ionization cooling theory and two examples of the cooler ring design are presented in chapter 8. A comparison of various scenarios for the muon front end design is carried out in chapter 9. The conclusions are given in chapter 10.

The core of the thesis starts with chapter 6. The main results are: a proposal of the front end with bunching (section 7.9) and a proposal for front end based on the bunch-to-bucket principle (section 9.3) with cooling ring (section 8.4).

# Chapter 2

# Towards a leptonic CP violation

Neutrinos are perhaps the most interesting and simultaneously mysterious elementary particles in modern physics. The discoveries of the neutrino oscillation phenomenon reported by SuperKamiokande [1], SNO [2], KamLand [3] and many other experiments opened a new era in particle physics. The CP violation in the leptonic sector is the next question to address in future oscillation experiments.

## 2.1 Neutrino oscillation phenomenon

Experiments confirmed the mixed nature of the neutrino, which can be formulated in the following way: the neutrino of given flavor state is a quantum mechanical superposition of states with definite masses ($\hbar = c = 1$):

$$|\nu_f >= \sum_m U_{fm} |\nu_m >, \tag{2.1}$$

where $|\nu_f >$ are flavor eigenstates, which are produced or detected via weak interaction, $|\nu_m >$ are mass eigenstates and $U_{fm}$ is the neutrino mixing matrix. The oscillation phenomenon happens when a neutrino produced in a given flavor state, changes its flavor in flight towards the detector, where it is observed with a different flavor state. The time dependence of a state can be described by:

$$|\nu_f(t) >= \sum_m e^{-iE_m t} U_{fm} |\nu_m > . \tag{2.2}$$

Then the amplitude of transformation into another flavor state is, using the orthogonality of mass eigenstates:

$$< \nu_g | \nu_f(t) >= \sum_m e^{-iE_m t} U_{fm} U^*_{gm}. \tag{2.3}$$

The probability of oscillation is given by the formula [4]:

$$P(f \to g) = \sum_m |U^*_{fm}|^2 |U_{gm}|^2 + 2Re[\sum_{m \neq n} U^*_{fm} U_{gm} U_{fn} U^*_{gn} cos(\frac{\Delta m^2_{mn} t}{2p})], \tag{2.4}$$

where the ultrarelativistic approximation was used:

$$E_m \simeq p_m + \frac{m^2_m}{2p_m}. \tag{2.5}$$

It is also assumed that:

$$p_m \simeq p_n \tag{2.6}$$

and $\delta m^2_{mn}$ in equation (4) is given by:

$$\Delta m^2_{mn} = m^2_m - m^2_n. \tag{2.7}$$

The distance at which the argument of $cos(\frac{\delta m^2_{mn} t}{2E})$ becomes $2\pi$ - is the oscillation length:

$$L_{osc} = \frac{4\pi E}{\Delta m^2_{mn}} \tag{2.8}$$

In the two generation case where the mixing matrix U is written:

$$\begin{pmatrix} cos\theta & sin\theta \\ -sin\theta & cos\theta \end{pmatrix}, \tag{2.9}$$

the probability of oscillation from flavor state f to g is:

$$P(f \to g) = sin^2(2\theta) sin^2(\frac{\pi L}{L_{osc}}), \tag{2.10}$$

where the time was replaced by the distance $L$ traveled by the beam.

## 2.2 CP violation

In the three generation case the mixing matrix U - (the Maki, Nagakawa, Sakata matrix [5]) can be written in the following way:

$$U = \begin{pmatrix} 1 & 0 & 0 \\ 0 & c_{23} & s_{23} \\ 0 & -s_{23} & c_{23} \end{pmatrix} \begin{pmatrix} c_{13} & 0 & s_{13}e^{i\delta} \\ 0 & 1 & 0 \\ -s_{13}e^{i\delta} & s_{23} & c_{13} \end{pmatrix} \begin{pmatrix} c_{12} & s_{12} & 0 \\ -s_{12} & c_{12} & 0 \\ 0 & 0 & 1 \end{pmatrix} \quad (2.11)$$

where $s(c)_{ij}$ is $sin(cos)\theta_{ij}$. The presence of the phase $\delta$ different from zero introduces a CP violation phenomenon in the neutrino oscillation. The CP violation in the quark sector is described in a similar way using the CKM matrix.

In the case of neutrino oscillation the CP violation means:

$$P(f \to g) \neq P(\bar{f} \to \bar{g}) \quad (2.12)$$

To observe the CP violation two experiments need to be performed with different initial neutrino beam polarities.

It was proposed to produce such beams in various ways:
1. Conventional neutrino beams based on pion decay [6]:

protons $\to$ target $\to \pi^{\pm} \to$charge selection in the horn and focusing $\to \nu_\mu$ or $\bar{\nu_\mu}$

2. Neutrino beams from $\beta$ decay of radioactive ions (a "beta beam") [7]:

protons $\to$ target $\to$creation of ion beam $\to$ stacking $\to$ acceleration $\to$ ion decay ring $\to \nu_e$ or $\bar{\nu_e}$

3. Neutrino beams from muon decay (a neutrino factory) [8, 10, 9]:

protons $\to$ target $\to \pi^{\pm} \to$ creation of $\mu^+$ or $\mu^-$ beam $\to$ acceleration $\to \mu$ decay ring $\to \bar{\nu_\mu}\nu_e$ or $\nu_\mu\bar{\nu_e}$

## 2.3 Conceptual idea of a neutrino factory

We shall focus on the concept of a neutrino factory.

The neutrino factory is a complex, in which a muon beam is created and accelerated to high energy (typically 20 - 50 GeV). The muon beam at the final energy is then injected into a storage ring with long straight sections (about 60 % of the ring circumference) pointing towards far detectors located from hundreds to several thousands km (in present proposals [12]) from the decay ring. The use of a decay ring instead of a straight decay channel can be immediately understood, realizing that muons accelerated to momentum 20 GeV/c have a decay length $\gamma c\tau = 126$ km. The geometry of the decay ring favors a concept of two baseline experiments run at different distances at the same time.

Muon decay $\mu^{\pm} \rightarrow e^{\pm} + \nu_e(\bar{\nu_e}) + \bar{\nu_\mu}(\nu_\mu)$ is one of the best measured processes in particle physics. Neutrino beam characteristics can be known with great precision from the distribution of neutrinos, which in the muon rest frame is given by [9]:

$$\frac{d^2N}{dxd\Omega} = \frac{1}{4\pi}(f_0(x) \pm Pf_1(x)cos\theta) \tag{2.13}$$

where $x = 2E_\nu/m_\mu$, $P$ is the muon beam polarization in the decay ring with respect to the beam line and $\theta$ is an angle between the neutrino momentum vector and the muon spin direction. The sign depends on the beam polarity, "-" for $\mu^+$ and "+" for $\mu^-$. The polarization of the muon beam depends on details of the design of muon lines. It can be measured precisely by observation of electron or positron polarization coming from $\mu^{\pm}$ decay in the decay ring. The table 2.1 gives the flux functions for electron and muon (anti)neutrinos:

| | $f_0(x)$ | $f_1(x)$ |
|---|---|---|
| $\nu_\mu$ | $2x^2(3-2x)$ | $2x^2(1-2x)$ |
| $\nu_e$ | $12x^2(1-x)$ | $12x^2(1-x)$ |

Table 2.1: Flux functions for electron and muon (anti)neutrinos.

Precise information on the neutrino beam contamination and the flux is a great advantage of the neutrino factory in comparison to the conventional neutrino beams from $\pi$ decay, where flux uncertainties are governed by limited knowledge of hadron production cross sections.

In the laboratory frame the neutrino beam is contained in the cone along the decay line. The angle of the cone depends on the parameters characterizing the boost from the laboratory frame to the muon rest frame. The cone angle is proportional to $1/\gamma_\mu$, which dictates a high muon storage energy. Another motivation to store muons at high energy in the decay ring is a fact that the divergence of the muon beam, which in addition contributes to the neutrino cone angle decreases with energy. Finaly, the neutrino interaction cross section increases with energy.

## 2.4 "Golden" observable in a neutrino factory

The basic observable in the experiment with a neutrino factory beam can be defined in the following way. Let's assume, that we store the $\mu^+$ in the decay ring first. We produce a beam with electron neutrinos and muon antineutrinos. If electron neutrinos oscillate into muon neutrinos, we shall see, due to charge current interaction, $\mu^-$ in a far detector. The muon antineutrino from the same beam, which did not change the flavor, would produce $\mu^+$ in a far detector. The oscillation signature is therefore an observation of the so called "wrong sign muons" in the far detector with respect to the sign of stored muons in the decay ring. This is called the "golden" channel. A neutrino far detector, a multi kT device, has to have a muon charge identification capability. To observe the CP violation we have to perform two runs with positive and negative muon beam polarities. The sensitive observable is the ratio:

$$A_{CP} = \frac{N(\mu^-)/N_0(e^-) - N(\mu^+)/N_0(e^+)}{N(\mu^-)/N_0(e^-) + N(\mu^+)/N_0(e^+)} \tag{2.14}$$

where the signs depend on the beam polarity, $N(\mu^\pm)$ is the number of wrong sign muons and $N(e^\pm)$ is the number of expected charge current events created in the far detector by electron (anti)neutrinos in the absence of oscillations.

It can be shown, that it is possible to expand the formula for the probability of oscillation in vacuum with small parameters:

$$P(\nu_e(\bar{\nu_e}) \to \nu_\mu(\bar{\nu_\mu})) = s^2_{23} sin^2 2\theta_{13} sin(\frac{\Delta_{13}L}{2}) + c^2_{23} sin^2 2\theta_{12} sin(\frac{\Delta_{12}L}{2})$$

$+\text{Jcos}(\pm\delta - \frac{\Delta_{13}L}{2})\frac{\Delta_{12}L}{2}sin(\frac{\Delta_{13}L}{2})$, (2.15)

where $\Delta_{ij} = \frac{\Delta m^2_{ij}}{2E_\nu}$ and $J = c_{13}sin2\theta_{12}sin2\theta_{23}sin2\theta_{13}$ is equivalent to the Jarlskog determinant in the quark sector. We can see that the CP odd term in the above formula vanishes if the Jarlskog determinant is equal to zero.

According to current experimental knowledge $s_{13}$ is very small, but all other parameters are comparable with unity. This means that observation of CP violation will be impossible if this parameter is much smaller than the Chooz limit. Both $s_{13}$ and CP violating phase $\delta$ can be studied in the neutrino factory simultaneously but the degeneracies in solution space must be resolved. This is believed to be possible with more than one baseline and the study of other channels than the "golden" channel. It should be mentioned that "matter effect" is asymmetric with respect to beam polarity, because interaction is different for (anti)neutrinos and matter in the Earth contains no antiparticles. The MSW effect has to be taken into account for a CP violation search in the leptonic sector [12].

## 2.5 Building blocks of a neutrino factory

The neutrino factory facility requires several accelerator and particle physics installations.

The requirements for a neutrino factory are the following:

- A proton driver, with multi-MW proton beam power and a specific beam time structure to meet the requirements of injection into a decay ring. This basically means that muon beam has to be shorter than the revolution time in the decay ring. The pulse duration of a linac in order to produce enough intensity is in the ms range. A short proton pulse compatible with decay ring operation needs proton accumulation. Application of $H^-$ ions in the linac, followed by charge exchange injection into an accumulator ring was proposed as a solution for accumulation. Typically, several hundreds of turns can be injected into an accumulator ring. Accumulation is usually followed by bunch compression [14], in order to produce the short final proton bunches (a few ns) needed at the target, which is necessary to limit the longitudinal emittance of the muon beam produced by $\pi$ decay.

  At CERN there are several schemes:

  1. The SPL (Superconducting Proton Linac) option [13]:

$H^-$ linac ( SPL ) to 2.2 GeV $\rightarrow$ proton accumulator ring $\rightarrow$ proton compressor ring $\rightarrow$ target.
2. The RCS (Rapid Cycling Synchrotron) option [14]:
$H^-$ linac to 150 MeV $\rightarrow$ proton accumulation in the synchrotron $\rightarrow$ acceleration and compression in a synchrotron or a chain of synchrotrons $\rightarrow$ target.

The proton driver is a separate accelerator facility which can be used for other purposes than neutrino production.

- A target system and pion capture including pion decay channel.
  The target is a difficult part of the machine. It has to operate with 4 MW proton beam power and absorb a minimal pion flux. The compromise between pion production and reabsorption dictates the target size to be one to two interaction lengths in the longitudinal dimension and about 1 cm in the radial one. This means that energy deposition in this kind of target is beyond the specifications of present proton targets. There exist several proposals and we mention two of them:
  1. Liquid mercury jet target [15].
  2. Tantalum beads cooled by gaseous or liquid helium [16].

  There are several proposals for the pion capture system:
  1. A 10-20 T solenoid located around the target followed by an adiabatic section, where the field is slowly reduced in the decay channel [17, 18].
  2. A target installed in the magnetic horn (operating at 50 Hz) matched to the decay solenoid with constant solenoidal field in the decay channel [19].
  3. A system consisting of several targets in magnetic horns followed by an alternating gradient funneling system [41].

  Issues related to activation problems and a primary proton beam dump are still under discussion.

- Muon front end.
  This part of a neutrino factory captures muons coming from the decay channel and prepares the muon beam for acceleration. The manipulation used here can be: bunching, debunching, phase rotation, magnetic compression and ionization cooling. Problems of muon front end are addressed in the rest of this work.

- Muon accelerator chain. The short muon life time imposes a very fast acceleration. A conventional synchrotron cannot be used because of the limited speed of magnetid field ramp and linear acceleration can be used only to a limited extent because of the cost. Two proposals can meet the goal:
  1. Application of the recirculating accelerators, where linear acceleration is followed by families of RF free arcs, one arc for every energy, which bends the $\mu$ beam back into a linac to enable recirculation [20]. The scheme is limited by the number of arcs which is typically 4 to 5.
  2. The use of the FFAG ( Fixed Field Alternating Gradient) [21] synchrotrons, where the magnetic field is constant in time, but there exist stable orbits over a large energy range. The limitation here lies in the size of the magnets.

- Muon decay ring.
  The geometry and length of the decay ring is a compromise to achieve 2 long straight sections pointing towards far detectors being a large fraction (60 %) of the ring circumference and the strength of the magnetic field in the arcs. The CERN ring is 2 km in circumference [22].

- One or two far detectors with multi-kT mass and muon charge identification capability.

The possible layout of the neutrino factory can be seen in Fig. 2.1.

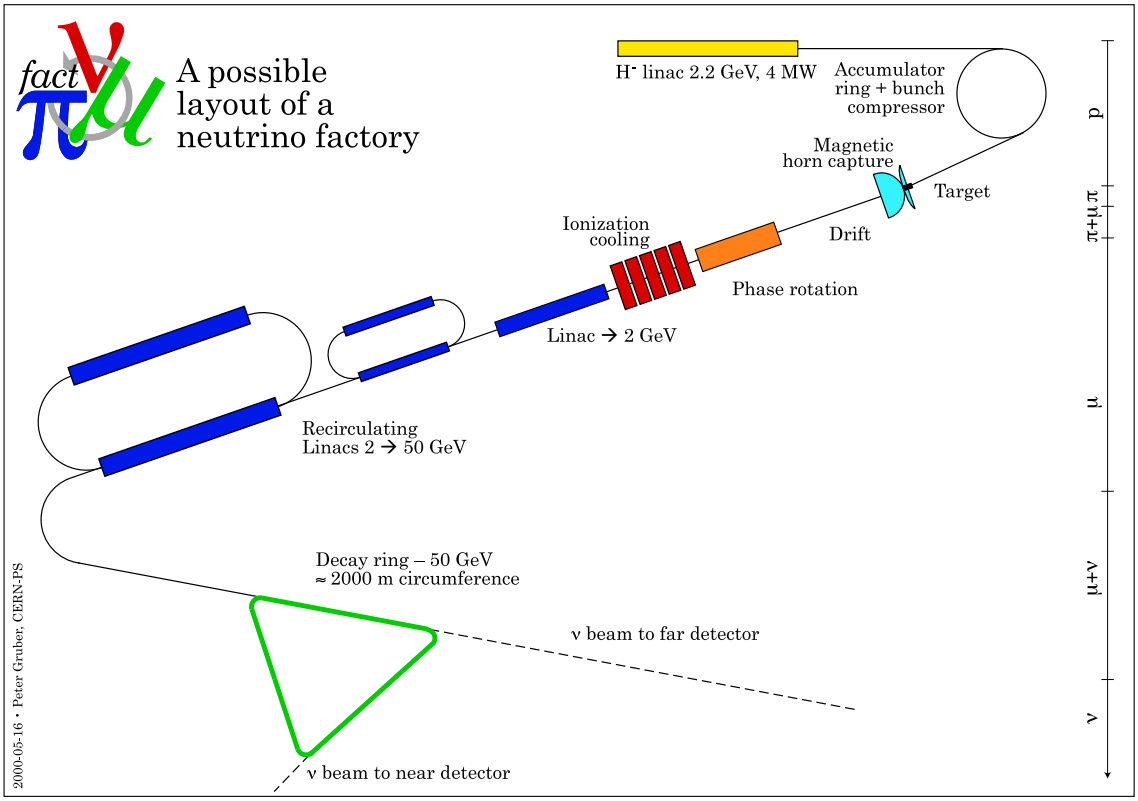


Figure 2.1: The conceptual layout of the CERN Neutrino Factory.

# Chapter 3

# Charged particle dynamics in an accelerator

The purpose of this chapter is to introduce the calculational tools needed to describe single particle dynamics in an accelerator. We shall explain the description of magnetic fields used to guide and focus a charged particle beam.

## 3.1 Lagrangian and Hamiltonian approach to dynamics

We start with the Maxwell Lagrangian of a charged particle with mass $m_0$ in a classical electrodynamic field [23, 24]:

$$\mathcal{L}_M = -m_0 c^2 \sqrt{1 - \frac{\dot{\vec{r}}^2}{c^2}} + \frac{e}{c}\dot{\vec{r}}\vec{A} - e\phi. \tag{3.1}$$

The canonical momentum $\vec{p_c}$ is defined as:

$$\vec{p_c} = \frac{\partial \mathcal{L}_M}{\partial \dot{\vec{r}}} = \vec{p} + \frac{e}{c}\vec{A}$$

where

$$\vec{p} = \gamma m_0 \vec{\beta} c,$$

is the mechanical momentum as can be easily checked by the explicit calculation. The dynamical problem can now be addressed by solving Euler-Lagrange equations:

$$\frac{d}{dt}\frac{\partial \mathcal{L}_M}{\partial \dot{\vec{r}}} - \frac{\partial \mathcal{L}_M}{\partial \vec{r}} = 0.$$

It is nevertheless very convenient to go to the Hamiltonian description of mechanics as it is common in many physical problems. The Hamilton description simplifies the equations of motion and introduces a powerful concept of phase space dynamics. The transformation from Lagrangian to Hamiltonian description is performed by Legendre transformation. Without going into details, we observe, that the Maxwell Hamiltonian is equal to total energy and is related to canonical momentum in the following way:

$$\mathcal{H}_M = \dot{\vec{r}}\vec{p}_c - \mathcal{L}_M = \sqrt{m_0^2c^4 + \vec{p}^2c^2} + e\phi = E_{tot},$$

$$\mathcal{H}_M = \sqrt{m_0^2c^4 + c^2(\vec{p}_c - \frac{e}{c}\vec{A})^2} + e\phi.$$

The dynamical problem is now solved via Hamilton equations:

$$\dot{r_i} = \frac{\partial \mathcal{H}_M}{\partial p_{ci}}, \tag{3.2}$$

$$\dot{p_{ci}} = -\frac{\partial \mathcal{H}_M}{\partial r_i}. \tag{3.3}$$

where i=x, y, z.

## 3.2 Definition of betatron and synchrotron motion

Now we will make several assumptions useful to simplify the dynamics of a charged particle in an accelerator.

Firstly, we will treat a magnetic field as constant in time, which is approximately valid for all existing accelerators. The magnetic field is slowly changing with time, orders of magnitude longer than betatron period; in other words betatron frequency is much higher than the revolution frequency, which is usually orders of magnitude higher than the repetition rate - the

frequency of magnetic field change. It is interesting to note that in the accelerators constructed according to a fixed field alternating gradient (FFAG) principle the magnetic field is constant in time exactly by definition.

The standard accelerator is built with a symmetry plane, which is usually a horizontal plane. The stable closed orbit lies in this plane (called the median plane). The charged particle characterized by a special set of coordinates moves on the closed orbit indefinitely. All other particles with small deviations in position and momentum from the reference particle perform stable oscillations around the reference orbit. Existence of stability of small oscillations is a subject of linear optics. Oscillations in the transverse planes are described by the relative deviation $\delta$x of distance from the reference particle and the component of the momentum $p_T$ perpendicular to a closed orbit. They are called betatron oscillations. The oscillations in the longitudinal plane ($\delta$E, $\delta$t) in the presence of fields in RF (radiofrequency) cavities, which do vary with time are called synchrotron oscillations. In addition a particle with different energy moves on a different orbit in a bending magnet. This effect is described by the dispersion function. We note, that in the case of a linear accelerator (linac), the reference particle moves in a straight line, but magnetic fields still have a median symmetry plane.

## 3.3 Accelerator system of coordinates

It is useful to introduce a curvilinear coordinate system to treat the dynamics in a circular machine or a transfer line containing chicanes. In addition, we will break a paradigm with time being an independent coordinate. In a particular problem of the particle motion in an accelerator lattice, one is more interested in beam properties changing from one sector to the other, than in real time evolution. In addition, time or rather time difference with respect to a reference particle (equivalently RF phase or phase difference with respect to a synchronous particle) is used as a coordinate canonically conjugated to energy difference with respect to the synchronous particle. This suggests treating the curvilinear abscissa $s$ of a closed orbit as an independent coordinate.

We shall transform the dynamical problem in two steps using canonical transformations. Before going into details, let's assume that the RF cavities have been turned off, which corresponds to a beam stored at a fixed mean energy without acceleration or passage through a transfer channel. Mathemat-

ically it corresponds to setting the scalar potential in [3.1] and all following formulas to 0. We will turn on RF cavities later. We define an accelerator system of coordinates in the following way: the position of a reference particle on its closed orbit is established once its position $s$ with respect to some initial value is given (for example from the injection point). To every point on a closed orbit we can attach an orthogonal system of coordinates shown in Fig 3.1.

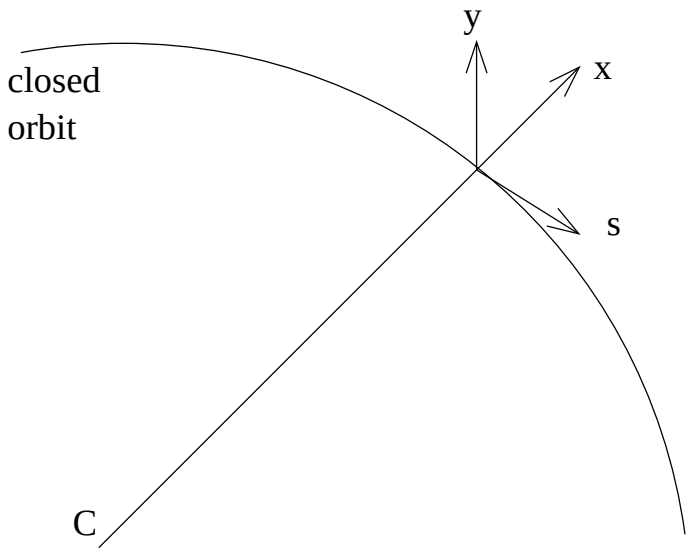


Figure 3.1: Accelerator system of coordinates.

## 3.4 Curvilinear system of coordinates

We shall now transform the Maxwell Hamiltonian to a Courant-Snyder Hamiltonian, which describes a motion in an accelerator system of coordinates. A canonical transformation is a change of generalized coordinates which conserves the Hamiltonian form of the equations of motion. It can be shown [24], that it is automatically fulfilled if the following relation holds:

$$p_{ic}\dot{q_{ic}} - \mathcal{H} = P_{ic}\dot{Q_{ic}} - \mathcal{K} + \frac{dF}{dt} \tag{3.4}$$

where $(q_i, p_i)$ and $(Q_i, P_i)$ are old and new generalized coordinates, and $\mathcal{H}$ and $\mathcal{K}$ are old, and transformed Hamiltonians, respectively. The generating

function F is a function of the phase space coordinates with continuous second derivatives. Let us introduce the unit vectors $(\vec{u_1}, \vec{u_2}, \vec{u_3})$ in the accelerator frame $(x, y, s)$ respectively. Following relations from basic geometry holds:

$$u_1\vec{(s)} = \frac{d\vec{r_0}(s)}{ds}, \tag{3.5}$$

$$k\vec{(s)} = -\frac{d\vec{u_1}(s)}{ds} = -k\vec{u_2}(s), \tag{3.6}$$

$$\vec{u_3} = \vec{u_1} \times \vec{u_2}, \tag{3.7}$$

$$\frac{d\vec{u_2}}{ds} = k\vec{u_1}, \tag{3.8}$$

$$\frac{d\vec{u_3}}{ds} = 0, \tag{3.9}$$

where $\vec{r_o}$ is a position vector of the reference particle calculated from the center of the machine. The curvature of the reference orbit $k$ is related to the radius of curvature $\rho$, the magnetic field in the bending magnet $B$ and momentum $p$ in the following way:

$$k = \frac{1}{\rho} = \frac{eB}{cp}. \tag{3.10}$$

We define a generating function to perform the canonical transformation to the curvilinear coordinate system:

$$F = -\vec{p_c}(\vec{r_0}(s) + x\vec{u_2}(s) + y\vec{u_3}(s)) \tag{3.11}$$

We can define a new set of canonical momenta related to the new coordinates with the help of $F$ [25]:

$$p_{sc} = -\frac{\partial F}{\partial s} = \vec{p_c}(1 + k(s))\vec{u_1}(s), \tag{3.12}$$

$$p_{xc} = -\frac{\partial F}{\partial x} = \vec{p_c}\vec{u_2}(s), \tag{3.13}$$

$$p_{yc} = -\frac{\partial F}{\partial y} = \vec{p_c}\vec{u_3}(s). \tag{3.14}$$

The generating function F given by equation 3.4 is not the explicit function of time. This suggests that we can transform the Hamiltonian expressing all old coordinates with new ones. This defines a new Hamiltonian $\mathcal{H}_F$:

$$\mathcal{H}_F = \sqrt{m_0^2c^4 + c^2(\frac{p_s}{1+k(s)x} - \frac{e}{c}A_s)^2 + c^2(p_x - \frac{e}{c}A_x)^2 + c^2(p_y - \frac{e}{c}A_y)^2}. \tag{3.15}$$

## 3.5 Time as an independent variable

We have transferred the Hamiltonian into the curvilinear coordinate system but time is still an independent variable. We can use one of the Hamilton equations:

$$\dot{s} = \frac{\partial \mathcal{H}_F}{\partial p_{sc}}, \tag{3.16}$$

to transform Hamilton equations to a new form with s as an independent variable:

$$p_{xc}^{'} = \frac{\partial p_{sc}}{\partial x} \qquad x^{'} = -\frac{\partial p_{sc}}{\partial p_{xc}} \tag{3.17}$$

$$p_{yc}^{'} = \frac{\partial p_{sc}}{\partial y} \qquad y^{'} = -\frac{\partial p_{sc}}{\partial p_{yc}} \tag{3.18}$$

$$\mathcal{H}_F^{'} = \frac{\partial p_{sc}}{\partial t} \qquad t^{'} = -\frac{\partial p_{sc}}{\partial \mathcal{H}_F^{'}} \tag{3.19}$$

If we treat $-p_{sc}$ as a new Hamiltonian function, the structure of equations is conserved.

## 3.6 Courant-Snyder Hamiltonian

We note, that from the Maxwell Hamiltonian the Lorentz force can be derived which acts on a particle with elementary charge immersed in the electromagnetic field:

$$\vec{F_L} = e(\vec{E} + \vec{v} \times \vec{B}) \tag{3.20}$$

where $\vec{E}$ and $\vec{B}$ are electric and magnetic field vectors respectively, and $\vec{v}$ is the particle velocity. Assuming that we treat a part of a machine without RF and electrostatic devices, we set $\vec{E} = 0$. Then from a vector multiplication law we deduce, that any static magnetic field cannot change particle energy. Then we can write the Courant-Snyder Hamiltonian (C-S) assuming further change of coordinates acting on canonical momenta:

$$p_c \rightarrow p_c/p \tag{3.21}$$

Finally we can write the Courant-Snyder Hamiltonian [25], which describes the single charged particle dynamics in a static magnetic field in accelerator physics:

$$\mathcal{H}_{\mathcal{CS}} = -\frac{e}{cp}A_s(1+kx) - (1+kx)\sqrt{1-(p_x-\frac{e}{cp}A_x)^2-(p_y-\frac{e}{cp}A_y)^2} \tag{3.22}$$

The structure of the last formula is rather complicated and the Hamiltonian equations derived from it, describe in general nonlinear dynamics with multidimensional coupling. Its solutions are beyond the possibilities of analytical methods and can be only approximately treated by numerical methods generally known as tracking.

## 3.7 Magnetic field expansion

We shall introduce several simplifications in order to achieve approximate equations of motion, which can be solved analytically. The magnetic potential $\vec{A}$ and the magnetic induction $\vec{B}$ are connected by:

$$\vec{B} = \vec{\nabla} \times \vec{A} \tag{3.23}$$

It can be shown that in a machine with median (horizontal) plane symmetry, the longitudinal component of the magnetic induction on the median plane vanishes. In addition, one usually treats the magnetic field in the accelerators for small particle oscillation around the closed orbit to be purely transverse and vary stepwise along $s$ coordinate in the so called hard edge approximation. This is in particular the way the machine is designed in a first stage. More complicated field patterns are then treated as small perturbations and finally a multiparticle tracking with high statistics is launched in further steps of the machine study.

The magnetic field for the median plane symmetry machine within the hard edge approximation is described by the series expansion around a closed orbit:

$$\frac{e}{cp_0}B_x = Ky + mxy + O(3) \tag{3.24}$$

$$\frac{e}{cp_0}B_y = k + Kx + \frac{1}{2}m(x^2 - y^2) + O(3) \tag{3.25}$$

where $p_0$ is the momentum of the reference particle. We call the $K$ and $m$ the quadrupole and sextupole field strength and remind that the curvature $k$ is related to dipole field via equation 3.10. We have omitted all components of skew magnets, where coils are rotated with respect to the closed orbit. They are used only in very special applications in the accelerator technology ( for example for coupling compensation).We have also omitted so called geometrical terms which are proportional to the curvature $k$. They are of importance only in the very strong bending magnets (with big deflection angle). As usual in physics, the notion of "big" and "small" remains to be carefully studied case by case. The $B_s$ component only enter via terms which we have already assumed to omit. We shall treat it explicitly in the machine containing solenoids, which is an exception to median plane symmetry machines. One can check using equation 3.23, that the magnetic induction given by formulas 3.24 and 3.25 can be derived from magnetic potential:

$$\frac{e}{cp_0}A_s = -\frac{1}{2}(1 + kx) + \frac{1}{2}K(y^2 - x^2) - \frac{1}{6}m(x^3 - 3xy^2) + O(4) \tag{3.26}$$

In general one can always use the gauge invariance to make other magnetic potential components to vanish in the case of the median symmetry plane machine.

## 3.8 Paraxial approximation

The next simplification is the paraxial approximation. We shall simply assume in equation 3.21 that the denominator is large compared to the numerator. The physical meaning of this assumption is that particles have small transverse momentum components in comparison to the longitudinal one. We can make the following substitution in the C-S Hamiltonian:

$$\sqrt{1-(p_x-\frac{e}{cp}A_x)^2-(p_y-\frac{e}{cp}A_y)^2}\rightarrow 1-\frac{1}{2}(p_x-\frac{e}{cp}A_x)^2-\frac{1}{2}(p_y-\frac{e}{cp}A_y)^2 \tag{3.27}$$

In addition to the use of the field expansions around the closed orbit, we introduce the relative momentum deviation:

$$\frac{e}{cp}=\frac{e}{c}\frac{1}{p_0+\delta p}\rightarrow\frac{e}{cp_0}(1-\frac{\delta p}{p_0}) \tag{3.28}$$

where $\delta p = p - p_0$. It is important to mention, that the momenta in the previous formula are mechanical momenta not to be confused with generalized momentum.

# Chapter 4

# Transverse dynamics

In this chapter we shall use the C-S Hamiltonian, previously derived, to write the linear equations of motion which describe transverse dynamics. We shall introduce the matrix formalism, the condition for stability and the conserved quantity called emittance. Then, we mention the formalism to describe the motion of a particle with momentum deviation. Finaly, the linear dynamics in a solenoidal channel is discussed.

## 4.1 Hill equations

It can be shown that the C-S Hamiltonian simplifies to the second order Hamiltonian:

$$\mathcal{H}_{\in} = -\frac{1}{2} - \frac{1}{2}\frac{\delta p}{p_0} - \frac{\delta p}{p_0}kx - \frac{1}{2}K(y^2 - x^2) + \frac{1}{2}k^2x^2 + \frac{1}{2}p_x^2 + \frac{1}{2}p_y^2 \qquad (4.1)$$

from which one can derive the transverse equation of motion called the Hill equation for a horizontal and a vertical plane respectively:

$$x'' + (K + k^2)x = \frac{\delta p}{p_0}k \qquad y'' - Ky = 0 \qquad (4.2)$$

We shall study the solutions of these equations and their implications in the following section.

The Hill equations are very similar to harmonic oscillator equations. The only difference is that coefficients $k_x$ and $k$ are functions of s. In the hard

edge approximation we treat them as step functions. For a machine built of periodic structures of length L:

$$k_x(s) = k_x(s+L) \qquad K(s) = K(s+L) \tag{4.3}$$

A circular machine has at least a period equal to its circumference:

$$k_x(s) = k_x(s+C) \qquad K(s) = K(s+C) \tag{4.4}$$

## 4.2 Matrix formalism

Let us first assume that $\frac{\delta p}{p_0}$ vanishes, which mean that we study the particle dynamics without momentum deviation with respect to the reference particle. The solution of all second order equations similar to the Hill equation can be expressed in the matrix formalism:

$$\begin{pmatrix} x \\ x' \end{pmatrix} = \begin{pmatrix} C & S \\ C' & S' \end{pmatrix} \begin{pmatrix} x_0 \\ x'_0 \end{pmatrix} = MX \tag{4.5}$$

where matrix $M$ is usually called the transfer matrix. It expresses the change in the position $x$ and angle $x'$ after a passage through the magnetic element described by the matrix M from its entrance values $(x_0, x'_0)$. The matrix describing a set of several magnetic elements can be constructed by successive matrix multiplication of matrices describing single elements. Finally, one can construct the one turn matrix for circular machines. It can be shown [25] through the analysis of eigenvalues of M, that stability of the machine in question is achieved only when [25, 26]:

$$|Tr(M)| \leq 2 \tag{4.6}$$

By the stability condition we understand that after N turns all elements of the machine transfer matrix $M^N$ remain bounded when N goes to infinity. The matrix M can be parameterized [25] in the following way:

$$M = \begin{pmatrix} cos\mu + \alpha sin\mu & \beta_x sin\mu \\ -\gamma_x sin\mu & cos\mu - \alpha_x sin\mu \end{pmatrix} \tag{4.7}$$

where condition $\beta_x\gamma_x - \alpha_x^2 = 1$ is the other way of expressing the fact that matrix M has a determinant equal to one. The last result is well known in the theory of ordinary differential equations, where unity of the determinant

called Wronskian expresses the lack of the term proportional to the first derivative of $x$ ($x'$) in the equation, in other words the lack of the dissipative term. The matrix M in the parameterization given by equation 4.7 is called the Twiss matrix in the accelerator physic literature.

## 4.3 Beam ellipse and invariant of motion

We shall now give a meaning to the coefficients $\alpha_x$, $\beta_x$ and $\gamma_x$.

The solution of the Hill equation can be postulated in the following way

$$x(s) = a\sqrt{\beta_x(s)}cos(\mu(s) - \mu_0) \tag{4.8}$$

The cosine term in the above equation is very similar to the $cos(\omega t)$ term in the solution of the harmonic oscillator problem. We can see that $\mu(s)$ plays a similar role to the angular frequency $\omega$. In particular, when $\mu(s)$ grows by $2\pi$ the particle motion performs an oscillation by one period around the closed orbit. A major difference with the harmonic oscillator lies in the amplitude term $\sqrt{\epsilon\beta_x(s)}$, which is a function of $s$. The beta function $\beta_x(s)$ defines the envelope of the beam. In particular, the maximum radius of the beam vary as:

$$r_{max}(s) = a\sqrt{\beta_x(s)} \tag{4.9}$$

After substitution of the Ansatz 4.8 into the Hill equation, we can make a connection with the Twiss matrix. The way we introduced the coefficients was not arbitrary. The detailed studies [25] show that $\beta_x$ and $\mu$ in the Twiss matrix of the whole machine corresponds to the equation 4.8. The exact meaning is as follows: the parameterization of the one-turn matrix corresponds to the value of $\beta_x$ function in the point we start the calculation. The phase $\mu$ corresponds to the total phase advance in the machine. The value $\mu_0$ in equation 4.8 was chosen to set the initial conditions. We shall give the relations between the parameters without proof. For details see [25, 26].

$$\alpha = -\frac{1}{2}\beta_x' \qquad \gamma = \frac{1+\alpha_x^2}{\beta_x} \qquad \mu = \int_C \frac{1}{\beta_x} ds \tag{4.10}$$

where the integration is performed around the circumference $C$ of the machine. The tune of the machine is:

$$Q = \frac{\mu}{2\pi} \tag{4.11}$$

Tune corresponds to a number of betatron oscillations performed by the particle during one turm around the machine.

Now we shall comment about the constant $a$ in the equation 4.8. Its form suggests that:

$$a^2 = \frac{1}{\beta_x}\left[x^2 + (\alpha_x x + \beta_x x')^2\right] = \gamma_x x^2 + 2\alpha_x x x' + \beta_x x'^2 = \epsilon \tag{4.12}$$

The last formula is known as the Courant-Snyder invariant. It is an ellipse equation, in which the area (equals to $\pi\epsilon$) remains constant in the transfer line or in the storage ring, where quantum excitations ( emission of the synchrotron radiation, decay, intrabeam scattering, interaction with the residual gas, etc.), nonlinear magnetic fields and couplings can be neglected. Conservation of the Courant-Snyder invariant $\epsilon$ is the 2-dimensional analogue of the Liouville theorem, which tells us about the phase space volume conservation in the Hamiltonian systems. The applicability of the concept of emittance can be understood in the following way. The ellipse enclosing the beam is changing from point to point in the machine, but its area remains constant. The parameters describing the shape and orientation of the ellipse in the phase space $(\alpha_x, \beta_x, \gamma_x)$ are instead continuously evolving usually in the periodic way. The exact meaning of the parameters describing the ellipse can be deduced from equation 4.12 and some of them are shown in Figure 4.1.

The emittance conservation is one of the principles of accelerator physics. Together with all linear beam parameters $(\alpha_x, \beta_x, \gamma_x, \mu)$ in spite of their approximate notion serves as an extremely fruitful description tool widely used in the subject. It is important to note that approximations used to derive the linear theory are extremely successful in almost all existing machines.

## 4.4 Orbit dispersion

We shall now briefly describe the motion of a particle with momentum deviation with respect to the refence particle. The only term, which has survived after linearization is $k_x \frac{\delta p}{p_0}$. This term describes the chromatic change of the

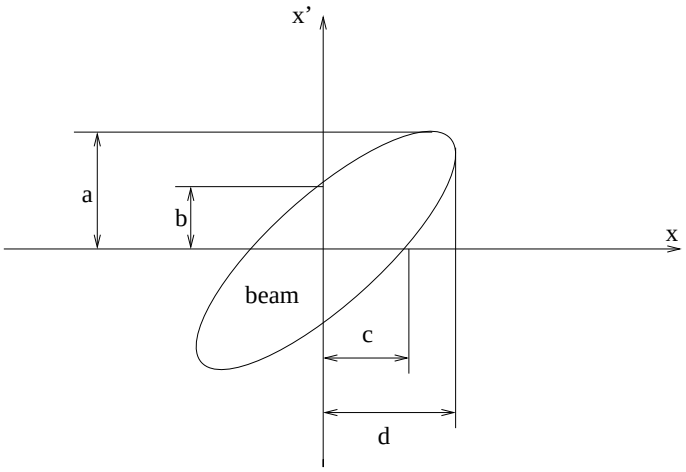


Figure 4.1: The orientation of beam ellipse in the phase space parameterized by Twiss functions: $a = \sqrt{\epsilon\gamma_x}$, $b = \sqrt{\epsilon/\beta_x}$, $c = \sqrt{\epsilon/\gamma_x}$, $d = \sqrt{\epsilon\beta_x}$. The upright ellipse corresponds to $\alpha_x = 0$.

orbit in the bending magnets due to the different radius of curvature of the particle with the momentum deviation. In this approximation we do not take into account changes in the focusing properties. The general solution of the inhomogeneous Hill equation:

$$x'' + (K + k^2)x = \frac{\delta p}{p_0}k \tag{4.13}$$

can be described in the matrix form:

$$\begin{pmatrix} x \\ x' \\ \frac{\delta p}{p_0} \end{pmatrix} = \begin{pmatrix} C & S & D1 \\ C' & S' & D1' \\ 0 & 0 & 1 \end{pmatrix} \begin{pmatrix} x_0 \\ x'_0 \\ \frac{\delta p}{p_0} \end{pmatrix} \tag{4.14}$$

We can assume, that a particle has a zero betatron amplitude and try to find a dispersive orbit for that particle - the closed orbit for the particle with momentum deviation. It can be shown that dispersion, which is defined as a deviation of the dispersive orbit from the closed orbit of the reference particle normalized to the momentum deviation:

$$D = \frac{x_D}{\frac{\delta p}{p_0}} \tag{4.15}$$

fulfills the equation:

$$D'' + (K + k^2)D = k \tag{4.16}$$

The equation shows a similarity to the driven harmonic oscillator. We mention without proof the solution for the periodic dispersion:

$$D(s) = \frac{\sqrt{\beta_x(s)}}{2sin(\pi Q)} \int_s^{s+L} \frac{\sqrt{\beta_x(\sigma)}}{\rho(\sigma)} cos(\mu(s) - \mu(\sigma) + \pi Q) d\sigma \tag{4.17}$$

where the integration is performed along the length of a periodic structure L, which can be the whole circumference of the machine.

## 4.5 Example: FODO lattice

As an illustrative example we shall explore the stability of the FODO channel, the focusing system by far the most common among accelerator applications. The name stands for F - focusing in quadrupole with positive K, O drift with eventually bends or other insertions, D - defocusing in quadrupole with negative K. A quick look at the Hill equations shows the alternating function of quadrupole for horizontal and vertical motion respectively, which can be seen by different signs in the terms proportional to K. The famous Alternating Gradient (AG) principle is exactly an analogy of optical focusing in light optics, where the combination of focusing and defocusing lenses creates a net effect of focusing in the horizontal and the vertical plane, simultaneusly. The only difference is that the "magnetic lenses" in the charged particle optics - the quadrupoles are focusing in one plane and defocusing in the other, but alternating the sign along the beam line produces a net focusing. We shall define a few parameters:

$$K = \frac{eg}{cp_0} \qquad f = \frac{1}{Kl_q} \tag{4.18}$$

where $K$ is the focusing strength of a quadrupole (the same coefficient as in the Hill equation), $g = \frac{\partial B_y}{\partial x}$ is the field gradient and $f$ is the focal length of the quadrupole. The matrices, which correspond to drift and thin quadrupole are of the following form respectively:

$$M_L = \begin{pmatrix} 1 & L \\ 0 & 1 \end{pmatrix} \qquad M_q = \begin{pmatrix} 1 & 0 \\ -\frac{1}{f} & 1 \end{pmatrix} \tag{4.19}$$

where $f$ is positive for a focusing lens and negative for a defocusing one. The matrices, which correspond to thick quadrupoles focusing and defocusing respectively, are given by:

$$M_F = \begin{pmatrix} cos(l\sqrt{|K|}) & \frac{1}{\sqrt{|K|}} sin(l\sqrt{|K|}) \\ -\frac{1}{\sqrt{|K|}} sin(l\sqrt{|K|}) & cos(l\sqrt{|K|}) \end{pmatrix} \tag{4.20}$$

$$M_D = \begin{pmatrix} cosh(l\sqrt{|K|}) & \frac{1}{\sqrt{|K|}} sinh(l\sqrt{|K|}) \\ \frac{1}{\sqrt{|K|}} sinh(l\sqrt{|K|}) & cosh(l\sqrt{|K|}) \end{pmatrix} \tag{4.21}$$

We shall now use thin lens approximation to derive the stability condition for the periodic FODO lattice. We cut the lattice in the middle of the focusing quadrupole, which is represented by the matrix with focal length 2f. In this way we study a symmetric cell until next half of the focusing quadrupole. We calculate the trace of the transfer matrix evaluated by successive multiplication of matrices representing in the sequence: half of focusing quadrupole, drift, defocusing quadrupole, drift and half of focusing quadrupole, see Fig.4.2.

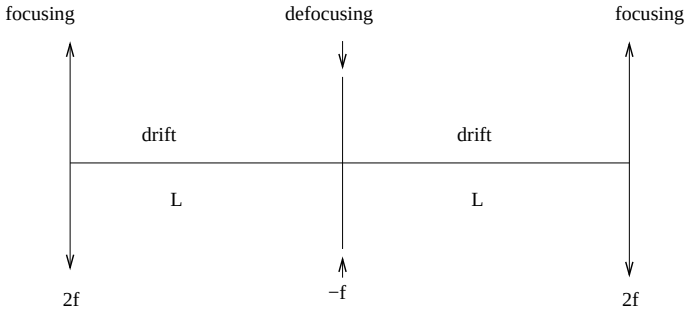


Figure 4.2: The sketch of elements in symmetric FODO cell.

We evaluate now the trace of the full transfer matrix and after using the Twiss parameterization 4.7 we can express it in the very useful form:

$$cos\mu = 1 - \frac{L^2}{2f^2} \qquad sin(\mu/2) = \frac{L}{2f} \tag{4.22}$$

The condition for stability 4.6 is equivalent to the condition, that $\mu$ has to be real. The last statement is equivalent to the condition: the focal length must be longer than the half distance between two lenses. It is interesting to note that taking into account the variation of the parameters with momentum and assuming a constant magnetic field the FODO channel is always stable for particles with higher energy than the reference particle. For particles with higher energy (momentum) the line is just a FODO channel with a different $k$ ($f$ in thin lens approximation). The phase advance per cell diminishes with momentum. For lower momentum particles one can easily derive the formula for the maximal relative momentum deviation accepted by the channel:

$$\frac{\delta p}{p_0} > sin(\mu/2) - 1 \tag{4.23}$$

It is important to note that the beta function goes to infinity near the limits of stability. Then the real acceptance limit has to be more restrictive than 4.23. For the same reason, the stability on the higher energy side is limited too. An example of the FODO cell including dipoles put in the middle of the drift is given. We treat quadrupoles first in the thin lens approximation and then find the thick quads solution with the same horizontal phase advance per cell. We make the linear beam dynamics calculation in the framework of the BeamOptics code developed at CERN [27]. The optical functions calculated with thick and thin lens models are shown in Fig. 4.3 and 4.4, respectively. The difference in the shape of the beta function is due to the localization of the effect on the beam in the thin lens, which works as a point-like kick. The parameters of the cell are listed in table 4.1. They are very similar, but not identical.

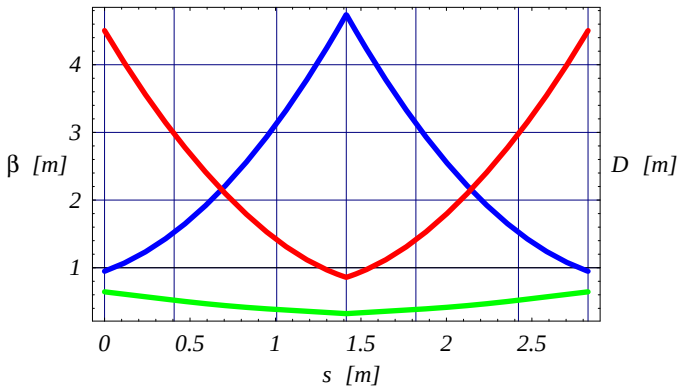


Figure 4.3: The optical functions in the FODO cell calculated in thin lens approximation. The red, blue and green lines are $\beta_x$, $\beta_y$ and $D$ functions, respectively.

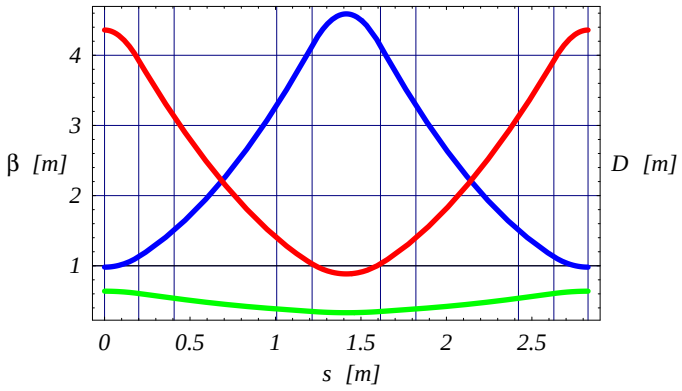


Figure 4.4: The optical functions in the FODO cell calculated using thick quadrupoles. The red, blue and green lines are $\beta_x$, $\beta_y$ and $D$ functions, respectively.

| | thin lenses | thick lenses |
|---|---|---|
| $Q_x$ | 0.25 | 0.25 |
| $Q_y$ | 0.232 | 0.232 |
| $\beta_x$ in the middle of F-quad | 4.504 m | 4.359 m |
| $\beta_y$ in the middle of F-quad | 0.948 m | 0.981 m |
| $D$ in the middle of F-quad | 0.644 m | 0.637 m |
| cell length | 2.828 m | 2.828 m |
| quad length | - | 0.4 m |
| dipole length | 0.6 m | 0.6m |
| bending per cell | $\pi/9$ rad | $\pi/9$ rad |

Table 4.1: Parameters of the FODO cell in thin and thick approximations.

## 4.6 Linear optics in a solenoidal channel

In general the coupling between horizontal and vertical motions can be created by a non vanishing solenoidal magnetic field component and rotated quadrupoles. In particular these effects are always present in the real machine due to field errors and misalignments as small perturbations. In some cases the effects of coupling can be rather strong due to the presence of solenoids ( for example in the detectors in colliders or electron cooling devices). In very special applications we can find solenoids as permanent focusing elements in the low energy sources and transfer lines. This is exactly the case of the solenoidal designs for the neutrino factory muon front end, which we shall study in the next chapter. Because of that we shall pay some attention to this kind of focusing to prepare the ground for applications.

In the presence of coupling the linear optics is described by $4 \times 4$ transfer matrix. To simplify the problem we shall perform a change of coordinates to treat the problem in $2 \times 2$ formalism. We shall treat a linac focused by solenoids. The transverse magnetic field expressed to first order in x and y can be described by:

$$B_x = -\frac{1}{2} x B_s'(0,0,s) \qquad B_y = -\frac{1}{2} y B_s'(0,0,s) \tag{4.24}$$

where $B_s' = \frac{dB_s}{ds}$. The $B_s$ component of the field is a function of s and varies with the distance from the axis in higher order in x and y.

We shall now follow the derivation of [28] or [29]. Similar results including the method to calculte the $4 \times 4$ transfer matrix can be find in [30]. The linearized equations of motion can be written in the following way:

$$x'' - S(s)y' - \frac{1}{2} S'(s) y = 0 \tag{4.25}$$

$$y'' + S(s)x' + \frac{1}{2} S'(s) x = 0 \tag{4.26}$$

where $S = \frac{e}{cp_0} B_s$. Note a high degree of symmetry in equations 4.25 and 4.26. We shall use this symmetry to transform to decoupled equations. We introduce a rotation in complex coordinates:

$$R = (x + iy) e^{-i\phi_L(s)} \tag{4.27}$$

By introducing the rotation angle specified by the formula:

$$\phi_L(s) = \frac{1}{2}\int_0^s S(z)dz \tag{4.28}$$

we can end up with decoupled equations:

$$\tilde{x}'' + \frac{1}{4}S^2(s)\tilde{x} = 0 \qquad \tilde{y}'' + \frac{1}{4}S^2(s)\tilde{y} = 0 \tag{4.29}$$

where the new coordinate system $(\tilde{x}, \tilde{y})$ ( sometimes called the Larmor frame) rotates around the laboratory system $(x, y)$. We note the similarity of equation 4.29 with the Hill equation. In particular we shall use the beta function formalism similar to the decoupled case assuming the rotational symmetry of the beam. Precisely speaking the beta function in the linac focused by solenoids is exactly the same as the horizontal beta function in the linac focused by focusing quadrupoles ( with the same sign of k ) replacing k by $\frac{1}{4}S^2(s)$ in the hard edge approximation or by $\frac{1}{f_{sol}} = \frac{1}{4}S^2(s)L_{sol}$ in the thin lens approximation, where $L_{sol}$ is the length of the solenoid.

In machine with coupling, the off-momentum orbits can be described by the horizontal $D_x$ and the vertical $D_y$ dispersion functions. The necessary matrix formalism to descibed them is a generalization of $3 \times 3$ formalism ( see paragraphe 2.12 ) to $5 \times 5$ one.

## 4.7 Example: FOFO lattice

With analogy to the FODO cell one can consider a cell of symmetric channel focused by solenoids giving it the name FOFO cell. This kind of channel is focusing in both planes simultaneously. This fact can be used to avoid large amplitude oscillations of the beam to provide a smooth beta function with small value, which can be used to transport low energy and large emittance beams. These properties make solenoidal channels very useful in the design of particle sources and beam cooling devices. Using defined in the previous section the focal length of the solenoid, one can derive expressions for the betatron phase advance in the FOFO cell consisting of half of the solenoid, drift and again half of the solenoid.

$$cos\mu = 1 - \frac{L}{2f} \qquad sin(\mu/2) = \frac{1}{2}\sqrt{\frac{L}{f}} \tag{4.30}$$

The stability again, as in the FODO case, reduces to the condition of $\mu$ to be real. It is remarkable to note that the cell is stable for higher momentum

and the stability of lower momentum is expressed in exactly the same manner as for the FODO:

$$\frac{\delta p}{p_0} > sin(\mu/2) - 1 \tag{4.31}$$

The comments already mentioned for the FODO about more strict treatment of these limits apply likewise for the FOFO case with even more attention due to quadratic momentum dependence of $cos\mu$ and even faster beta function growth. As an example we show the Larmor beta function of the cell for 200 MeV kinetic energy muon beam, 0.5 m long 1.8 T solenoids and drift length equal to 1.5 m in Fig. 4.5

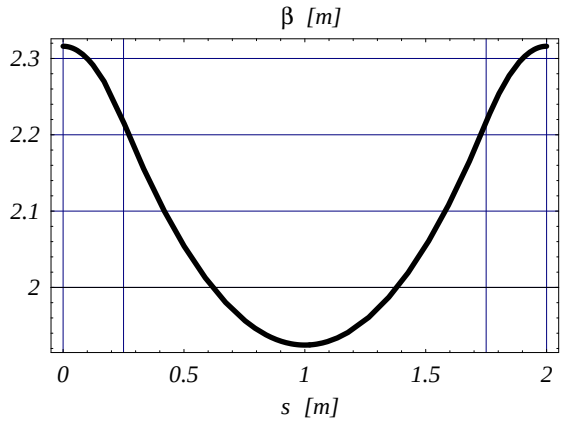


Figure 4.5: The Larmor beta function in the FOFO.

## 4.8 Remarks on nonlinear dynamics

The nonlinear dynamics enter the beam physics through various doors. The previous discussions neglect quadratic and all higher order terms in the magnetic field expansion. In addition, in our derivation of the equations of motion we have applied paraxial approximation, which helps to simplify the problem, but neglects higher order terms.

Nonlinear fields can be seen as a small perturbation due to errors, in the ends of magnetic elements as so called edge effects or can be introduced as a special field component in the combined function magnets, or as special separated function elements.

One of the most important applications of nonlinear elements is chromaticity correction with sextupoles, magnetic elements in which the field changes quadraticaly with distance from the magnetic axis. The exact treatment of dynamics of a particle with momentum deviation shows a tune variation with momentum, mostly because the focusing strength of a quadrupole decreases with momentum. These effects can be quantified by defining the chromaticity:

$$\xi = \frac{\frac{\delta Q}{Q}}{\frac{\delta p}{p_0}} \tag{4.32}$$

It can be shown that the chromaticity can be corrected by placing the sextupole magnets in dispersion regions. For example in the horizontal plane holds:

$$\xi_x = -\frac{1}{4\pi Q_x}\int_C \beta_x(K - mD)ds \tag{4.33}$$

where the first term in the integral is the so called natural chromaticity of the ring and the second one corresponds to correction with sextupolar component described by $m$.

The reason for taking care of the chromaticity correction is very interesting. The nonlinearities in the magnetic fields, which are always present due to errors and misalignments, can act destructively on the beam in circular accelerators for certain tune values, which fulfill the resonant condition:

$$aQ_x + bQ_y = integer \tag{4.34}$$

with $a$ and $b$ being integer. It can be pictorially understood in the following way: for the resonant condition, the particle sees the perturbation always in the same way, let's say "in phase", and the effect can add up creating a loss of the particle. In the out of resonance condition effects from various passes cancel out each other. The chromaticity correction controls the variation of tune with momentum and the working-point chosen for on-momentum in the $(Q_x, Q_y)$ diagram. Without the chromaticity correction the tune for off-momentum particles could move close to a dangerous resonance.

Another nonlinear phenomenon enters via the edge effect. In the end of magnetic elements, where the field reduces to zero , higher order terms in the field expansion cannot be neglected. We can treat this effect assuming that the magnetic field vanishes on a relatively short distance compared to

betatron wave-length and compared to the length of a magnetic element. Then the longitudinal variation of the magnetic field can be approximated in this limit as a step function. The change in the position and angle of the particle passing through the input end of a quadrupole can be estimated via the following equations [34]:

$$\Delta x = (\frac{1}{12}x^3 + \frac{1}{4}xy)K \qquad \Delta x' = (\frac{1}{2}xyy' - \frac{1}{4}x'(x^2 + y^2))K \tag{4.35}$$

At the output of the quadrupole, the sign of $K$ is reversed. The same equations apply to the vertical motion when $K$ is changed to $-K$. In the case of real end field patterns, numerical tracking methods and explicit field calculations are needed.

Other nonlinear terms arise from the exact treatment of equation 3.27. They are called the kinematical terms. Their effect is usually negligibly small in conventional accelerators, but has to be studied carefully in extreme cases such as the interaction region of the muon collider, where the relatively large emittance beam has to be focused to a very small beta function value. The effect is usually explicitly included in tracking codes, which take into account higher order beam dynamics.

At the end of this section we shall comment about the Liouville theorem and applicability of emittance in the presence of nonlinearities. The Liouville 6D phase space volume is conserved even in the presence of strong nonlinear fields and couplings, but the 2D emittances are not conserved. The horizontal, vertical and longitudinal 2D emittances can be viewed as projections of the 6D volume. In the presence of nonlinearities and couplings the projections of motion are not ellipses. First filamentation can be observed and for the presence of even higher nonlinearities the dynamical portrait is noncompact due to the creation of islands and a transport between the subspaces is possible. The presence of nonlinearities can create an increase in 2D emittance.

# Chapter 5

# Longitudinal dynamics

We shall now turn on the RF (radiofrequency) cavities and explore the dynamics in the longitudinal phase space. The concept of the phase stability was independently discovered by [32] and [31] in 1945. It resolved the problem of acceleration of charged particles to arbitrarily large relativistic energies. We shall now briefly explain the particle dynamics in the synchrotron under the influence of RF fields. The acceleration of particles is also possible with electrostatic devices, but its field gradient is limited to values much lower than in RF cavities. Nevertheless, they are still in use in, for example, particle sources.

## 5.1 Synchrotron equation in a linac

We shall derive briefly the phase focusing effect in a linac [33] and then comment about phase focusing in a ring. We shall not study the principles of the design of the RF cavities. The longitudinal component of the electric field changes with time according to the law:

$$E = E_0 cos(\omega_{RF} t - \frac{\omega_{RF} z}{v_p}) = E_0 cos\phi \tag{5.1}$$

where we have introduced the phase variable $\phi$, and $v_p$ is a particle velocity. The synchrotron motion is the motion of a particle with energy deviation $\delta W$ and phase deviation $\delta\phi$ with respect to the reference particle accelerated at the synchronous phase $\phi_s$. The expression of $\delta W$ after passage through a cavity of length $L_c$ is:

$$\delta W = qE_0L_cT_t(cos\phi - cos\phi_s) \tag{5.2}$$

where q is a charge of the particle and $T_t$ is the transit time factor, which takes into account the variation of the field during the particle passage through the cavity. The transit time factor can be expressed by:

$$T_t = \frac{sin(\theta/2)}{\theta/2} \qquad \theta = \omega_{RF}L_c/v_p \tag{5.3}$$

where $L_c$ is the cavity length. The transit time factor is of great importance for nonrelativistic transport lines. For relativistic energies usually it is close to unity. Assuming the acceleration continuously distributed along the channel, the variation of $\delta W$ with s is:

$$\frac{d}{ds}\delta W = qE_0T_tcos[(\phi_s + \delta\phi) - cos\phi_s] \tag{5.4}$$

The derivative of $\delta\phi$ with s is:

$$\frac{d}{ds}\delta\phi = \frac{\omega_{RF}}{c}(\frac{1}{\beta} - \frac{1}{\beta_s}) \approx -\frac{\omega_{RF}}{m_0c^3\beta_s^3\gamma_s^3}\delta W \tag{5.5}$$

The equations 5.4 and 5.5 govern the synchrotron motion. The invariant of the linear synchrotron motion can be written:

$$\frac{(\delta\phi)^2}{a^2} + \frac{(\delta W)^2}{b^2} = const \tag{5.6}$$

The area of the above ellipse is the longitudinal emittance.

The synchrotron oscillation wave-length is:

$$\Lambda_s = 2\pi(-\frac{\omega_{RF}qE_0T_tsin\phi_s}{m_0c^3\beta_s^3\gamma_s^3})^{-\frac{1}{2}} \tag{5.7}$$

We come back to the equations 5.4 and 5.5 and derive the second order equation of motion:

$$\frac{d^2\delta\phi}{ds^2} + \frac{\omega_{RF}qE_0T_t}{m_0c^3\beta_s^3\gamma_s^3}[cos(\phi_s + \delta\phi) - cos\phi_s] = 0 \tag{5.8}$$

The motion can be seen as a nonlinear oscillation in an effective potential possessing one stable and one unstable fixed points. The effective potential is:

$$U(\delta\phi) = \frac{\omega_{RF}}{m_0 c^3 \beta_s^3 \gamma_s^3} q E_0 T_t [sin(\phi_s + \delta\phi) - sin\phi_s - \delta\phi cos\phi_s] \tag{5.9}$$

The equation of the separatrix which divides the phase space into stable and unstable regions:

$$\frac{\omega_{RF}}{2 m_0 c^3 \beta_s^3 \gamma_s^3} (\delta W)^2 + q E_0 T_t [sin(\phi_s + \delta\phi) + sin\phi_s - (2\phi_s + \delta\phi) cos\phi_s] = 0 \tag{5.10}$$

The separatrix, together with the electric field and the effective potential are shown in Fig. 5.1.

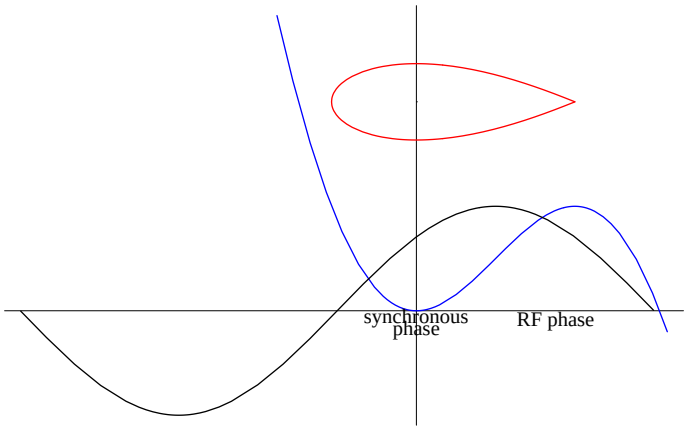


Figure 5.1: The relative position of the stable RF bucket $(\delta\phi, \delta W)$ in red with respect to the effective potential $(\delta\phi, U)$ in blue and the electric field $(\phi, E)$ in an RF gap in black.

## 5.2 Orbit lengthening and transition

The effect of orbit dispersion in the magnet due to different radi of curvature for particles with different momenta creates a different path length of orbit for particles with different momenta. The change of length of the path to first order is given by:

$$\delta L = \int_s^{s+L} \frac{x(s) ds}{\rho(s)} \tag{5.11}$$

For off-momentum orbit described by dispersion function the previous equation can be written:

$$\delta L = \frac{\delta p}{p_0} \int_s^{s+L} \frac{D(s)ds}{\rho(s)} \tag{5.12}$$

Now we can define the momentum compaction factor $\alpha_c$:

$$\alpha_c = \frac{1}{L} \int_s^{s+L} \frac{D(\sigma)}{\rho(\sigma)} d\sigma \tag{5.13}$$

The time of flight on the path with length L is:

$$T = \frac{L}{c\beta} \tag{5.14}$$

Now we calculate the variation of T:

$$\frac{\delta T}{T} = \frac{\delta L}{L} - \frac{\delta \beta}{\beta} \tag{5.15}$$

The first therm represents contribution from path length variation and the second one corresponds to speed variation with energy. Finaly we can write the formula for the time variation:

$$\frac{\delta T}{T} = (\alpha_c - \frac{1}{\gamma^2}) \frac{\delta p}{p_0} = \eta \frac{\delta p}{p_0} \tag{5.16}$$

where $\gamma$ is the relativistic factor for the reference particle, $\eta$ is called the slipping factor and plays an important role in longitudinal dynamics. In particular one can find a specific value of $\alpha_c$ for which $\eta$ vanishes. In that particular point there is no difference in the revolution frequency for the particles with momentum deviations. This point of machine operation usually creates additional difficulties because of a lack of longitudinal stability. This point is called the transition. The equation 5.16 can be rewritten in the following way:

$$\frac{\delta T}{T} = (\frac{1}{\gamma_T^2} - \frac{1}{\gamma^2}) \frac{\delta p}{p_0} \tag{5.17}$$

where $\gamma_T$ called "gamma transition" is defined by:

$$\gamma_T = \frac{1}{\sqrt{\alpha_c}} \tag{5.18}$$

## 5.3 Longitudinal focusing in a ring

We shall now briefly comment about the phase focusing in a ring accelerator. The synchronous particle has to remain synchronised with respect to the cavities. The RF frequency is thus an integer multiple of the revolution frequency:

$$\omega_{RF} = h\omega_{rev} \tag{5.19}$$

where, $h$ called the harmonic number, is an integer number. Then the particle with momentum deviation has a different length of orbit, which has an influence on the arrival time in the cavity. Assuming the continuous acceleration model, one can derive the similar synchrotron equation with time as independent variable instead of length. One can show that the synchrotron oscillation in the ring accelerator is described by the synchrotron frequency:

$$\Omega_s^2 = \frac{hqV_{max}T_t\eta_s\omega_{rev}sin\phi_s}{2\pi R_s p_s} \tag{5.20}$$

where $R_s$ is the effective ring radius with $2\pi R_s$ equals to the orbit length for the synchronous particle and $\eta_s$ is the slipping factor defined in equation 5.16. This expression differs from 5.7 by expressing the RF frequency in terms of revolution frequency and harmonic number, by expressing the electric field by the averaged voltage around the ring ($\frac{V_{max}}{2\pi R_s}$) and by putting the proper expression for $\eta_s$, which in the linac is simple $-\gamma_s^-2$.

## 5.4 Normalized emittance

We will take a moment to comment on quantities, which are strictly conserved during the motion. The transverse emittance defined in section 4.3 is conserved only in the absence of acceleration. It can be clearly seen in the simplified way: consider a beam of particles crossing a very short accelerating cavity. The $x'$ of the particles is reduced after passage through the cavity because the transverse momentum component was unchanged, but the longitudinal one was increased by the process of acceleration. The position $x$ of beam particles was not changed during the passage through very thin cavities. It seems that the Liouville theorem is violated, but it is only because we treat the Hamiltonian in which we have assumed that energy is constant. When acceleration is present the angle $x'$ is no longer canonically

conjugated to the $x$ variable. The process of decreasing $x'$ during acceleration is called adiabatic damping. One can define a quantity, which remains conserved during acceleration. This is the so called normalized emittance:

$$\epsilon_N = \beta\gamma\epsilon \tag{5.21}$$

where $\beta$ and $\gamma$ are relativistic factors of the reference particle of the beam. It turns out in the longitudinal plane, that the phase difference $\delta\phi$ and energy difference $\delta W$ are already the canonical variables, and the longitudinal emittance is conserved during acceleration. There still exists an analogy of the adiabatic damping in the decrease of $\delta\phi$ with acceleration. This is accompanied by increase of $\delta W$ which leaves the longitudinal emittance unchanged:

$$\delta\phi \sim (\beta_s\gamma_s)^{-\frac{3}{4}} \qquad \delta W \sim (\beta_s\gamma_s)^{\frac{3}{4}} \tag{5.22}$$

# Chapter 6

# Input beam for muon front end

Now we shall introduce the subject of beam dynamics in the muon front end of the neutrino factory. Firstly we shall define the subject and describe the input beam, which we want to accept.

## 6.1 Front end in an accelerator

Front end is usually the part of the accelerator facility, which prepares the beam of charged particles created in the source before acceleration or storage. The front end defines the beam for the downstream part of the accelerator. The condition under which the cloud of charge is being created in the source makes it very difficult to handle directly. This is because the charge particle sources usually creates particles incoherently producing wide thermalized charge distributions. Without special treatment in the front end most of this beam would be lost. The front ends are usually constructed with special elements providing the focusing system with very large transverse acceptance. The longitudinal plane usually needs special treatment to prepare the beam in the well defined acceptance limits for easy use of the RF system in the downstream accelerator installation.

The muon front end is not an exception to the situation described above. In addition, it has the responsibility of delivering enough muon intensity for the accelerator to achieve neutrino flux with promising discovery potential. In other machines there are other options for achieving enough intensity in proton or electron machines. Usually, the source current can be increased or the beam storage applied to achieve the required intensity. In the case of a

neutrino factory all parameters are almost at the physical or technological limits. The highest possible muon intensity is limited by the instantaneous proton current on target, its repetition rate and a cross section for pion production. The energy deposition of 4 MW proton beam considered for a neutrino factory and superbeam operation on the target makes it one of the most challenging parts of the machine. The repetition rate is also limited by the special time structure of the beam required for a muon storage ring, which dictates the small duty factor. The duty factor is defined as a ratio of time with beam and total machine cycle. In addition, the muon beam cannot be stored before final injection into the storage ring at the ultimate energy because of muon decay.

## 6.2 Beam time structure

The muon beam macrostructure in the neutrino factory is predefined by the presence of a decay ring, which dictates low duty factor for the muon front end and accelerator. In other words, after the final filling into the decay ring the muon beam performs a few hundreds revolutions and no intermediate filling is foreseen in the present scenarios. A further limitation is given by the horn repetition frequency, which, set at 50 Hz, is already a technological challenge. The muon beam inherits the time macrostructure from the proton beam in the present approaches. It consists of a single bunch or a train of bunches. Its structure constitutes a beam microstructure.

The beam microstructure can stay constant in the front end, being a carbon copy of the proton beam microstructure at the target. In this case we refer to the bunch to bucket principle (B2B). In other words, there is a one-to-one correspondence between proton bunches hitting the target and muon bunches trapped inside stable buckets at the exit of the muon front end. This is exactly the case for the CERN reference scenario [19], where a train of 140 proton bunches at 44 MHz hits the target and muons are phase rotated and cooled at the same frequency of 44 MHz or at a second harmonic - 88 MHz in the latest proposal leaving every second bucket empty. The same principle governs the Japanese NuFact design [35] where the time structure is kept constant from the target through the whole FFAG ring chain.

It is also possible to change the time structure in the front end, which can be done in the process of bunching. This beam manipulation is motivated by the use of high frequency RF, which offers a higher accelerating gradient,

of interest for fast cooling or acceleration. A large single bunch or a train of low frequency bunches is converted into the train of high frequency bunches with high efficiency. This philosophy is used in the American NuFact Study I [17], where the single bunch is phase rotated in induction linacs and bunched at 200 MHz in the double harmonic buncher ( 400 MHz cavities are used to modify the potential of 200 MHz cavities to minimize the losses). The Study II [18] proposes to bunch the beam at 200 MHz by a special technique developed by D. Neuffer [36] called adiabatic bunching, where the bunch, after passing a long drift, is injected into the buncher with varying RF frequency (300-200 MHz) and voltage. Then the bunched beam is rotated by the 200 MHz phase rotation section.

## 6.3 Input beam

We start our description with the proton beam at the target although some authors do not include targetry, capture and decay channel problems into the front end. Nevertheless, these components and its parameters define the muon beam for the neutrino factory.

The proton beam at the target consists of the single bunches (or train of bunches) usually with assumed short time length of the order of 1 ns rms or 4 ns total. At the target in nuclear physics reactions, a detailed description of which is beyond the scope of this note, pions are created in a very large transverse emittance and with a very large energy spread. In other words pions, are produced with large transverse and longitudinal momentum spread. It should be noted, that detailed parameterization of pion production cross section is still unknown to a sufficient precision. Surprisingly, the process of pion production extensively used for many years in nuclear and particle physics for a production of secondary beams (for example in Meson Factories), was not exactly measured for a wide spectrum of target materials. The uncertainty of even 20 % can be present in measured production cross sections. The existing codes differ in many aspects in simulating the target production process. Nevertheless, there is a hope, that this problem may be resolved by the Harp experiment [37], the purpose of which is to measure the cross sections in question.

In this note we use the particle production simulated by the MARS code [38], which was used for the horn simulations in [39]. The departure from physical values will result in different particle yields and could even have

an influence on the capture reference energy and thus modify the front end design, but the general concept will remain valid. At the target, the pion beam is captured in the magnetic horn [39] or in the high field solenoid. The choice and details of the capture scheme are irrelevant for our study. From now on, we assume horn capture and in addition, we assume 4 ns long proton bunch with time distribution given in [14]. The arrival time is sampled using Monte-Carlo methods. The proton beam time distribution at the target is shown in Fig. 6.1. The pion spectrum at the horn output calculated in the MARS simulation is shown in Fig 6.2. The simulation takes into account tracking in the magnetic field of the horn and scattering in the walls.

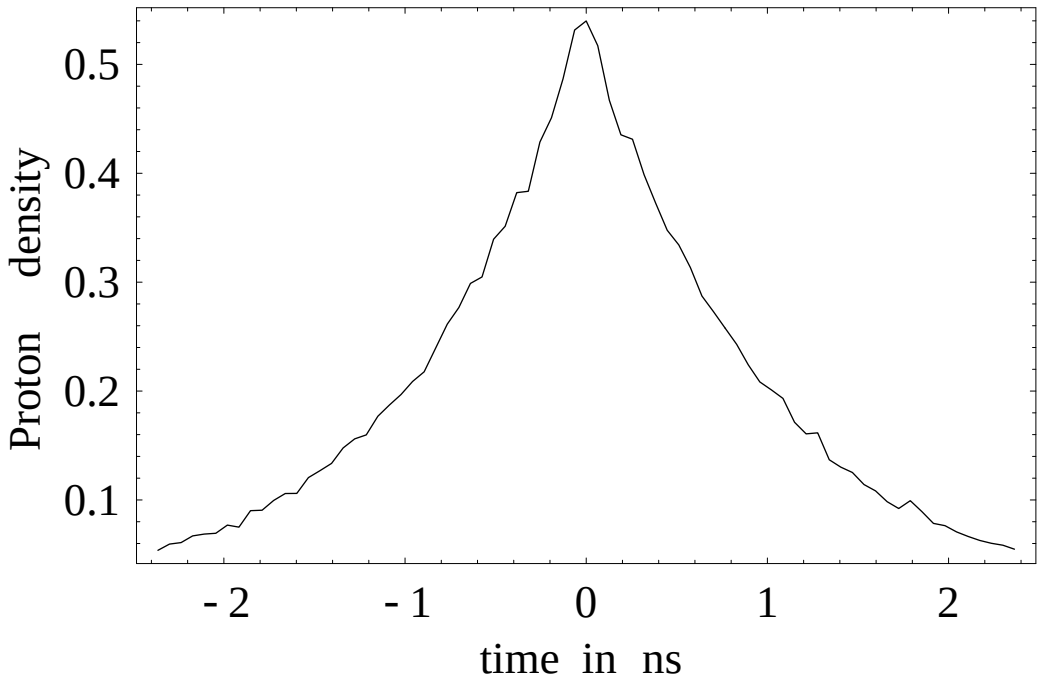


Figure 6.1: Proton bunch time distribution.

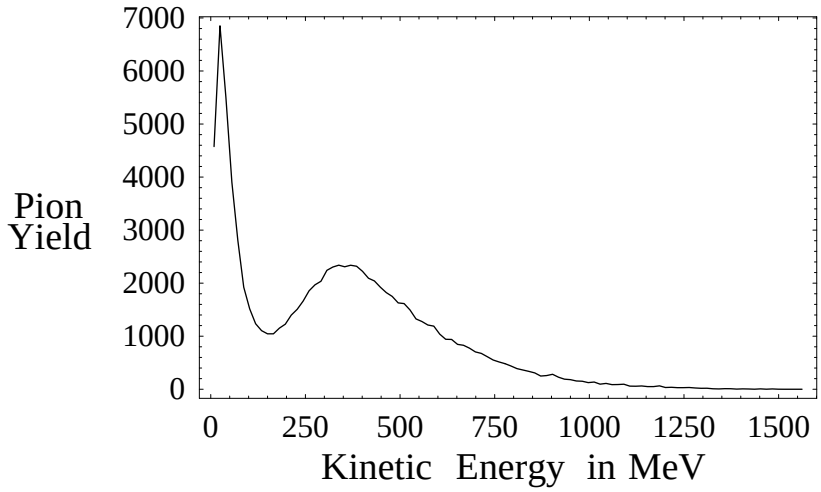


Figure 6.2: Pion spectrum at the horn exit.

## 6.4 Decay channel

Downstream of the collector a pion decay channel is located, which is usually of a solenoidal structure. In the CERN scheme after the horn capture there is a solenoidal channel of the uniform magnetic field, 30 m in length. In the American design the solenoidal field is adiabatically reduced to achieve the average transverse momentum reduction due to approximate conservation of adiabatic invariants [40]. In the CERN scheme the required reduction in angle is performed directly at the horn, which is a point to parallel imaging optical device.

The choice of the solenoidal focusing is motivated by minimization of the emittance growth due to pion decay. It can be shown that an instantaneous transverse emittance growth is proportional to a value of $\beta_t$ at the given point. The uniform solenoidal channel is capable of providing the smooth beta function all along the channel simultaneously in both planes. Here we have to mention another design [41], based on an AG lattice, where the emphasis is put on multichannel capture and its further recombination in the funneling scheme in order to reduce the integrated power per target and to increase its lifetime.

The length of the decay channel is defined by the pion and the muon life

time and is a compromise between the high pion to muon transition and low relative muon losses. Fig. 6.3 shows the length at which 90 % of pions have decayed as a function of the initial pion energy. The physics behind it is described by the simple exponential decay:

$$\frac{N_\pi(s)}{N_\pi(0)} = e^{-\frac{s}{c(\beta\gamma\tau)_\pi}} \tag{6.1}$$

For optimization of the decay channel length the problem can be described by the system of coupled ordinary differential equations relating change of number of pions and muons with distance:

$$\frac{dN_\pi}{ds} = -\frac{N_\pi}{c(\beta\gamma\tau)_\pi} \tag{6.2}$$

$$\frac{dN_\mu}{ds} = -\frac{dN_\pi}{ds} - \frac{N_\mu}{c(\beta\gamma\tau)_\mu} \tag{6.3}$$

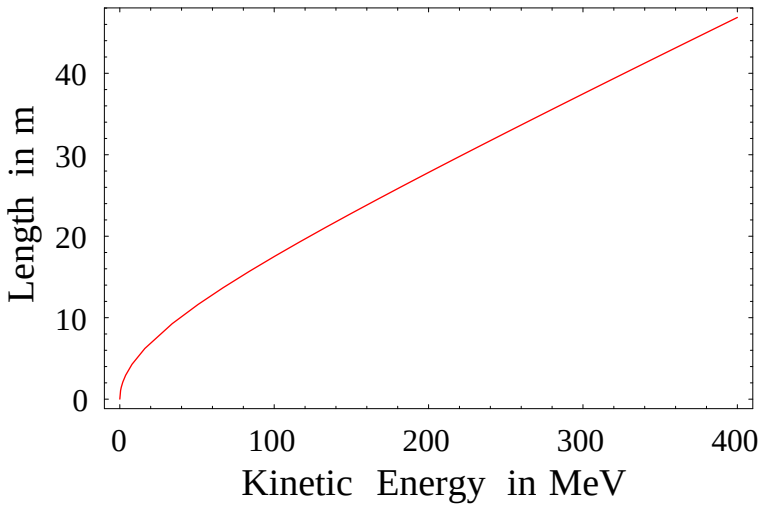


Figure 6.3: Length at which 80 percent of pions decay, versus energy.

The magnetic field of 1.8 T was chosen as limiting value for normal conducting solenoids. The higher value could be achieved using superconducting magnets but the use of this technique in the part of the decay channel close to the target is challenging due to a very high energy deposition. The muon

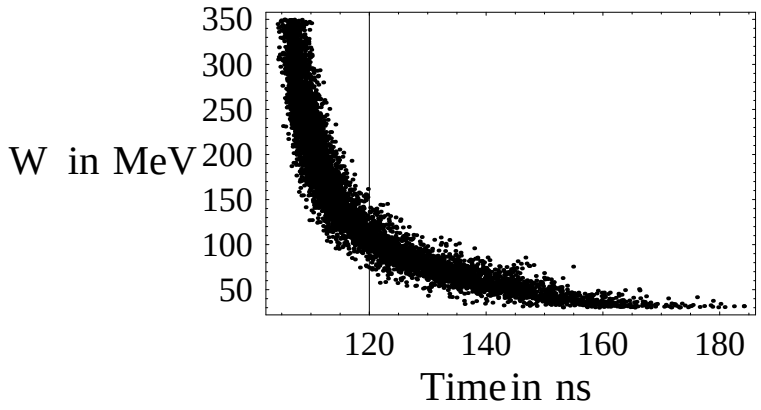


Figure 6.4: Longitudinal portrait of muon beam at the exit of the decay channel.

beam at the output of the decay channel, projected in the longitudinal and the horizontal planes is shown in Fig. 6.4 and Fig. 6.5, respectively. We have assumed the radius of the beam pipe in the decay channel of 30 cm. The beam growth in length can be seen due to variation of speed with energy, combined with the process of pion decay comparing longitudinal beam portraits at the output of the decay channel with the proton beam time distribution at the target.

## 6.5 Parameters of the muon bunch

We start by reminding the kinematics of pion decay. The kinetic energy of the muon is related to parameters of the pion moving on the reference axis in the laboratory system by the following formula:

$$E_{\mu tot} = \gamma_\pi (E_1 + \beta_\pi P_1 cos\theta) - m_\mu \tag{6.4}$$

where $E_1$ and $P_1$ are muon total energy and momentum in the pion rest frame and are given by:

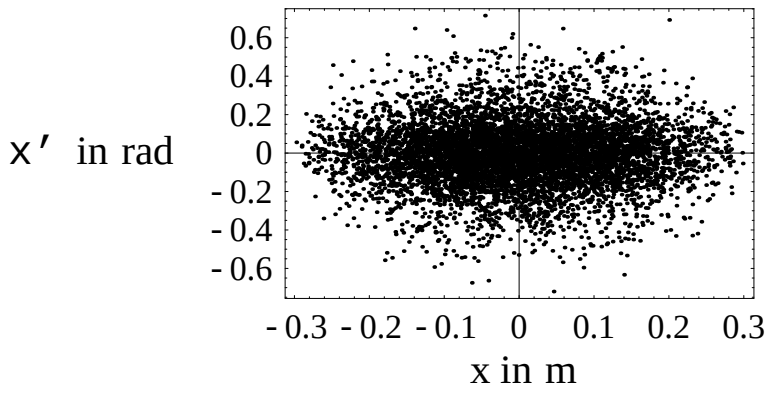


Figure 6.5: Transverse phase space of muon beam at the exit of the decay channel.

$$E_1 = \frac{m_\pi^2 + m_\mu^2}{2m_\pi} \qquad P_1 = \frac{m_\pi^2 - m_\mu^2}{2m_\pi} \tag{6.5}$$

The angle $\theta$ between the z axis and the muon momentum vector in the pion rest frame belongs to values contained in the interval of $\pm\pi$. We observe that there exists a kinematically allowed energy region for pions to decay into the given kinetic energy muon. The extreme values for this region correspond to forward and backward decay in the pion rest frame or values of $\theta$ $\pm\pi$. From this we can deduce that the maximal time of flight of the given energy muon at the exit of 30 m decay channel corresponds to the lowest allowed kinetic energy pion, which decays forward into the muon at the end. Furthermore, the minimal time is given by the flight of the maximal kinetic energy pion, which decays backwards thus creating the muon at the exit of decay channel. Here we assume, that the muon energy band is within pion energy band. With this result in hand we will estimate the orientation of a muon bunch at the input of phase rotation in order to deduce the effective input angle in the phase-energy plane. We can also calculate the total kinematically allowed longitudinal phase space volume for the given muon energy range.

The method mentioned above overestimates the real required longitudinal acceptance, because it does not take into account the statistical character of the decay. In other words, it calculates the total allowed volume, without taking into account the fact that probabilities of decay into the regions close to boundaries vanish. This problem is addressed in [43a]. Nevertheless, the estimation of the total longitudinal muon emittance can be of interest. The pion time of flight can be calculated from the formula:

$$T(E_{tot}) = \frac{L}{c\beta_\pi(E_{tot})} \tag{6.6}$$

To evaluate the kinematically allowed region we evaluate $\beta_\pi$ corresponding to the forward and backward decay as a function of the muon kinetic energy. We obtain the double-valued function. To calculate the value of the total longitudinal emittance, we integrate over the given energy interval and take into account finite duration of the initial pion bunch:

$$\pi\epsilon_L = \int_{E_{tot}^{min}}^{E_{tot}^{max}} (\frac{L}{c\beta_\pi^{min}} + \Delta T - \frac{L}{c\beta_\pi^{max}}) dE_{tot} \tag{6.7}$$

We can separate from the above equation the contribution from the pion initial emittance and the contribution coming from the pion decay:

$$\pi\epsilon_L = \pi\epsilon_0 + \pi\epsilon_{decay} \tag{6.8}$$

$$\pi\epsilon_0 = \Delta T \Delta E_{tot} \tag{6.9}$$

$$\pi\epsilon_{decay} = \frac{L}{c}\int_{E_{tot}^{min}}^{E_{tot}^{max}} (\frac{P_1^2 + E_{tot}^2}{E_{tot}\sqrt{E_{tot}^2 + P_1^2 - E_1^2} - E_1 P_1} - \frac{P_1^2 + E_{tot}^2}{E_{tot}\sqrt{E_{tot}^2 + P_1^2 - E_1^2} + E_1 P_1}) dE_{tot} \tag{6.10}$$

where L is the length of the decay channel (30 m), $\Delta T$ is the total initial time length of the pion bunch at the production target (4 ns) and $E_1$, $P_1$ were explained in equations 6.5. In the above calculation, we simply expressed $\beta_\pi^{max}$ and $\beta_\pi^{min}$ as a function of the muon total energy E. After integration the final result is:

$$\pi\epsilon_L = \Delta T \Delta E_{tot} + 2\frac{L}{c} P_1 (ArcTanh(\frac{E_{tot} - \frac{1}{2}\Delta E_{tot}}{E_1}) - ArcTanh(\frac{E_{tot} + \frac{1}{2}\Delta E_{tot}}{E_1})) \tag{6.11}$$

# Chapter 7

# Longitudinal capture

The longitudinal plane requires a special attention in the muon front end to maximize the muon transmission. The initial muon beam created at the end of the decay channel has a very large momentum spread and its shape in longitudinal plane is filamented. To avoid large losses, special longitudinal bunch manipulations were proposed to match the muon beam to a stable accelerating bucket for cooling or acceleration. They act on momentum spread, time spread or even on the time microstructure of the muon beam. In this chapter we describe RF phase rotation, magnetic bunch compression and bunching.

## 7.1 Principle of phase rotation

The beam at the exit of the decay channel has extremely large momentum spread, (Fig. 6.4). The change of tune for off-momentum particles would create a large mismatch in the downstream part of the machine and a beam loss. Even if we manage to transport this beam through the transport channel without transverse losses, which could be possible for example assuming a constant uniform solenoidal channel, the limitations of the longitudinal acceptance would nevertheless lead to beam loss during acceleration or cooling. The height of the separatrix of an accelerating bucket, which defines the stable part of the longitudinal phase space, is limited by the voltage applied.

Phase rotation uses the correlation between an arrival time in the RF cavities and momentum (energy) deviation to obtain a beam with lower energy spread. The time-energy correlation has already been created in the decay

channel and can eventually be increased in an additional drift section. The RF phase is fixed at zero angle at the reference capture energy, which gives zero acceleration, but particles with positive and negative energy deviation receive deceleration and acceleration respectively. From here we assume that zero phase corresponds to zero RF gradient. The beam continues to increase further in length or in phase, but energy deviation is reduced. The process is continued until the energy spread is exchanged with the time spread, which can be treated as an ultimate limit for the procedure. In addition, the beam can reach the nonlinear part of the RF voltage, which creates the filamentation limiting the applicability of procedure to less than half the RF period ($\pi$ in phase variable ). We illustrate the working principle of the phase rotation in Fig. 7.1, showing evolution of the longitudinal portrait of the bunch. The idealized elliptical bunch at the input of the phase rotation section is relatively short as compared to the stable bucket but with the very large energy spread represented by the red ellipse in Fig. 7.1 is injected into the phase rotation section. Its evolution is seen as a blue ellipse with smaller energy spread but larger time spread. The final black ellipse at the exit of the phase rotation has a much smaller energy spread, than the initial red ellipse.

## 7.2 Phase rotation as 1/4 synchrotron wavelength transformation

A convenient way of looking at the phase rotation is to treat it as a quarter synchrotron oscillation wave-length transformation. The formula for the synchrotron oscillation wave-length was derived in chapter 4. We quote it divided by 4:

$$\frac{\Lambda_s}{4} = \frac{1}{2}\pi(-\frac{\omega_{RF} q E_0 T_t}{m_0 c^3 \beta_s^3 \gamma_s^3})^{-\frac{1}{2}} \tag{7.1}$$

The value of $\Lambda_s$ corresponds to the length of a linac phase rotation section, which is built of RF cavities of frequency $\frac{\omega_{RF}}{2\pi}$, mean RF gradient $E_0$ and reference energy corresponding to relativistic factors $\beta_s$ and $\gamma_s$. This phase rotator is supposed to rotate the upright bunch by $\pi/2$ in the longitudinal phase space. Scaling laws for the rotator can be written:

$$\Lambda_s \sim (\beta_s \gamma_s)^{\frac{3}{2}} \qquad \Lambda_s \sim E_0^{-\frac{1}{2}} \qquad \Lambda_s \sim f^{-\frac{1}{2}} \tag{7.2}$$

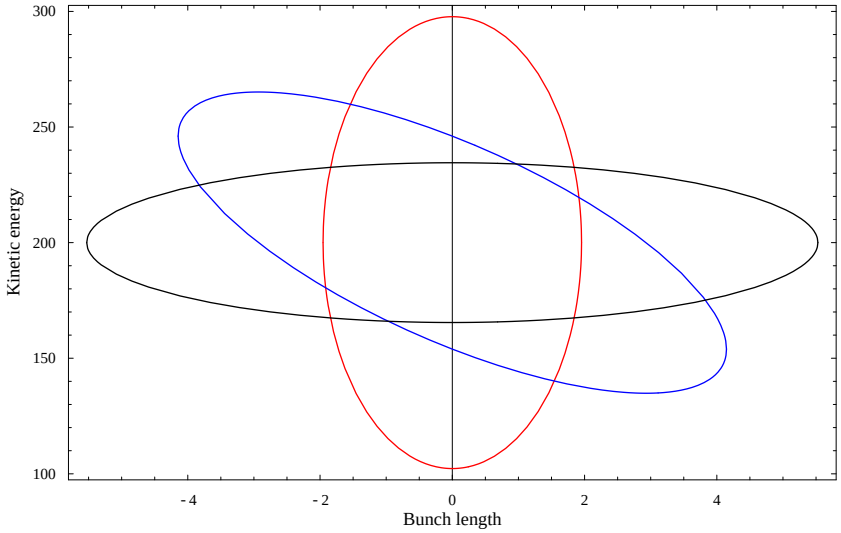


Figure 7.1: Phase rotation principle. The initial idealized bunch (red ellipse) with large energy spread is transformed into a long bunch with smaller energy spread (black ellipse). The blue ellipse shows a intermediate state of the process. The effect of the rotation in the longitudinal plane can be clearly seen.

where for every formula we vary only one variable, treating others as constants. Usually, in the neutrino factory studies, RF gradients are close to the sparking limit. There exists an empirical parameterization of the achievable gradient called the Kilpatrick limit, but the real limitation depends on the technical details of the RF design. The Kilpatrick limit [42] relates the surface gradient near the sparking limit to the frequency of a cavity:

$$f_{RF} = 1.643 E e^{-\frac{8.5}{E}} \tag{7.3}$$

where f is in MHz and E in MV/m. With present day designs the field can exceed the Kilpatrick limit up to a factor 2. The accelerating gradient is related to the maximal field by a geometrical factor. For example, the CERN 88 MHz cavity is set at 2.3 Kilpatrick which corresponds to about 10.8 MV/m and the real accelerating gradient in the structure is 4 MV/m.

To situate the phase rotation of a neutrino factory in the context of existing schemes, it is interesting to take the characteristics of the proposed RF cavities. The RF gradient is a function of RF frequency. For this purpose

we take the 7 MHz, 0.7 MV/m RF from the Japanese NuFact studies, 44 MHz, 2 MV/m and 88 MHz 4 MV/m adopted in the CERN scenario and 200 MHz 10 MV/m proposed in the American designs. Fig 7.2 shows the dependence of the RF gradient as a function of frequency. One can argue, that one should use more physical parametrization based on the Kilpatrick limit, but the real limit depends on details of cavity construction ( for example room temperature vs superconducting, surface treatment etc.) and it is more complicated, than the single Kilpatrick curve. Nevertheless it is interesting to use proposed gradients to study the phase rotation. We assume that the mean gradient in the rotator corresponds to the value quoted above. We assume a lattice with superimposed RF cavities and focusing elements, which enables very high packing of cavities and high avaraged RF gradient. Fig 7.3 shows the quarter synchrotron wave-length as a function of frequency for 200 MeV, 180 MeV and 130 MeV kinetic energies for muons. In Fig 7.4 the quarter synchrotron wave length is plotted as a function of energy.

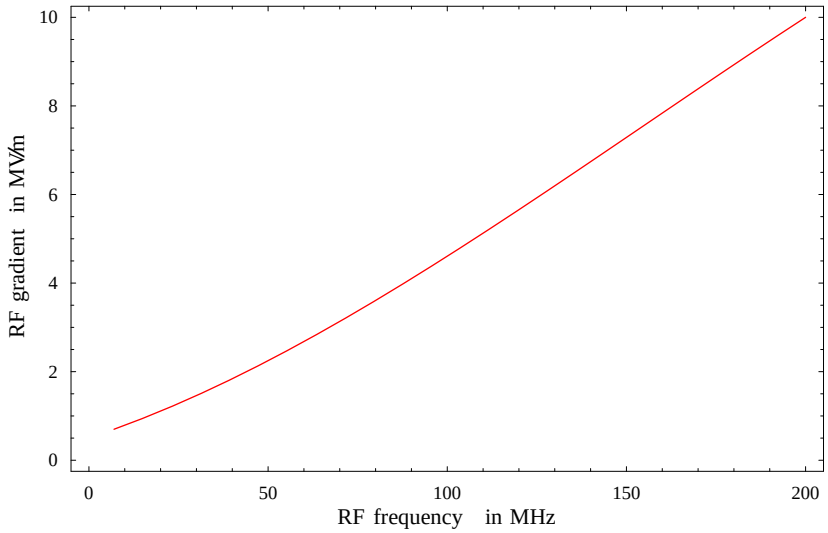


Figure 7.2: Parameterization of the gradient used in Nufact studies.

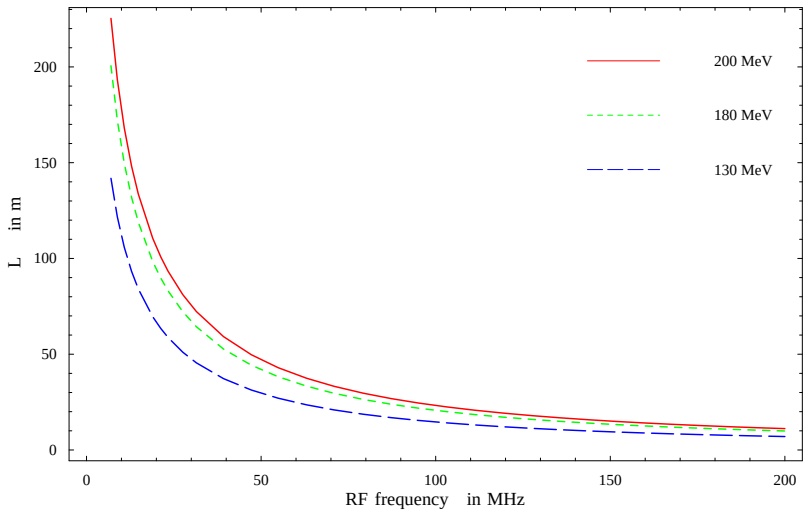


Figure 7.3: Variation of quarter synchrotron wave-length with RF frequency.

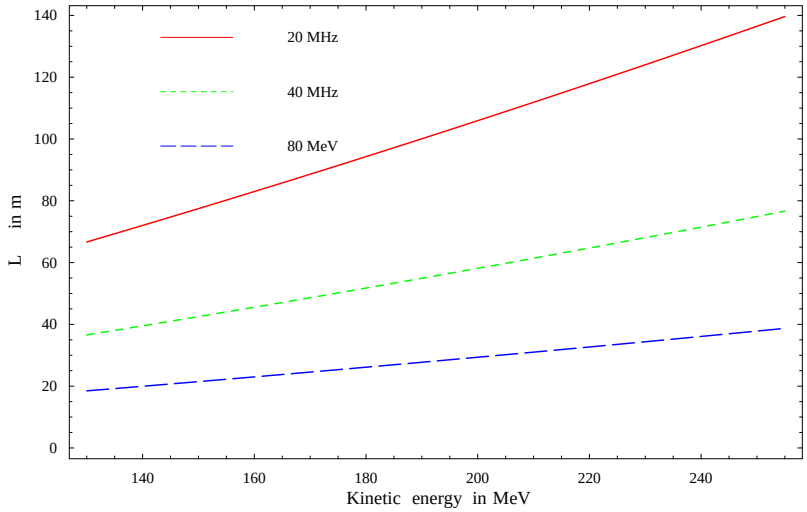


Figure 7.4: Quarter synchrotron wave-length as a function of energy.

## 7.3 Length of phase rotator

The shape of longitudinal portrait of the muon beam at the end of decay channel is not an upright ellipse (Fig. 6.4). The realistic muon beam at the

exit of the decay channel is effectively rotated and we have to take this effect into account in order to estimate the length of the phase rotation section.

The shape of the muon bunch can be obtained by calculating the boundaries of the allowed region. To estimate the effective orientation of the muon bunch, we take the arithmetic mean value corresponding to both boundaries. The mean arrival time of a muon at distance L from the target is given by:

$$T_{mean} = \frac{L}{c} \frac{E_{tot}(P_1^2 + E_{tot}^2)\sqrt{P_1^2 - E_1^2 + E_{tot}^2}}{E_{tot}^2(P_1^2 - E_1^2 + E_{tot}^2) - E_1^2 P_1^2} \tag{7.4}$$

From the above equation the value of $\frac{dT}{dE_{tot}}$ at the exit of the decay channel can be estimated.

The linearized solution to the longitudinal dynamics can be represented by:

$$\Delta\phi(s) = \Delta\phi_{max} sin(\int_0^s \frac{2\pi ds}{\Lambda_s} + \phi_0) \tag{7.5}$$

From the above equation the approximate angle of the bunch at the exit of the decay channel can be estimated. Note that the angle is different for positive and negative values of $\Delta W$, resulting from velocity variation with energy. This dependence vanishes for ultrarelativistic energies. Working with linearized dynamics it is convenient to calculate the angle in the ($\delta\phi$, $\delta W$) plane at the value of the reference energy. The length of the phase rotation is given by:

$$s = \frac{\Lambda_s}{2\pi} ArcSin(\frac{\frac{dT}{dE_{tot}}\frac{2\pi}{T_{RF}}}{\sqrt{(\frac{dT}{dE_{tot}}\frac{2\pi}{T_{RF}})^2 + \frac{a^2}{b^2}}}) + \frac{\Lambda_s}{4} \tag{7.6}$$

where $T_{RF}$ is the RF period and $\frac{dT}{dE_{tot}}$ is calculated at reference energy. The coefficients $a^2$ and $b^2$ are defined as follows:

$$a^2 = \frac{\omega_{RF}}{m_\mu c^3 \beta_s^3 \gamma_s^3} \qquad b^2 = qE_0T \tag{7.7}$$

Fig. 7.5 shows the length of phase rotation for 200 MeV and 180 MeV kinetic energy as a function of RF frequency assuming gradient as in Fig 7.2. Note, that $\frac{dT}{dE_{tot}}$ is negative, so the first term in the equation 7.6 is negative too.

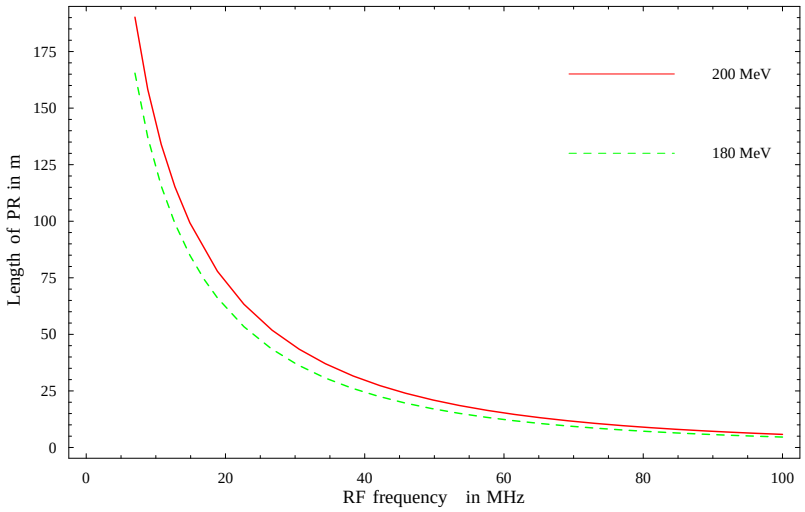


Figure 7.5: Length of the phase rotation linac.

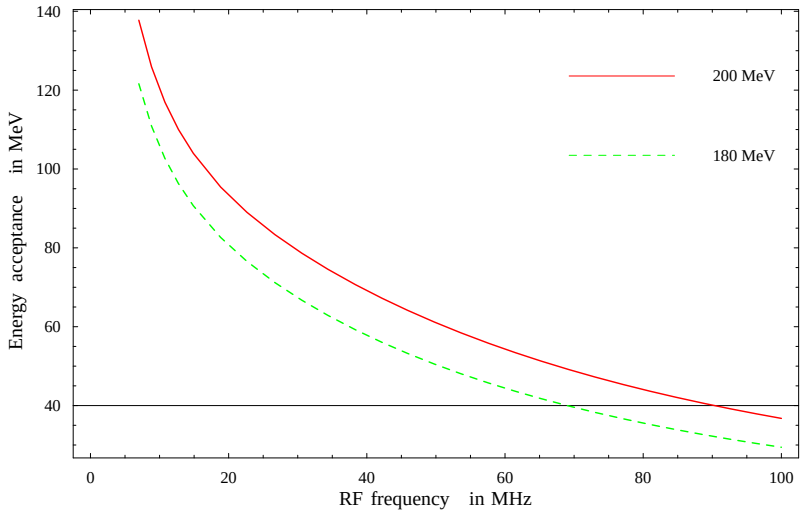


Figure 7.6: The phase rotation energy acceptance.

## 7.4 Energy acceptance of phase rotation

The efficiency of phase rotation depends on the ability to rotate the high energy spread into the stable accelerating RF bucket for cooling or accelera-

tion. The phase rotation is limited to less than half an RF period because of a nonlinearity in the longitudinal dynamics due to sine-like voltage variation. The ratio of the ellipse axes in the linear theory can be expressed by:

$$\frac{\bar{W}}{\bar{\phi}} = \frac{b}{a} \sim (\beta_s \gamma_s)^{\frac{3}{2}} \tag{7.8}$$

The real energy acceptance is calculated in the same way as the effective bunch shape at the exit of the decay channel. The effect is again related to the effective rotation of the bunch. This effect limits the real energy acceptance of the phase rotation. To estimate the energy spread, which can be phase rotated, we calculate the intersection of the ellipse in the $(\Delta\phi, \Delta W)$ plane with the straight line tangent to the muon bunch at zero phase, see Fig. 7.7. The phase at the point of intersection is then given by:

$$\Delta\phi_a = \frac{(\frac{\Delta\phi}{\Delta W})_0 \Delta\phi_{max}}{\sqrt{(\frac{\Delta\phi}{\Delta W})_0^2 + \frac{a^2}{b^2}}} \tag{7.9}$$

Using the relation between phase and time:

$$\Delta\phi = \Delta T \frac{2\pi}{T_{RF}} \tag{7.10}$$

where $T_{RF}$ is the RF period, the energy spread, which can be phase-rotated is:

$$\Delta W_a = \sqrt{\Delta W_{max} - (\Delta\phi_a)^2 \frac{b^2}{a^2}} \tag{7.11}$$

The ratio $(\frac{\Delta\phi}{\Delta W})_0$ is calculated at the centre of the $(\Delta\phi, \Delta W)$ plane, $\Delta\phi_{max}$ and $\Delta W_{max}$ corresponds to the ellipse axes, see Fig.7.7. $\Delta\phi_{max}$ is set at $(\frac{9}{10}\pi)$, which is a little less than half an RF period. The $\Delta W_{max}$ is calculated from equation 7.8 where we set $\bar{\phi}$ at $(\frac{9}{10}\pi)$. In reality the dynamics is nonlinear due to the sine shape voltage and asymmetric for the positive and negative energies because of a paticle speed variations. In addition, the optimized solution can be affected by the muon distribution and a solution with slightly over-rotated bunch may be obtained. Nevertheless, the linearized parameterization is interesting to design the scheme and get a first approximation of the parameters. In Fig. 7.6 the energy acceptance of the phase rotation is shown as a function of RF frequency for 200 and 180 MeV kinetic energies.

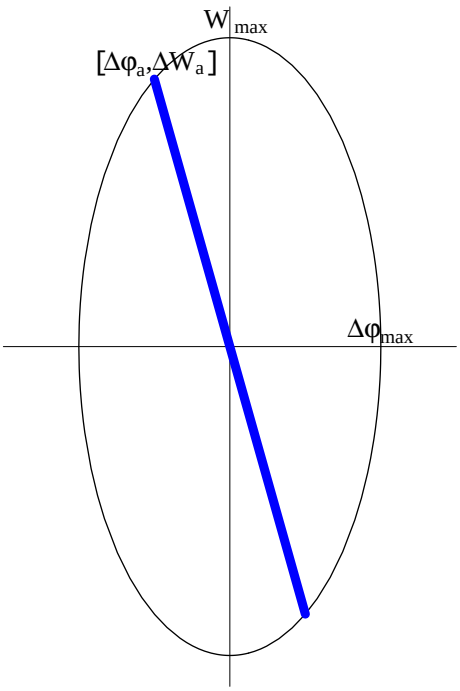


Figure 7.7: The blu line represents an idealized muon bunch at the exit of the decay channel. It crosses the ellipse describing the boundaries of stable longitudinal motion at $\Delta\phi_{max} = \frac{9}{10}\pi$.

We can calculate the longitudinal emittance of the muon bunch for the given energy acceptances as a function of the frequency using the results of the previous chapter. But, as mentioned in the previous chapter, the method highly overestimates the result, so we apply a more pragmatic approach. In practice, the emittance given in equation 6.11 is scaled by a factor k of the order of 0.5. Fig 7.8 show the longitudinal emittance of the bunch, which can be successfuly rotated by the phase rotation for 200 MeV reference kinetic energy compared with the longitudinal acceptance of the accelerating bucket as a function of frequency at $\pi/4$ reference phase. Here, we can formulate the so called longitudinal phase space problem, which states that within the bunch to bucket principle the acceptance of an accelerating bucket is insufficient to accept the muon bunch successfully rotated in phase rotation for wide range of RF frequencies. Similar calculations of the muon beam longitudinal emittance can be found in [43]

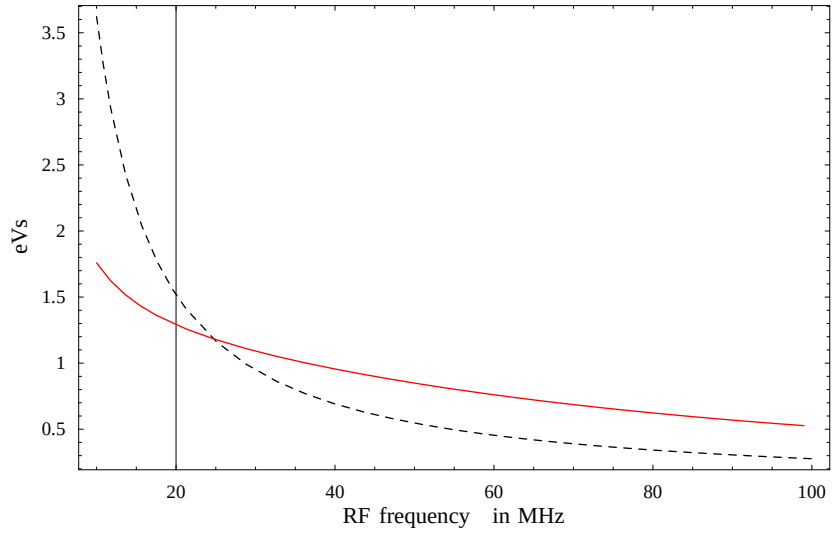


Figure 7.8: Bunch and bucket longitudinal areas versus RF frequency. The dashed and the solid lines describe longitudinal areas of the accelerating bucket at $\pi/4$ and the muon bunch, respectively.

## 7.5 Longitudinal matching to an accelerating bucket

The longitudinal phase space problem can be formulated again by calculating the final $\Delta W$ after phase rotation and comparing it with the energy acceptance of an accelerating bucket at $\pi/4$. We calculate it by assuming a muon bunch rectangular in shape. Knowing its area and length $(\frac{9}{10}\pi)$ we can calculate its half width in energy spread (Fig 7.9). We see that below 70 MHz within our approximation bucket height is higher than the rotated bunch. This means that bucket is filled only partialy. To avoid longitudinal blow up during acceleration or cooling the voltage could be lowered to match the beam into the bucket, but as we want to collect as much muon current as possible we instead search for a solution to optimize bucket filling. A possible solution could be to increase a frequency of all or part of a set of RF cavities in the phase rotation to second harmonic with respect to an accelerating RF. For this scheme, the muon train time structure corresponds to the accelerating RF. Another solution could be to apply a magnetic bunch

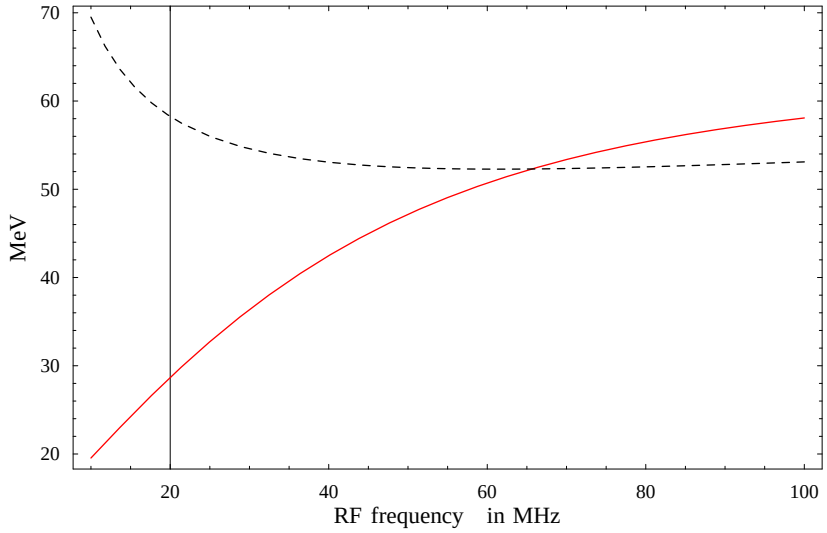


Figure 7.9: The dashed and the solid lines describe the "hight" of the accelerating bucket at $\pi/4$ and the muon bunch after phase rotation, respectively.

compression instead of the phase rotation or a combination of both to maximize the muon transmisson. The above solutions fit into the bunch to bucket principle. Another family of solutions can be developed by employing a concept of bunching to divide a big muon bunch into a string of microbunches fitting a downstream accelerating RF.

## 7.6 Phase rotation in the CERN reference scenario

We show the phase rotation in the case of the 44 MHz CERN scenario [44]. The reduction of the beam energy spread can be clearly seen by comparing the longitudinal portrait at the input and output as shown in Figs 7.11 and 7.12, respectively. The 44 MHz accelerating bucket at $\pi/4$ is drawn together with the phase-rotated beam. Thus one can observe that the bucket is too short to accept efficiently the beam, the bucket height being a little larger than the beam. We report briefly on the transverse dynamics and a cell structure. The solenoids are superimposed with the RF cavities to maximize the RF packing factor. The RF packing factor is the total length of RF

cavities divided by the total length of the phase rotation section. The lattice studied above consists of 21 1.4 m RF cavities with a total length of 29.4 m. The averaged gradient is 2 MV/m. The magnetic field varies from about 1.5 T outside to about 3.25 T within a body of 96 cm long solenoids. The layout of the cell and its approximate symmetric Larmor beta function are seen in Figs 7.13 and 7.10 respectively. The cell structure was developed in [45].

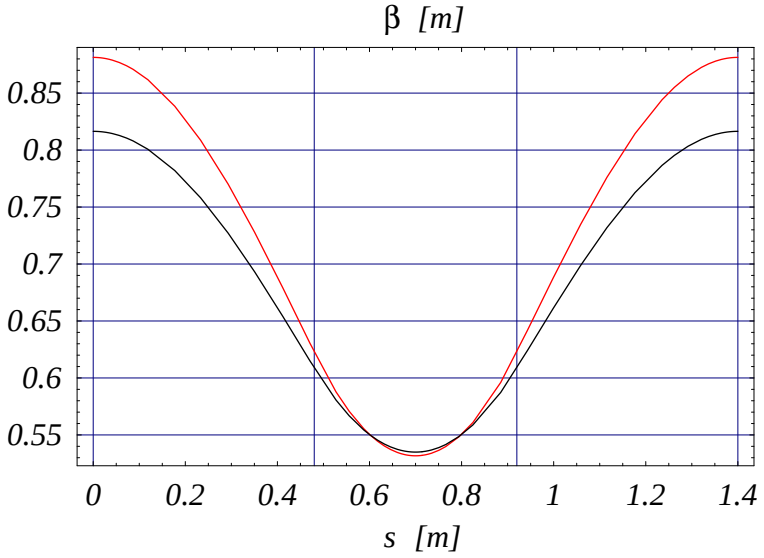


Figure 7.10: The Larmor $\beta_L$ function in the phase rotation cell in hard edge approximation. The red and black curve are calculated assuming zero and 1.5 T values of magnetic fields between solenoids respectively.

## 7.7 The second harmonic phase rotation

The idea of the second harmonic phase rotation is based on the simple observation that a longer bucket is needed to accept the muon bunch. We propose to act on a muon beam bunched at 44 MHz with 88 MHz RF system for phase rotation followed by longitudinal capture in 44 MHz accelearting RF system ( for cooling or direct acceleration). The higher voltage available at the higher frequency makes the length of the phase rotation shorter. According to the previous study, energy acceptance of the phase rotation is reduced with frequency, but some gain is expected due to better matching

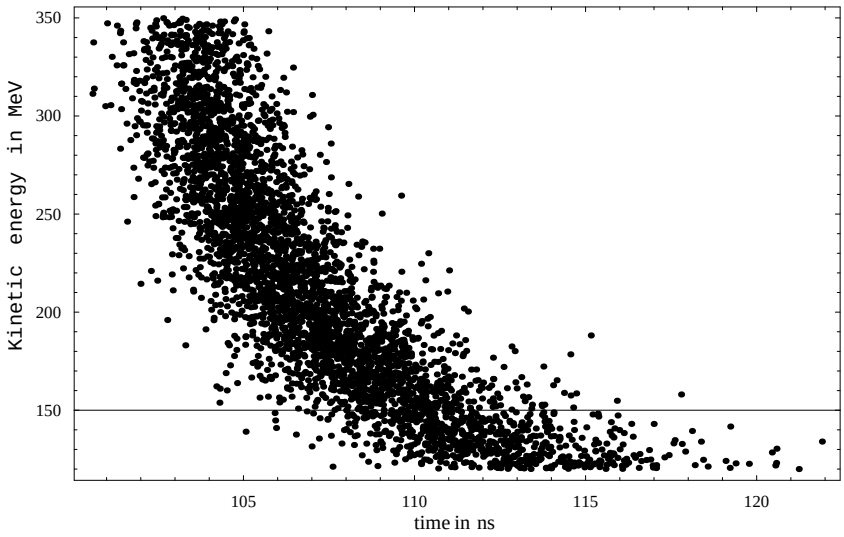


Figure 7.11: The muon beam at the end of decay channel.

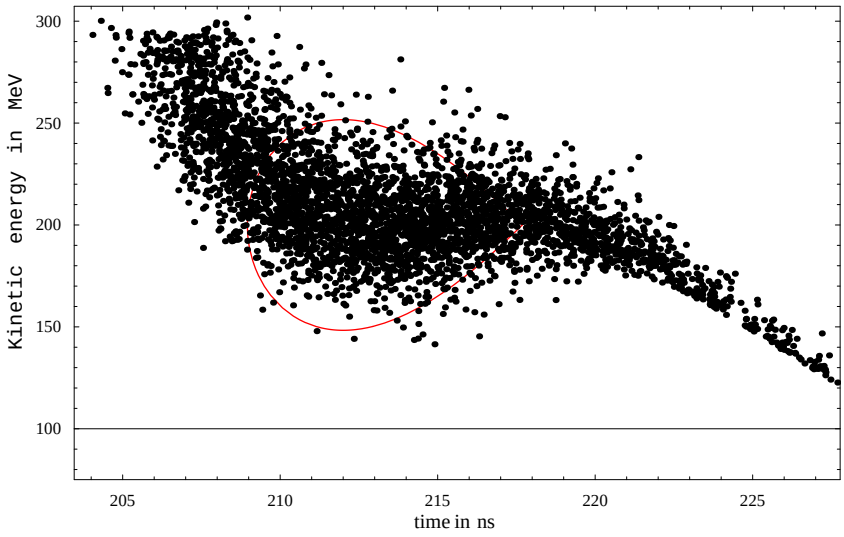


Figure 7.12: Longitudinal portrait of the muon beam at the exit of the CERN 44 MHz phase rotation section.

to the bucket. We study the phase rotation at 88 MHz 4 MV/m followed

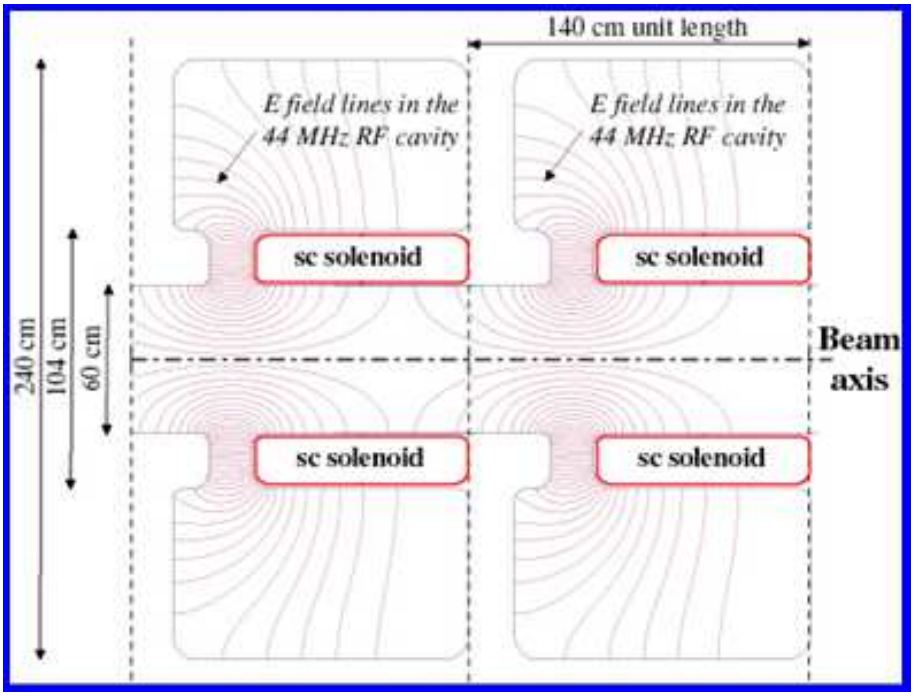


Figure 7.13: Layout of 44 MHz phase rotation cell. Note superimposed RF cavities and solenoids

by capture at 44 MHz accelerating bucket at $\pi/4$ phase and 2 MV/m. The longitudinal phase space after the second harmonic phase rotation is shown in Fig. 7.14 together with the 44 MHz bucket. Matching to the bucket is better than in the pure 44 MHz case (both for phase rotation and capture) by about 15 %. The higher efficiency is expected for the phase rotation located closer to the target, where the muon beam is shorter and better fits into the 88 MHz system, but RF acts on the beam with a higher admixture of pions. Then, pions decaying during the phase rotation can produce muons outside matched area in the longitudinal phase space. The final optimization of the proposed scheme is not possible without detailed information on the initial pion spectrum at the production target.

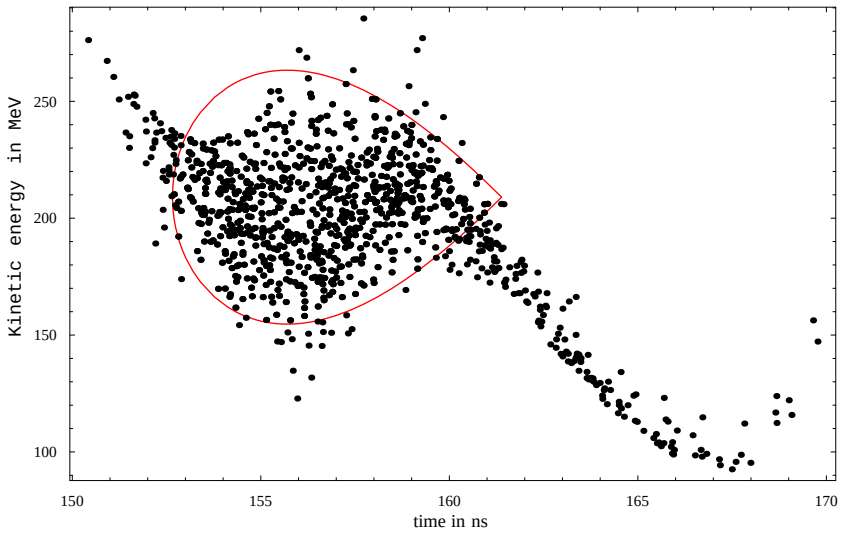


Figure 7.14: Muon bunch rotated with 88 MHz phase rotation system captured by 44 MHz accelerating bucket at $\pi/4$ phase (the second harmonic phase rotation).

## 7.8 Magnetic bunch compression

In order to achieve better matching and as a result higher muon transmission, we propose to act on the arrival time of particles with momentum deviation. Introducing dispersion by application of bending magnets creates the effect of different path lengths for off-momentum particles, which together with velocity variation results in arrival time variation. This effect in the linear approximation is described by equation 5.17. Phase rotation is used to reduce initially the energy spread, but keeping the correlation between the arrival time and energy deviation. We thus reduce the effective angle of rotation and number of RF cavities is reduced. The bunch should be rotated only to the energy spread corresponding to the accelerating bucket height, which was already given in Fig. 7.9. Then the required compression in phase is given by the following equation:

$$\Delta\phi_{BC} = \sqrt{W_{max}^2 - \Delta W_{bucket}^2 \frac{a^2}{b^2}} \tag{7.12}$$

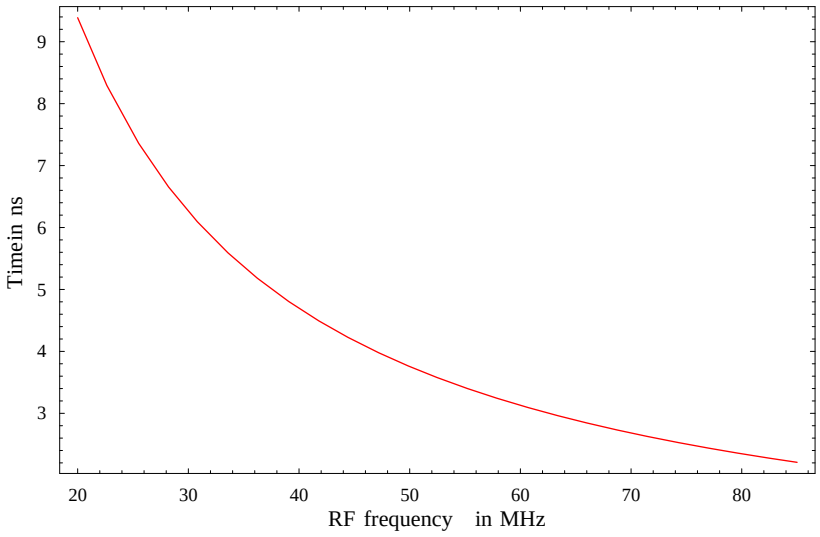


Figure 7.15: Required compression in time for various RF systems.

where $W_{max}$ corresponds to maximal energy amplitude in the motion described by the ellipse in 7.7 at $\frac{9}{10}\pi$ phase. We plot the amount of compression

needed for the various RF systems as a function of frequency assuming the previous gradient lows in Fig. 7.15. The length of phase rotation upstream of the compressor is adjusted to rotate the bunch to $W_{bucket}$.

We have studied the phase rotation with solenoidal focusing in[47] and in an AG triplet lattice. The choice of AG lattice in [48] was studied as a continuation of the AG applications in the decay channel studied in [41]. The detailed parameters differ in these two cases, but the general concept of bunch compression remains the same. Similar design was proposed independently in [49].

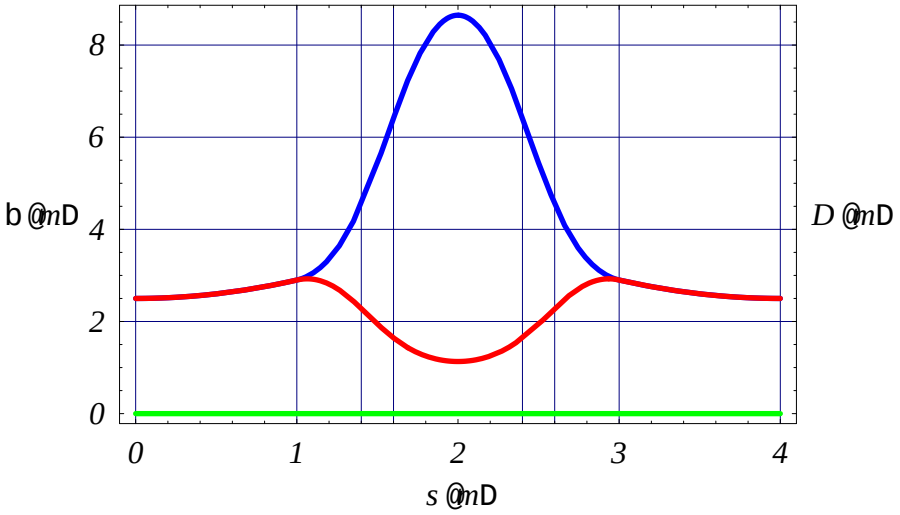


Figure 7.16: Optics in the single triplet cell. The red and blue lines are $\beta_x$ and $\beta_y$ functions, respectively.

We shall now give a brief description of the AG focusing line. The line for phase rotation has 2 cm acceptance. The magnetic field in the line is compatible with room-temperature magnets. To achieve a high RF packing factor, a triplet AG focusing structure was chosen, which offers long drifts with small $\beta_t$ values in both transverse planes. The optical functions in a single 4 m phase rotation cell are shown in Fig. 7.16. On both sides of the cell there is room for one 44 MHz cavity and packing factor is 1/2. The phase rotation channel consists of eight triplet cells. The phase rotation line contains 16 cavities with 2 MV/m peak gradient. The line consists of a matching section from the FODO decay channel, the phase rotation

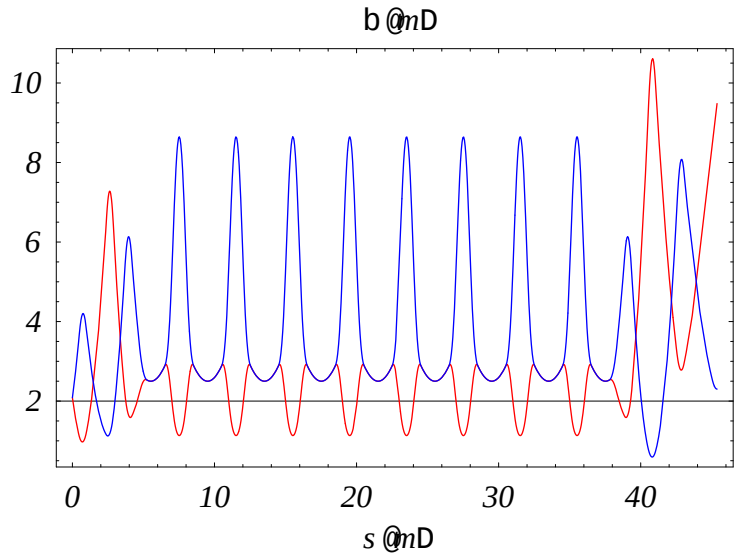


Figure 7.17: Optics in the phase rotation and the matching sections. The red and blue lines are $\beta_x$ and $\beta_y$ functions, respectively.

section and a matching section to the magnetic compressor chicane. Optical functions are shown in Fig. 7.17. The result of tracking the muon bunch through the phase rotation line is shown in Fig. 7.18. The reference particle was chosen at 200 MeV kinetic energy.

The principle of magnetic compression is based on lengthening of particle trajectories for off-momentum particles [46]. It can be achieved by the proper choice of $\gamma_T$ with respect to the relativistic $\gamma$ of the bunch center. We present now the example of matching a 44 MHz bucket with the combination of RF phase rotation. From the above calculations we obtain the required value of compression in time $\Delta T$ of about 4 ns. The phase rotation should rotate the initial bunch to $\pm 50$ MeV. The required amount of compression can be realized choosing $\gamma_T$ to be 1.76 with relativistic $\gamma$ of 2.89 for a reference muon of 200 MeV kinetic energy. The length of the compressor lattice is 26.4 m. The magnetic compressor chicane consists of two periods with one sign of the bending magnets each, which results in a zero total deflection angle. Each part consist of three FODO cells and is designed as an achromat. The appropriate value of $\gamma_T$ was achieved by the choice of deflection angle in three bending manets. Optical functions of the compressor chicane are shown in Fig. 7.21 and its layout in Fig. 7.22 respectively. The result of tracking in

the longitudinal plane in the compressor chicane together with the 2 MV/m 44 MHz accelerating bucket at $\pi/4$ synchronous phase is shown in Fig. 7.19. Comparison of Fig. 7.18 and Fig. 7.19 shows the compression of the bunch in length. Table 7.1 gives the magnet parameters.

The study of the transverse dynamics in the compressor shows the presence of strong geometrical and chromatical aberrations leading to emittance dilution. As an example, we show the horizontal tracking of the matched ellipse for on momentum (see Fig 7.23) and with momentum deviations of +10 % and - 10 % in Fig. 7.24 and 7.25, respectively. The deformation of the initial ellipse (the blue one) for the on-momentum is due to geometrical aberrations and a mismatch due to chromatic aberrations for the off-momentum cases. The result of tracking is described by the black ellipse. The center of the bunch is not matched to zero for off-momentum studies although the linear dispersion is matched to zero. This indicates the presence of the nonlinear dispersion, which is not matched to zero. We present now the result of tracking in the compressor with a sextupolar correction described by the red ellipse. The sextupoles were placed in the large dispersion region in the lattice. We managed to reduce the filamentation in the horizontal phase space and to match the off-momentum orbits to dispersion. The off-momentum orbits before and after corrections are presented in Figs 7.26 and 7.27 respectively. The sextupolar correction has a sizeable effect in the longitudinal plane, which can be seen in Fig. 7.20 . The remaining emittance dilution is still not negligible and could be reduced in the lattice with bending magnets different from sector magnets, which are responsible for large geometrical aberrations.

The tracking studies in this and all later chapters were performed using functions working with the BeamOptics code [27] written in the *Mathematica* [55] framework.

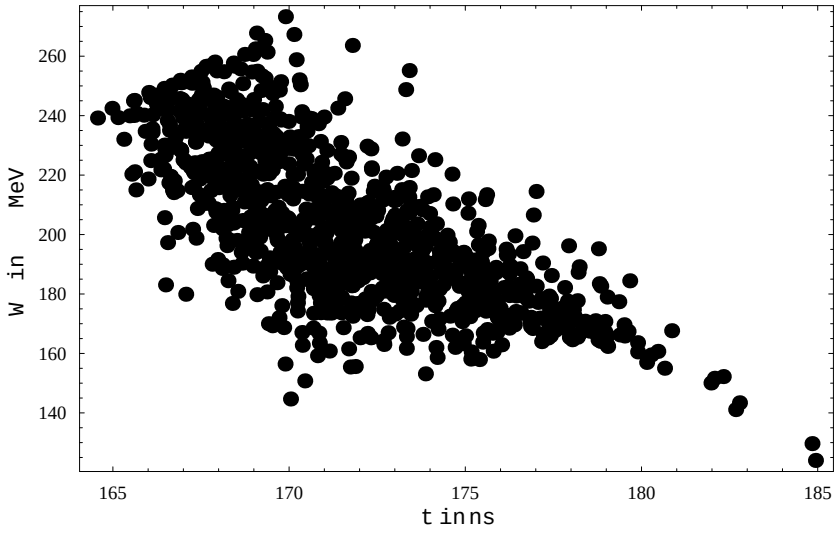


Figure 7.18: Longitudinal distribution after phase rotation.

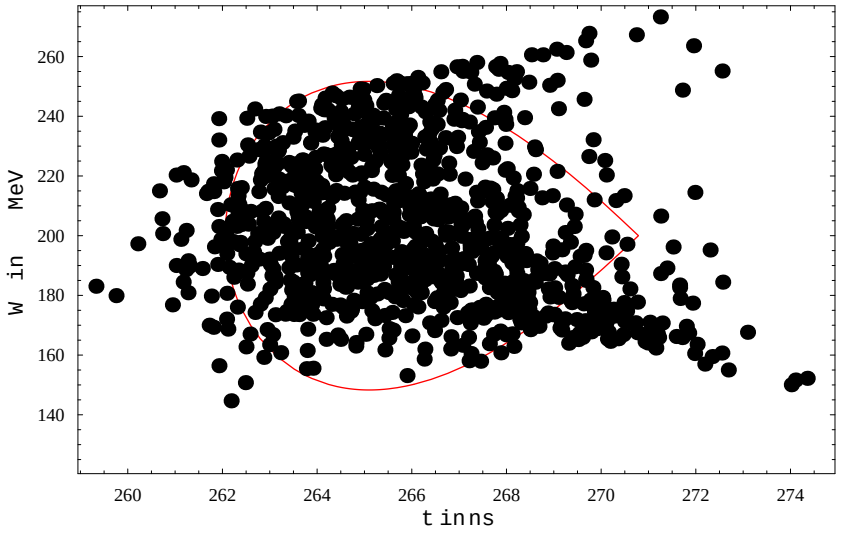


Figure 7.19: Longitudinal distribution after magnetic compression.

| | k $[m^-2]$ | $\beta$ [m] | g [T/m] | r [m] | B [T] |
|---|---|---|---|---|---|
| Triplet | 2.25<br>-1.79 | 4.5<br>8.5 | 2.15<br>- 1.71 | 0.3<br>0.41 | 0.64<br>0.7 |
| Matching sections | 1.94<br>1.4 | 7<br>10.5 | 1.85<br>1.34 | 0.37<br>0.45 | 0.68<br>0.6 |
| Compressor (quadrupoles) | 0.7 | 3.9 | 0.67 | 0.88 | 0.59 |
| Compressor (maximum bending) | - | - | - | - | 0.55 |

Table 7.1: Magnet parameters in the line for 2 cm acceptance.

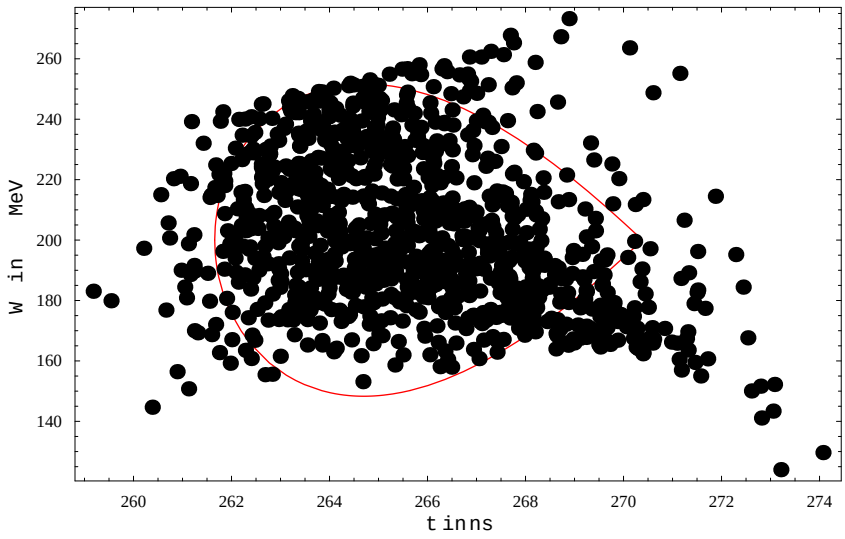


Figure 7.20: Magnetic compression with sextupolar correction

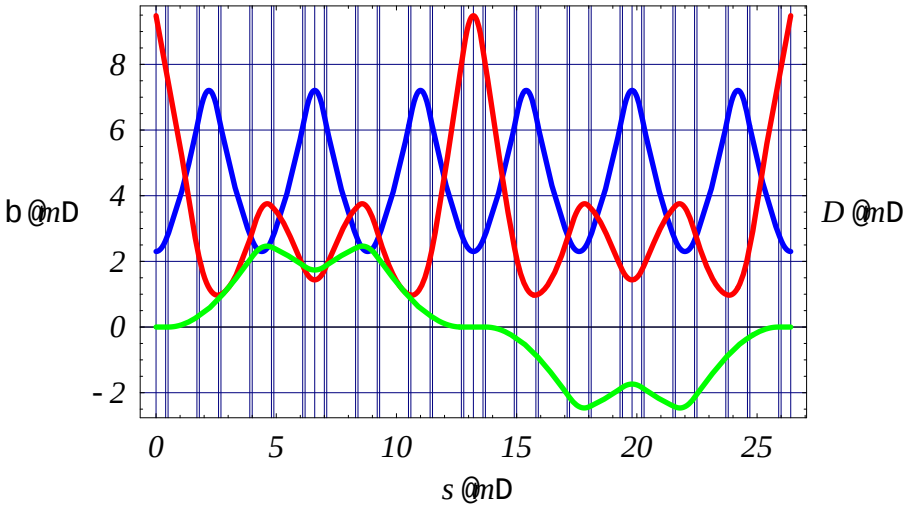


Figure 7.21: Optics in the compressor chicane. The red, blue and green lines are $\beta_x$, $\beta_y$ and $D$ functions, respectively.

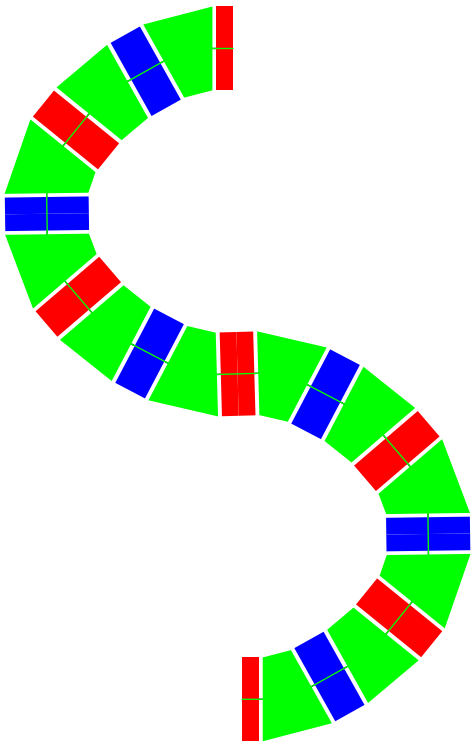

Figure 7.22: Layout of the compressor. The red and blue parallelograms correspond to the focusing and defocusing quadrupoles, respectively. The green polygons correspond to the sector bendings.

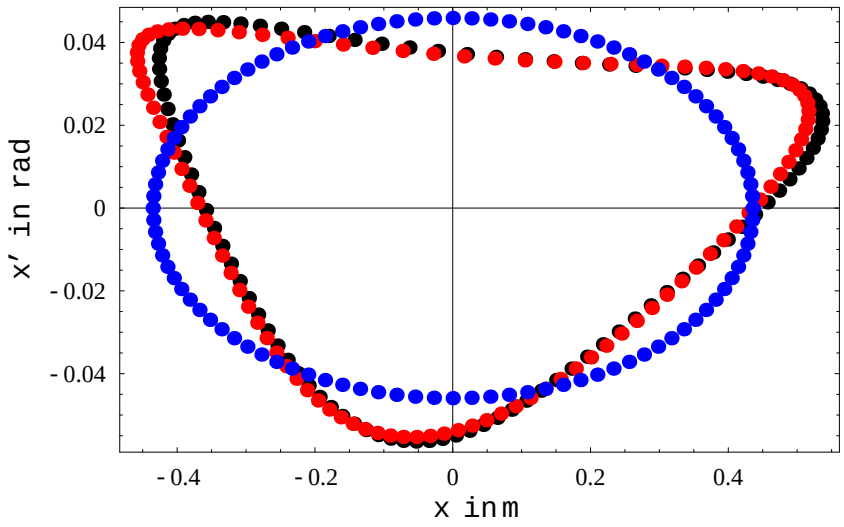


Figure 7.23: Horizontal phase spaces in the compressor for on momentum particles: initial (blue), final (black) and final with sextuoles (red).

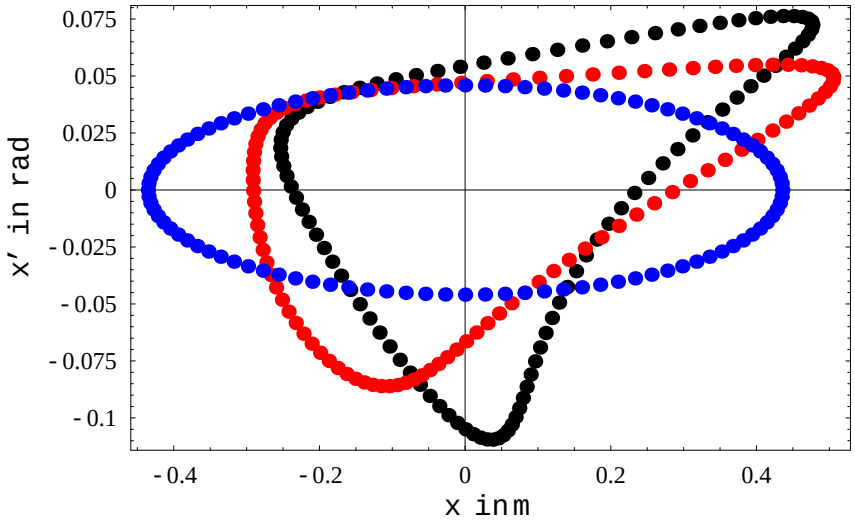


Figure 7.24: Horizontal phase spaces in the compressor for +10% momentum deviation: initial (blue), final (black) and final with sextuoles (red).

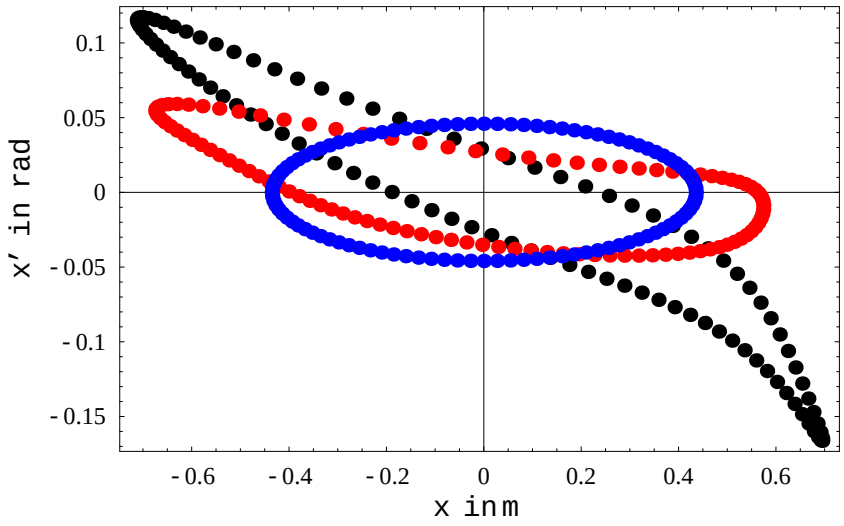


Figure 7.25: Horizontal phase spaces in the compressor for -10% momentum deviation: initial (blue), final (black) and final with sextuoles (red).

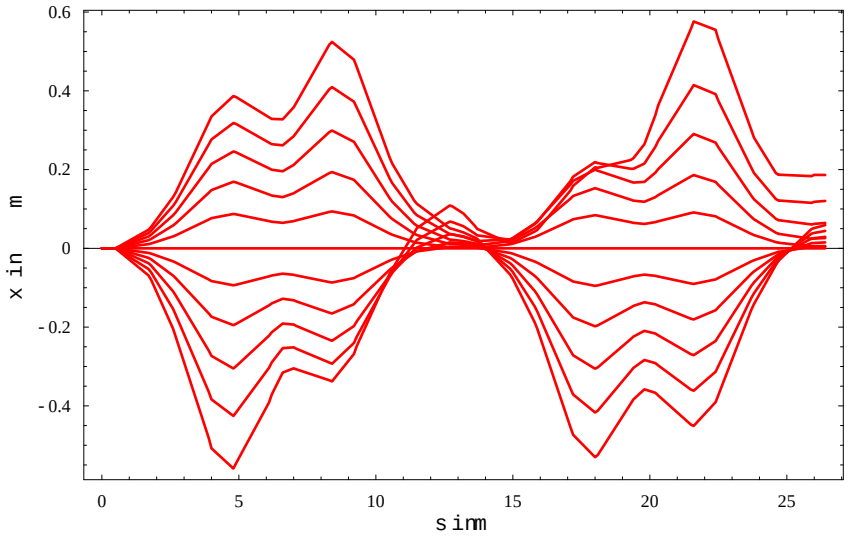


Figure 7.26: Off-momentum orbits in the compressor without sextupoles.

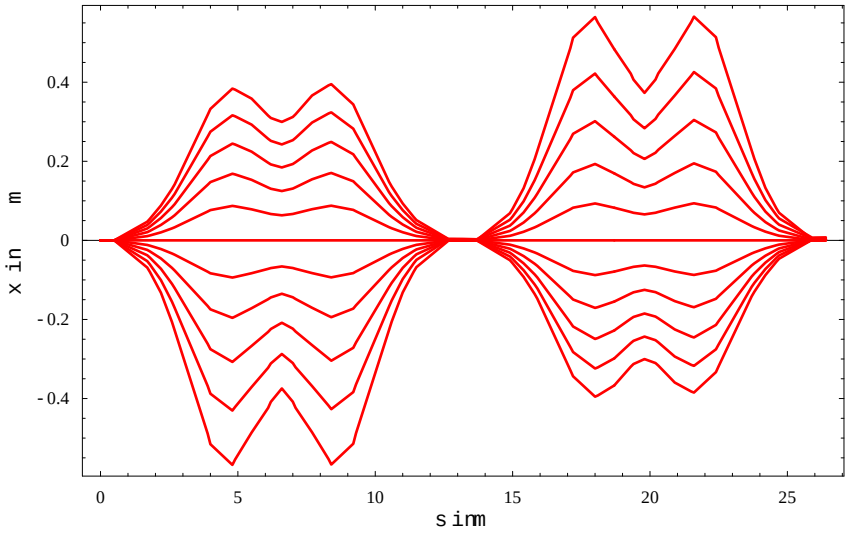


Figure 7.27: Off-momentum orbits in the compressor with sextupolar correction.

## 7.9 Bunching method

An alternative solution to the bunch-to-bucket principle is based on bunching the initial large muon bunch into a string of high-frequency microbunches. Muon front-ends in the American Study I [17] (with the double harmonic bunching) and II ( with Neuffer's adiabatic bunching) [36] are examples of this approach. A common feature of these proposals is a relatively low capture energy, which is motivated by the bunching. At lower energy the synchrotron oscillation wavelength is shorter and all longitudinal bunch manipulations can be done on a shorter distance. The disadvantage of Neuffer's approach is that the muon train is too long to be injected into any short (50-100 m) ring. Cost-effective designs require small rings for cooling or acceleration.

We are searching for the muon front-end capable of producing a short muon train out of the single muon bunch at the exit of the decay channel and of keeping large total longitudinal acceptance. As a solution, we propose conventional low-frequency phase rotation followed by bunching at high frequency similar to Study I scheme. We show the example of a 10 MHz, 1 MV/m, 100 m long phase rotation section followed by a 200 MHz 140 m long buncher linac, see Fig 7.30. The voltage is raised quadratically along the length of the linac to increase the bunching efficiency. We show a longitudinal plane after the beam passed the rotator in Fig. 7.28 and at the exit of the buncher in Fig. 7.29. The bunching efficiency achieved in this study is 73.6 %. The disadvantage of schemes with bunching is that linacs for both the low frequency rotation and the bunching are long. In Neuffer's case the initial drift following the decay channel mostly contributes to the length. In this light the solutions with bunching can be hardly called cost-effective, except for the RAL proposal, where the beam is bunched in a cooling ring and no special bunching linac is foreseen [50].

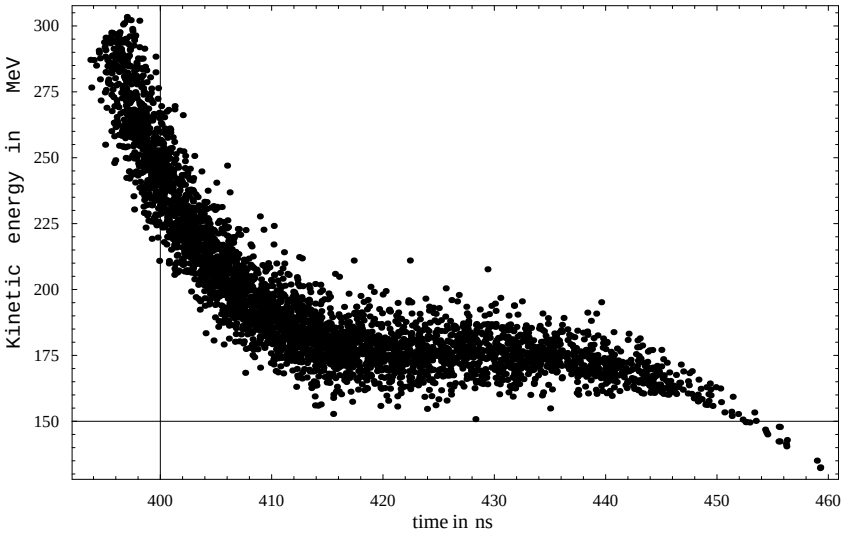


Figure 7.28: Muon beam at the exit of 10 MHz phase rotation.

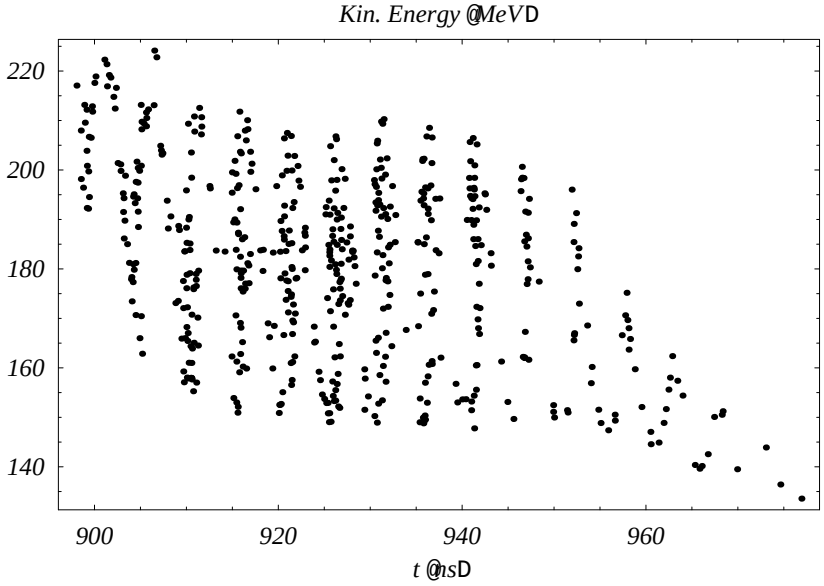


Figure 7.29: Muon beam at the exit of the buncher

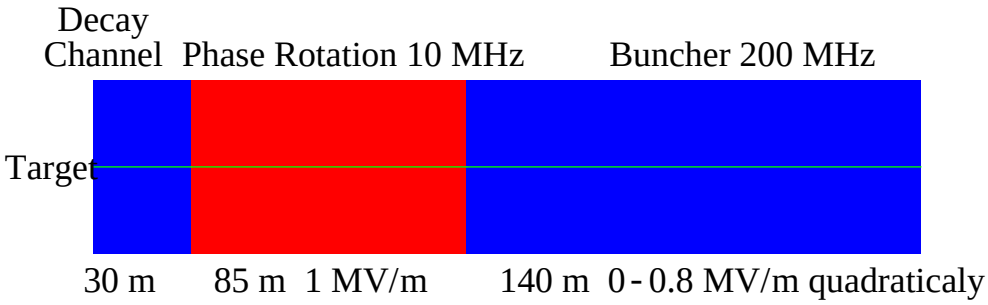


Figure 7.30: Layout of the muon front end with the buncher.

# Chapter 8

# Cooling

Cooling is a process in which beam emittance is reduced. From previous discussions, it appears that the muon beam demands a large apperture machine and that the beam dynamics is affected by large emittances. Cooling the muons in the front-end would relax technical requiremenys and make machine more economical. The neutrino factory could be considered as the first stage towards muon collider and, for such machines cooling is essential. We present parameterization of the ionization cooling process as a handy tool in cooler lattice design. Then we study cooling in a ring.

## 8.1 Theory of ionization cooling

All known and already well tested and widely used cooling methods are too slow for muon beams. Ionization cooling was proposed [51] as a baseline technique for muon beams. The simple principle is shown in Fig. 8.1. The muon passes through an absorber, where it loses energy by the ionization resulting from interactions with absorber electrons. Its total momentum vector is reduced ( phase 1 in Fig. 8.1). Accelerating the beam along the axis of the beam (phase 3) reduces the beam divergence and thus the transverse emittance. There is however a multiple scattering of muons on the absorber nuclei, which changes the initial direction of the muon (phase 2). This effect is statistical in nature and after avaraging over the muon ansamble creates the heating.

We shall derive an approximate equation of evolution of the transverse emittance in the cooler, which can be either a linac or a ring. We consider


Figure 8.1: Fundamental principle of the ionization cooling: reduction of the transverse momentum after passage through absorber and RF cavity.

the equation of emittance in a ring or in a linac:

$$\epsilon = \gamma_x x^2 + 2\alpha_x x x' + \beta_x x'^2 \tag{8.1}$$

Let us make a variation according to infinitesimal change of angle, assuming that transverse momentum is small comparing with its longitudinal component. This corresponds to the successive passage of a muon through an absorber, where it loses its momentum and an RF cavity, where its longitudinal component is restored. The net effect is a change in angle. Change in angle can be approximately given by:

$$\delta x' = -x' \frac{\delta p}{p} \approx -x' \frac{\delta W}{c\beta p} \tag{8.2}$$

Now we vary the equation for emittance and substitute the last formula. Before giving the formula we observe that averaging over the betatron phase gives:

$$< x'^2 >= \frac{\epsilon}{2\beta_x} \tag{8.3}$$

Finally after varying 8.1, substituting 8.2, using 8.3 during averaging over betatron phase and assuming $\alpha_x = 0$ at the position of the absorber, we obtain:

$$\delta\epsilon = -\epsilon \frac{\delta W}{c\beta p} \tag{8.4}$$

Now we describe a small variation with respect to passage through a small fraction of the cooler lattice. We can introduce the derivative with respect to s:

$$\frac{d\epsilon}{ds} = -\epsilon \frac{\frac{dW}{ds}}{c\beta p} P^A \tag{8.5}$$

where $\frac{dW}{ds}$ is calculated from the Bethe-Bloch formula at $W_s$ and $P^A$ is absorber packing factor. Assuming N absorbers of length $d$ in a lattice of length $L$, RF gradient $E$ and reference phase $\phi$, $P^A$ is given by expression:

$$P^A = \frac{Nd}{L} = \frac{P^{RF} eEsin\phi}{\frac{dW}{ds}} \tag{8.6}$$

where $P^{RF}$ is an RF packing factor. We calculated a cooling term in the emittance evolution equation.

Now we come to evaluation of the heating effect due to multiple scattering effect of muons on absorber nuclei. The rms angle spread (see [52]) after a passage of material characterized by radiation length $X_0$ is:

$$\theta_0 = \frac{13.6}{\beta cp}\sqrt{\frac{d}{X_0}}(1 + 0.038ln\frac{d}{X_0}) \approx \frac{13.6}{\beta cp}\sqrt{\frac{d}{X_0}} \tag{8.7}$$

where $p$ is the muon momentum in Mev/c. $X_0$ and $dW/ds$ depend on the choice of an absorber material. Usually a material with large energy loss and radiation length is needed. Liquid hydrogen is a possible choice, but requires a special container and has in addition important safety issues. Lithium hydride is an interesting alternative due to easy manipulations with solid materials. Note the difference between the betatron function always denoted $\beta_x$ and the relativistic $\beta$ factor. We observe that:

$$\delta\epsilon = \beta_x(\delta x')^2 \tag{8.8}$$

Finally we obtain the following expression for the heating term:

$$\frac{d\epsilon}{ds} = \beta_x \frac{13.6^2 P^A}{(c\beta p)^2 X_0} \tag{8.9}$$

The equation for the emittance evolution along the cooler lattice has the following form:

$$\frac{d\epsilon}{ds} = -\epsilon \frac{\frac{dW}{ds}}{c\beta p} P^A + \beta_x \frac{13.6^2 P^A}{(c\beta p)^2 X_0} \tag{8.10}$$

The analytical solution for this equation can be expressed as follows:

$$\epsilon(s) = \epsilon_e + (\epsilon_0 - \epsilon_e)e^{-\frac{s}{L_c}} \tag{8.11}$$

where $\epsilon_e$ and $L_c$ correspond to the equilibrium emittance and the cooling length, respectively. The equilibrium emittance is the ultimate state of the cooling process and depends on absorber material and lattice properties as follows:

$$\epsilon_e = \beta_x \frac{13.6^2}{\beta pc X_0 \frac{dW}{ds}} \tag{8.12}$$

The cooling length can be understood as the length of the cooler needed to cool the muon beam down by a factor $1/e$. It is a function of the averaged RF gradient in the cooler. It can be related to cooling time in the following way:

$$T_c = \frac{L_c}{\beta c} = \frac{p}{P^{RF} eE sin\phi} \tag{8.13}$$

The presence of dispersion in the cooler creates the correlation between energy and position which can be used for longitudinal cooling. Putting wedge absorbers in the high dispersion region, a position-dependent energy loss is introduced. Particles with higher energy pass at a distance $D\frac{\delta p}{p}$ from the reference orbit and stay longer in the wedge absorber, which translates into a larger energy loss. The effect of the dispersion at the wedge absorber introduces an additional heating term in the transverse plane:

$$\epsilon D \frac{\frac{dW}{dx}}{pc} P^W \tag{8.14}$$

$$P^W = \frac{N\delta'}{L} \tag{8.15}$$

where we put N wedge absorbers with angle $\delta'$ in the cooler of a length $L$. In particular this term increases the equilibrium emittance achievable in the cooler.

## 8.2 Motivation for cooling rings

The muon cooling channels proposed for a neutrino factory are solenoidal focused linacs [17, 19]. The simple cell structure together with a lack of

bending magnets and zero dispersion results in low equilibrium emittance. The large number of RF cavities needed to achieve a sufficient cooling rate on the entire lattice length makes the cooler price a substantial part of the neutrino factory cost. To see the required length for cooling we study the evolution of emittance assuming a $\beta_x$ value of 0.5 m at the absorber and 44 MHz 2 MV/m at $\pi/4$ phase. The 2 cm emittance muon beam at 200 MeV kinetic energy is required to be cooled. The evolution of the emittance along a cooler is shown in Fig. 8.2.

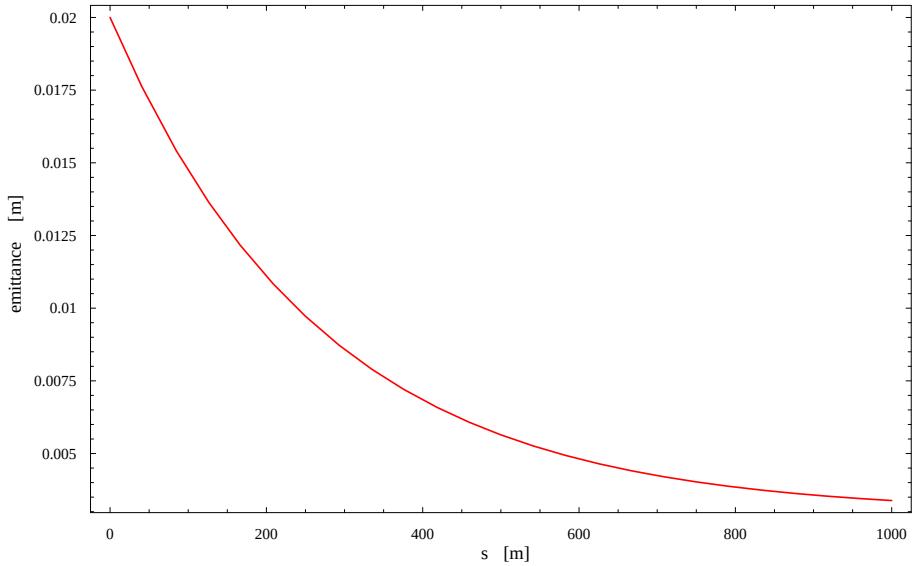


Figure 8.2: Transverse emittance along the cooler lattice

It can be seen, that a 500 m lattice is needed to cool the beam by a factor 4 (the beam size is reduced by a factor 2).

A ring cooler is proposed [53] in order to reduce the cost of muon cooling for the neutrino factory. The beam can be injected into a ring with a high RF packing factor and perform a few turns until the emittance is reduced. The ring circumference is a compromise between cost, performance of the upstream part of the muon front-end in order to create a short high intensity muon train and the injection kicker rise/fall time. The presence of a small ring with standard full aperture injection puts a severe constraint on the neutrino factory machine. The high-power proton beam has to be efficiently converted into a short muon trains or single bunches separated by the cooling time. Note that the CERN scheme in which 140 bunches are extracted at 44

MHz from the proton accumulator ring to the target cannot produce the short enough muon train. As an alternative, a very intense single bunch can be formed at the target and bunched at the cooling frequency or short trains of bunches could be formed by extracting proton beam in steps. In addition the horn current flat top and the mercury jet at the target must last long enough to accept the beam consisting of several muon trains or single bunches within the machine cycle (assuming the use of the mercury jet target). In this way we have introduced an additional intermediate time structure. Now we have the machine cycle set at 50 Hz called macro-structure. This macro-structure consists of short trains or single bunches with length consistent with the muon cooling ring injection separated by the cooling-down time and kicker time. At the most basic structure we have a time micro-structure compatible with the RF system. Here we stop discussion on the constraints imposed on the proton beam and target, and leave space for a future study. As a balance between kicker rise/fall time and the total low cost of the cooler we assume a circumference of 50-100 m. According to Fig. 8.2 the muon beam performs 5-10 revolutions to achieve the cooling by a factor 4.

## 8.3 Zero gradient ring

Effective cooling requires a small $\beta_t$ value at the absorber position. In addition a large RF packing factor determines the beam radius to correspon to RF cavity size. The large momentum spread and associated chromatic aberrations practically exclude the possibility of using standard low-beta insertions matched to high $\beta_t$ values. Beam matched to a small beta at reference energy deviates from matching conditions for particles with momentum deviations, which can create a lower cooling rate duo to higher $\beta_t$ value or even beam instability. This suggests that a lattice with low $\beta_t$ values everywhere must be chosen. The single cell should have in addition large momentum acceptance. With a lattice based on the alternating gradient principle in the FODO structure solutions with very short drift lengths and short but extremely strong magnetic elements are usually found. In particular, it is difficult to go below 1 m $\beta_t$ value for the FODO based cell structure in both transverse planes at the same point. This difficulty can be overcome in the AG triplet structure, where there can be similar beta values in both planes at the end of the cell and there is a long drift length. Unfortunately the beta value is high in one transverse plane and large apertures are needed. All these limitations lead us

to search for other convenient solutions with focusing present in all elements and distributed more uniformly in a cell length.

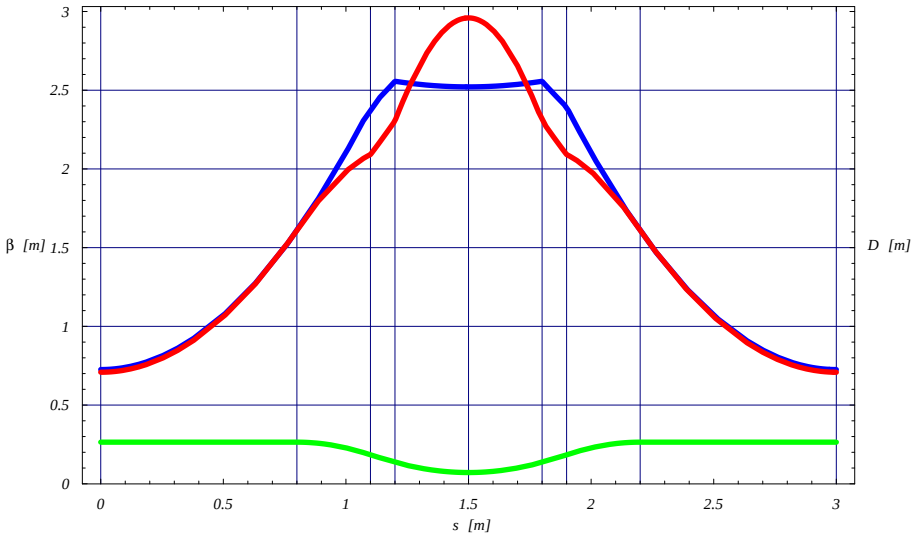


Figure 8.3: Optics in the cell of the weak focusing ring. The red, blue and green lines are $\beta_x$, $\beta_y$ and $D$ functions, respectively.

We propose a solution with zero-gradient dipole magnets for focusing. The triplet-like structure enables us to achieve similar beta values in the drift sections at the end of the cell. The horizontal focusing is achieved via $1/\rho^2$ term in bending magnets. Negative bending was introduced to achieve small horizontal $\beta_x$. The proper shape of the magnet edges creates an effect of focusing in the vertical plane. All edge focusing effects act as thin focusing lenses in the vertical plane. The edge defocusing effect in the horizontal plane is much weaker than the focusing due to bending. The optics in the single cell is shown in Fig. 8.3 and a cell drawing is shown in Fig. 8.4. The cooler ring consists of 32 cells and is 96 m in circumference. The $\gamma_T$ is imaginary. The parameters of the ring are given in Table 8.1. On both cell ends there is enough room for the 87.91 MHz cavity. A 43.955 MHz cavity can be used as well but it would correspond only to one cavity per cell in average and smaller RF packing factor. We study the evolution of the particle distribution shown in Fig. 8.9. We consider the case of normal absorbers and wedge absorbers with a wedge angle, both with liquid hydrogen. The evolution of the transverse rms emittances are shown in Fig. 8.5 and Fig. 8.6 for the

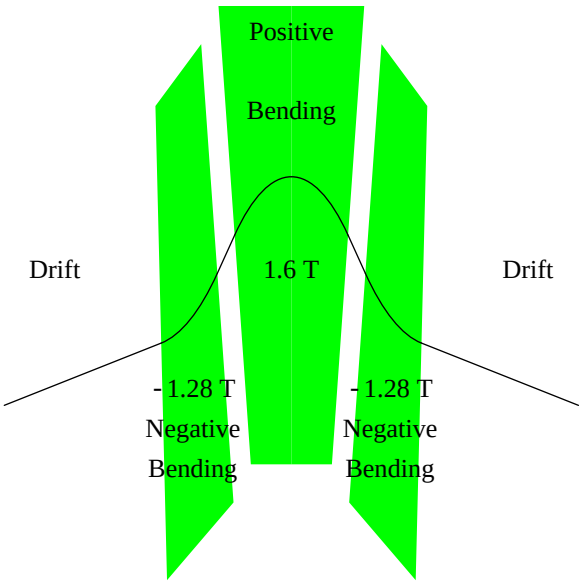


Figure 8.4: Layout of the "Zero-gradient" ring cell.

horizontal and the vertical planes respectively as a function of the number of turns in the cooling ring (Figs 8.12 and 8.13 for the study with wedge absorbres). The longitudinal plane and transverse brightness are shown in Fig. 8.7 and Fig. 8.8 (Figs 8.14 and 8.15 for the study with wedge absorbres), respectively. We define the brightness of the beam as a particle density in 4D transverse phase space:

$$B_{4D} = \frac{N}{4\pi^2 \epsilon_x^{rms} \epsilon_y^{rms}} \tag{8.16}$$

where N is number of particles in the simulation and takes into account both losses due to aperture restrictions and muon decay. The initial and final transverse phase space portraits are shown in Fig. 8.9 (8.16). The initial and final longitudinal phase space are shown in Figs 8.10 and 8.11 (Figs. 8.17 and 8.18 for the study with wedge absorbres). The simulation confirms the ability to cool in both transverse phase spaces. The presence of wedge absorbers at the dispersion regions increase the achievable horizontal emittance. The longitudinal emittance has a small tendency to grow even if we do not take the energy straggling into account, but we can cure the effect to some extent by using wedge absorbers. Unfortunately the vertical

| | |
|---|---|
| Length of negative field magnet length | 0.3 m |
| Entrance edge angle of negative field magnet | 0 rad |
| Exit edge angle of negative field magnet | 0.223838 rad |
| Deflection of negative field magnet | -0.402517 rad |
| Length of positive field magnet | 0.6 m |
| Entrance edge angle of positive field magnet | 0.223838 rad |
| Exit edge angle of positive field magnet | 0.223838 rad |
| Deflection of positive field magnet | 1.00138 rad |
| Long drif length | 1.6 m |
| Number of cells | 32 |
| Circumference | 96 m |
| Reference muon kinetic energy | 200 MeV |
| Momentum acceptance | $\pm$15% |
| Harmonic number | 30 |
| $Q_x$, $Q_y$ | 11.83, 11.68 |
| Wedge absorber angle | 0.3 rad |
| $\gamma_T$ | -5.54i |
| Mean RF gradient | 3.33 MV/m |
| Total transverse acceptance | 2 cm |
| Muon transmission including decay | 70.3% |

Table 8.1: Parameters of the "Zero-gradient" cooling ring.

acceptance of the "zero-gradient" ring was not confirmed by the nonlinear tracking studies. Nevertheless the study was an interesting introduction to problems of muon cooling rings.

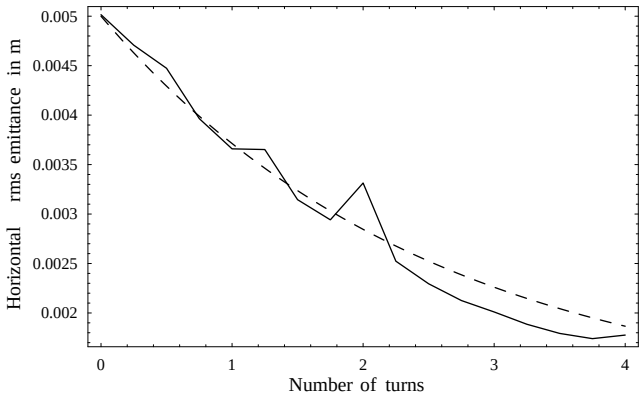


Figure 8.5: Evolution of horizontal rms emittance in the dipole ring. Dashed line represents the theoretical prediction.

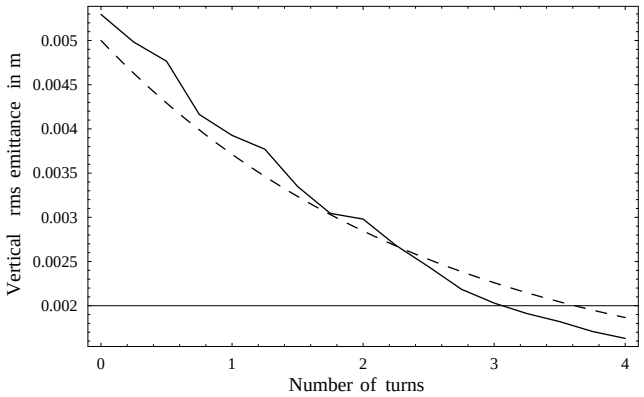


Figure 8.6: Evolution of vertical rms emittance in the dipole ring. Dashed line represents the theoretical prediction.

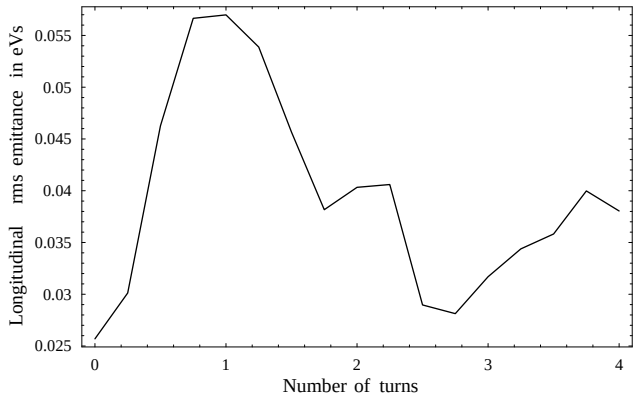


Figure 8.7: Evolution of longitudinal rms emittance in the dipole ring.

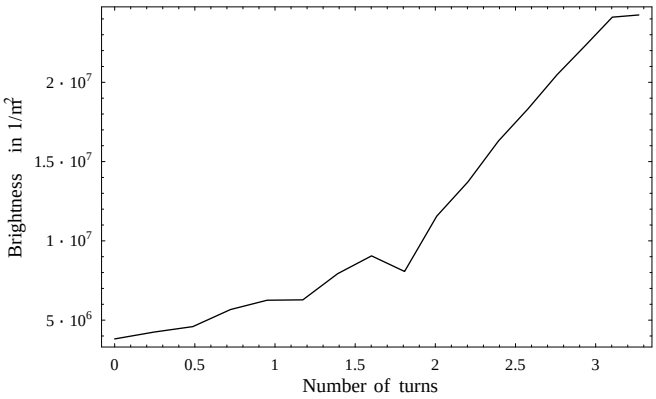


Figure 8.8: Evolution of transverse brightness in the dipole ring.

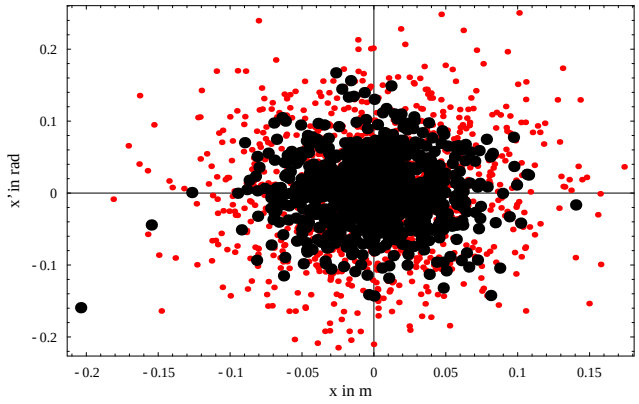


Figure 8.9: Initial (small, red dots ) versus final (large, black dots) horizontal phase space distribution.

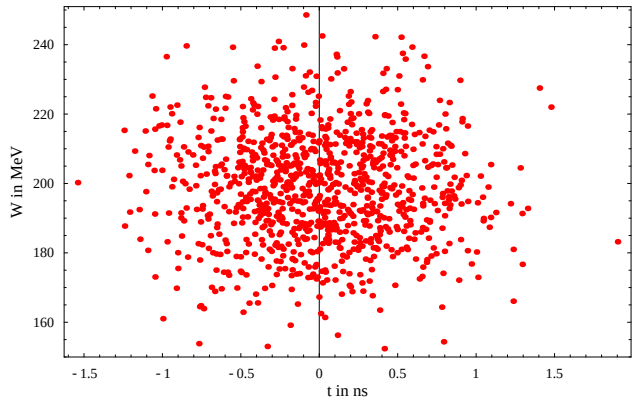


Figure 8.10: Initial longitudinal phase space.

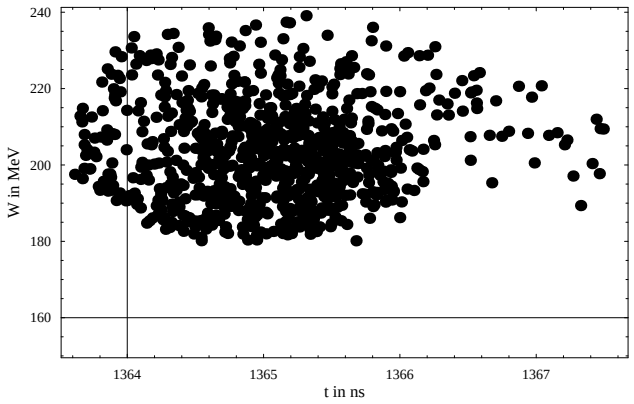


Figure 8.11: Final longitudinal phase space.

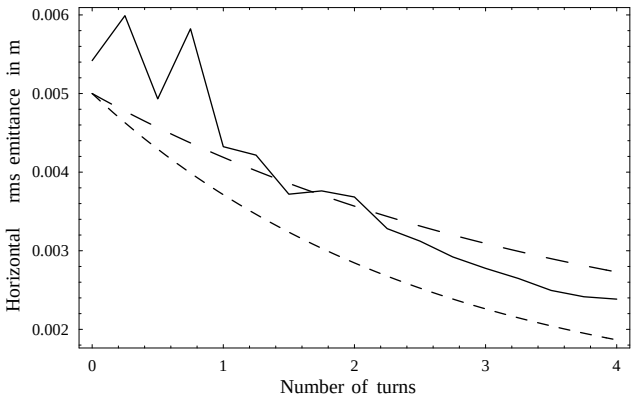


Figure 8.12: Evolution of horizontal rms emittance in the dipole ring with wedge absorbers. The theoretical predictions with and without wedge absorbers are ploted with large and small dashings, respectively.

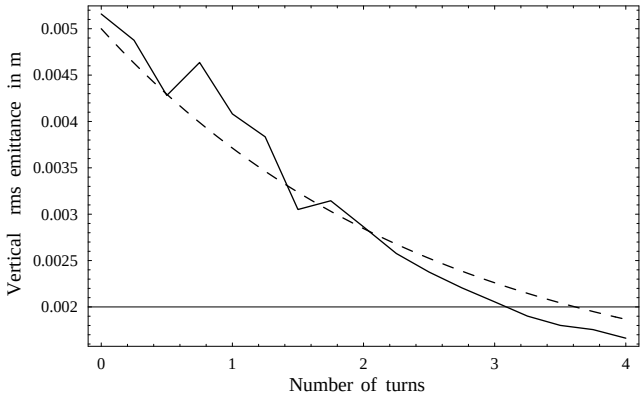


Figure 8.13: Evolution of vertical rms emittance in the dipole ring with wedge absorbers. Dashed line represents the theoretical prediction.

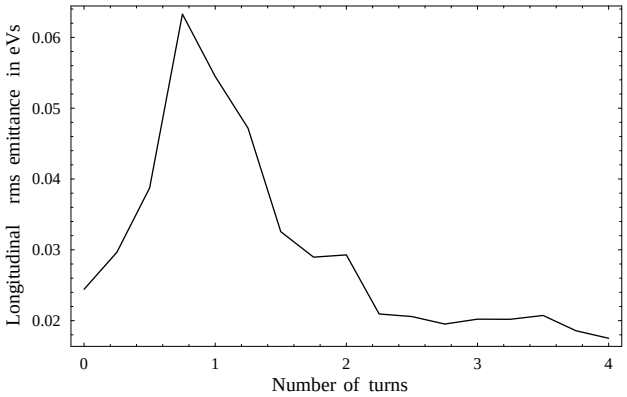


Figure 8.14: Evolution of longitudinal rms emittance in the dipole ring with wedge absorbers.

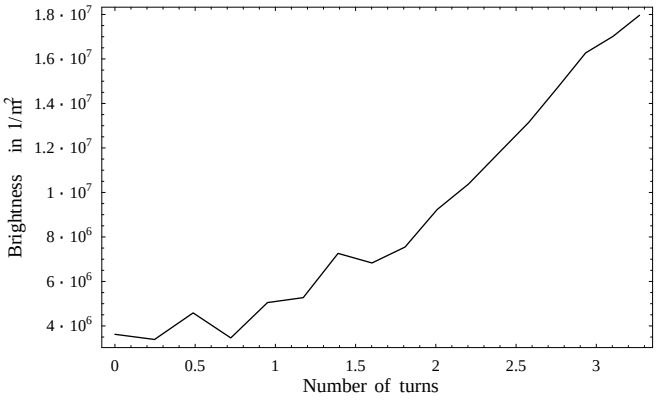


Figure 8.15: Evolution of transverse brightness in the dipole ring with wedge absorbers.

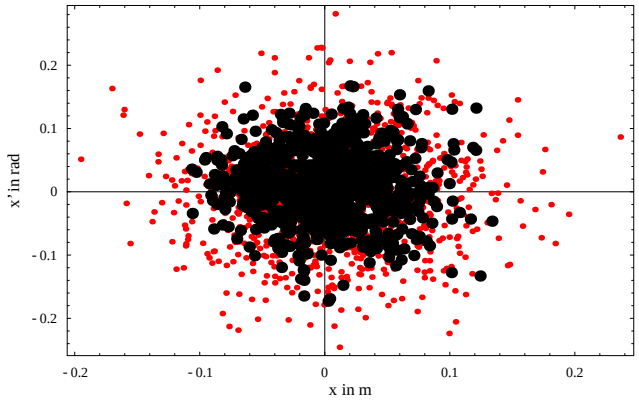


Figure 8.16: Initial (small, red dots ) versus final (large, black dots) horizontal phase space distribution with wedge absorbers.

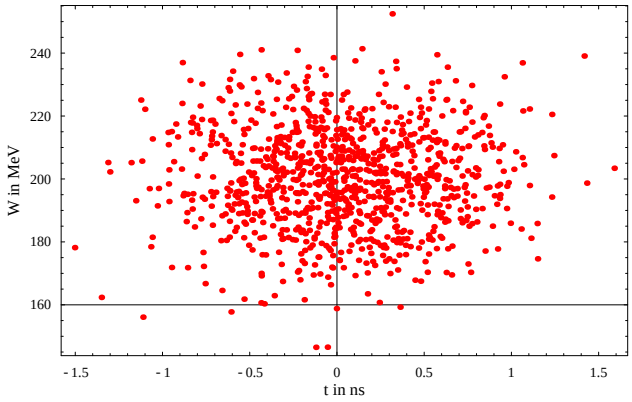


Figure 8.17: Initial longitudinal phase space.

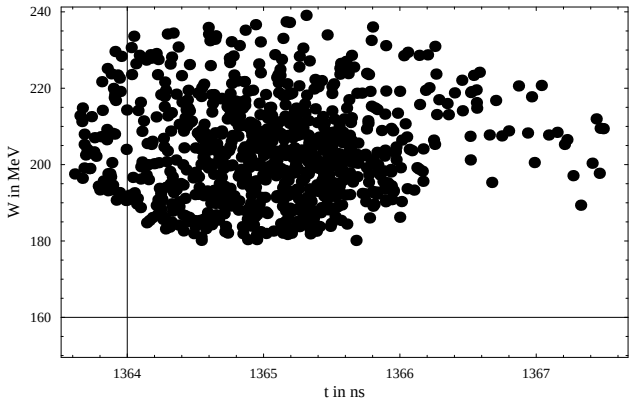


Figure 8.18: Final longitudinal phase space with wedge absorbers.

## 8.4 Solenoidal focused ring with adiabatic matching

The need for fast and efficient cooling dictates a low $\beta_t$ value and a high average RF gradient. Both conditions can be met with solenoidal focusing. The disadvantages of the solenoidal focusing are a very large chromatic detuning and difficulties with the injection/extraction scheme. The cell for cooling with superimposed RF cavities and focusing solenoidal coils is so compact that there is almost no room for injection/extraction. To inject or extract a long drift section is needed. For the standard cooling cell, drift length of about 1 m imposes a very severe conditions on the kicker strength. We have to note here, that for AG rings and the zero gradient ring the injection can be easier due to the possibility of using open C-shaped magnets together with distributed kicker modules in the ring. For solenoidal focusing the distribution of kickers seems to be not at hand due to a strong chromatic detuning. In the thin lens approximation the symmetric $\beta_t$ in the FOF (solenoid, drift, solenoid) cell depends on cell length. A kicker located at the beginning of the cell has to kick the beam away by more than $2\sqrt{\epsilon\beta}$ assuming zero dispersion in the cell. We end up with the following condition for the kick:

$$\psi > 2\sqrt{\frac{\epsilon}{L/sin\mu_L}} \tag{8.17}$$

where $\mu_L$ is the Larmor phase advance per cell. This condition can be converted into the formula for the ring acceptance as a function of the kicker strength:

$$\epsilon_{max} = \frac{\psi^2 L/sin\mu_L}{4} \tag{8.18}$$

This suggests that locally a cell with a long length is needed. Then we meet the problem of how to match a large $\beta_t$ at injection/extraction section into a cooling cell of the solenoidal lattice with very strong chromatic effects. We propose adiabatic matching by slow variation of the intermediate cell parameters. The phase advance per cell is kept small in order to achieve large momentum acceptance. The bending fields in the cells are varied in order to control value of the dispersion function. In this study we use the sector bendings, but the tilted solenoidal coils could be used to generate the bending field (see [53]). Firstly, we study the optics in the Larmor frame

approximation neglecting the effect of bending magnets. Then we repeat the calculations using eigenvalues of the $4 \times 4$ ring transfer matrix, taking bendings into account. A spectrum of eigenvalues as a function of particle momentum was studied. In general unstable regions are found in the momentum band. We performed a minimization varying the solenoidal strengths in the adiabatic matching section in order to achieve a better solution. By a better solution we understand a spectrum of absolute values of the ring transfer matrix eigenvalues very close to one. The solution found has an off-momentum stability for a broad momentum band. The remaining narrow islands of instability should not cause serious beam loss due to strong momentum exchange in the cooler ring in RF cavities and absorbers. In addition instabilities in the FOFO channel develop slower than in the AG lattice because of the permanent focusing and even transformation from the hard edge approximation into a smooth field maps model should reduce the effect of instability. This effect can be explained by magnetic confinement of the solenoidal field which is extended into the larger part of the ring due to the smooth character of the realistic fields which fill partially even the drift sections.

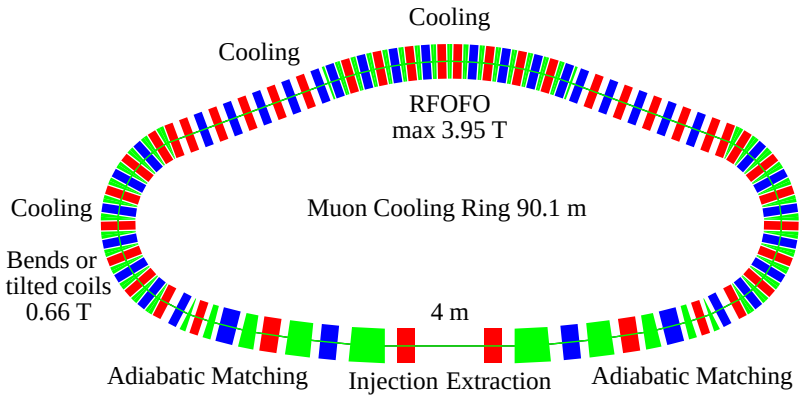


Figure 8.19: The layout of the solenoidal ring. The red and blue parallelograms represent solenoids with positive and negative field polarity, respectively. The green polygons correspond to the sector bendings.

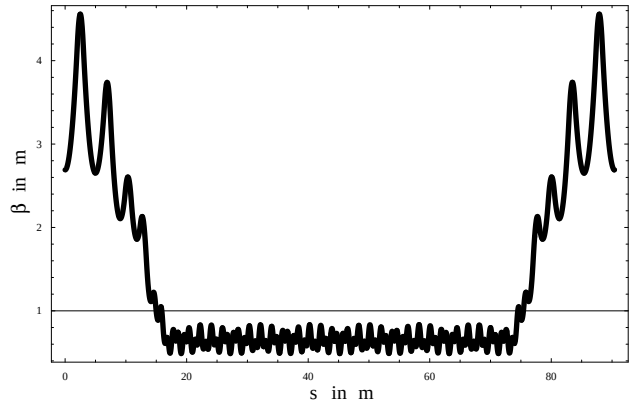


Figure 8.20: The Larmor $\beta_L$ function in the solenoidal ring.

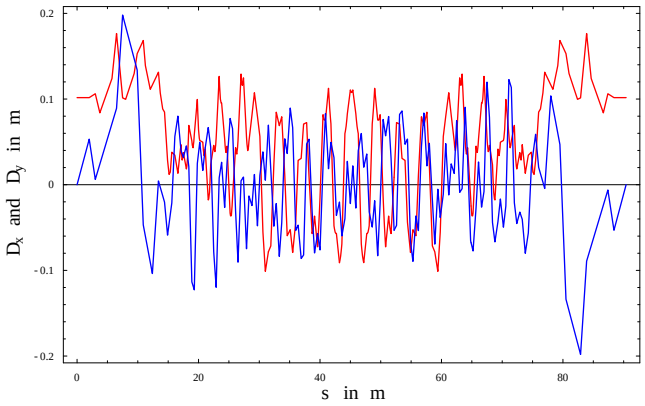


Figure 8.21: Dispersions in the solenoidal ring.

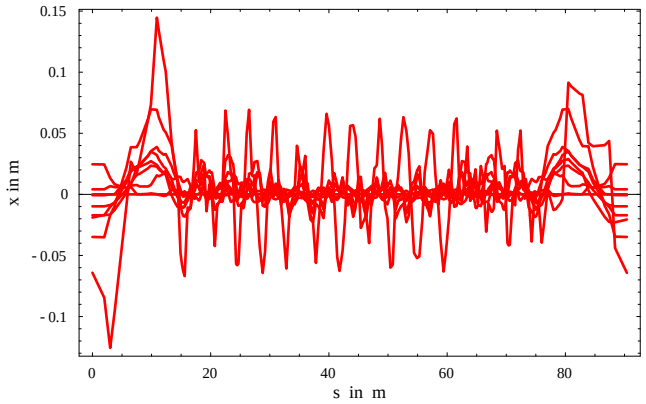


Figure 8.22: Off-momentum closed orbits with positive momentum deviation seen in the horizontal plane.

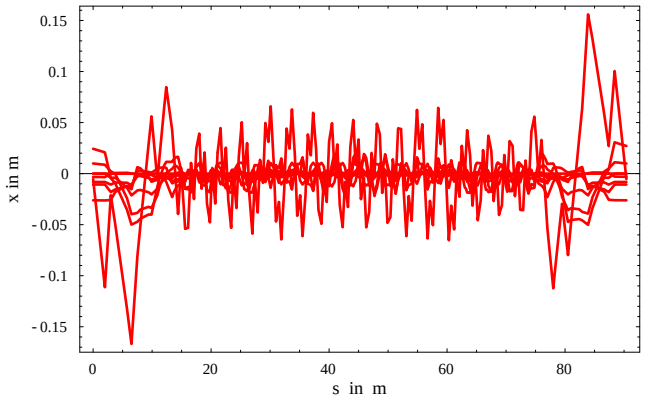


Figure 8.23: Off-momentum closed orbits with negative momentum deviation seen in the horizontal plane.

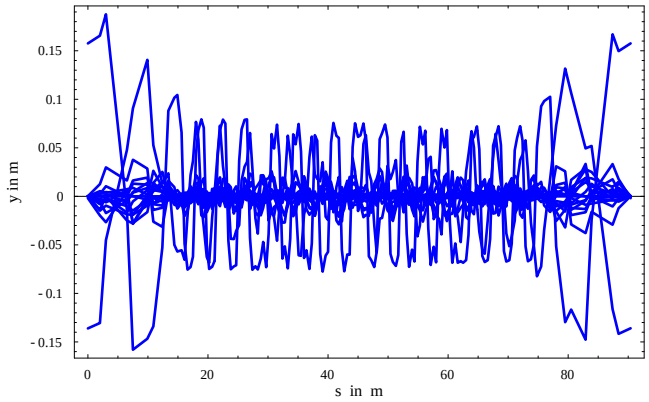


Figure 8.24: Off-momentum closed orbits seen in the vetical plane.

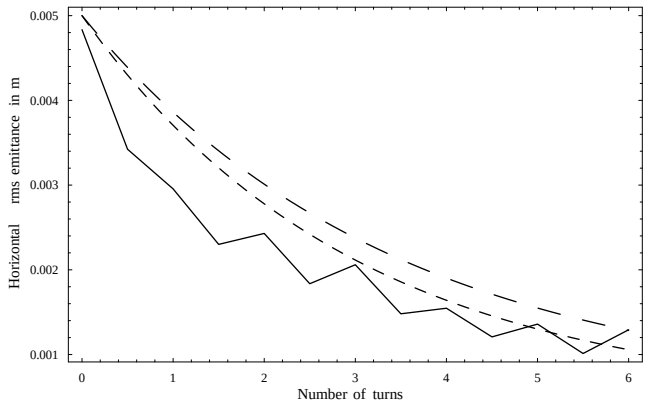


Figure 8.25: Evolution of horizontal rms emittance in the RFOFO ring. The theoretical predictions with and without wedge absorbers are ploted with large and small dashings, respectively.

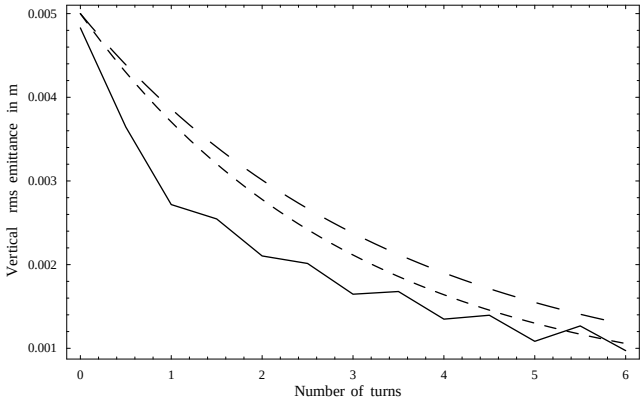


Figure 8.26: Evolution of vertical rms emittance in the RFOFO ring. The theoretical predictions with and without wedge absorbers are ploted with large and small dashings, respectively.

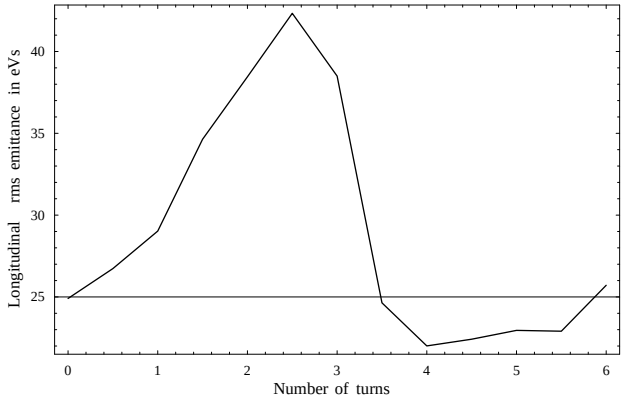


Figure 8.27: Evolution of longitudinal rms emittance in the RFOFO ring.

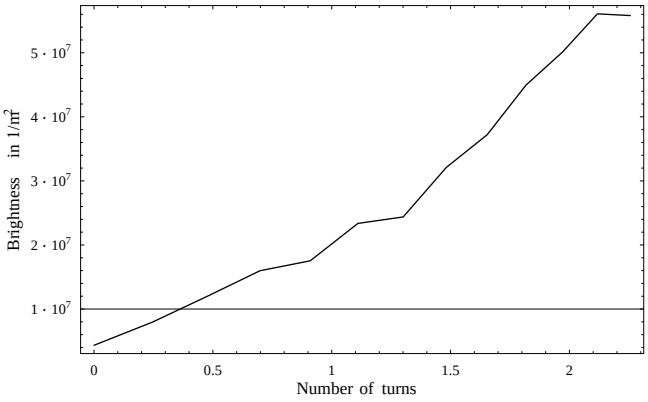


Figure 8.28: Evolution of transverse brightness in the RFOFO ring.

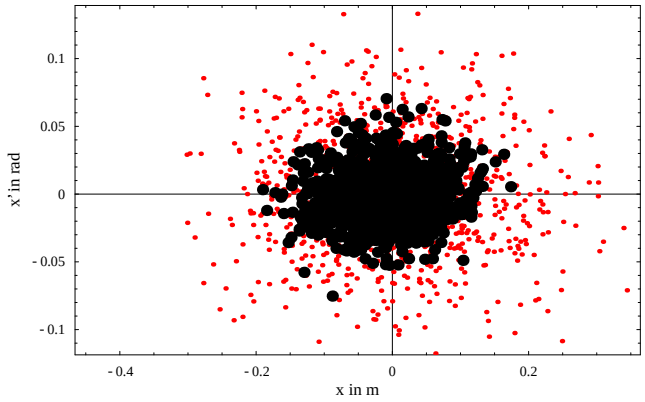


Figure 8.29: Initial (small, red dots ) versus final (large, black dots) horizontal phase space distribution.

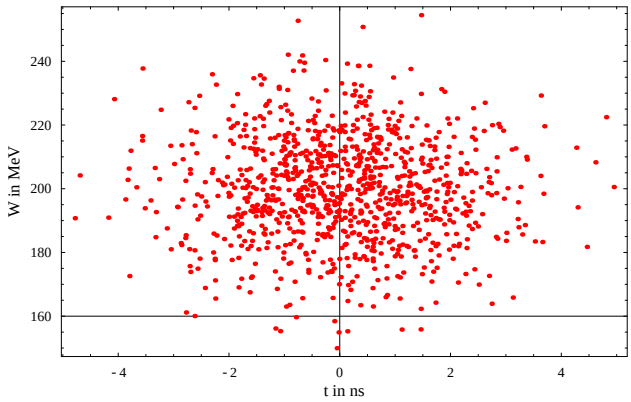


Figure 8.30: Initial longitudinal phase space.

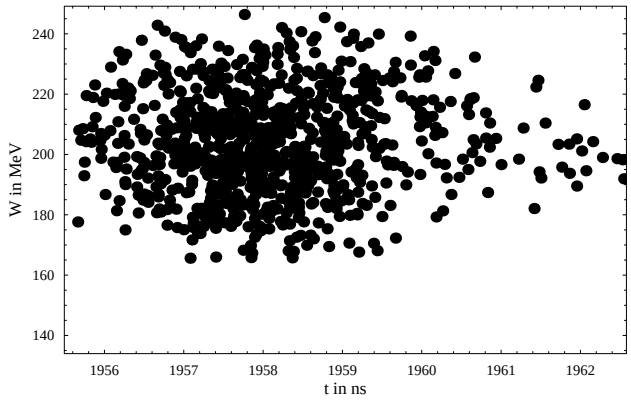


Figure 8.31: Final longitudinal phase space.

Table 8.2 shows the parameters of the cooler ring. The schematic layout of the ring is shown in Fig. 8.19. Fig. 8.20 shows the on-momentum Larmor $\beta_L$ function. The off-momentum closed orbits are shown in Fig 8.22, Fig 8.23 and Fig 8.24. We put RF cavities in the low-beta region. The RF packing factor for the ring is 0.75. We simulate cooling in the ring with liquid hydrogen absorbers and 43.57 MHz RF (h=14) at $\pi/4$ phase. The gamma transition factor equals 2.09. The beam passes 6 turns with a mean energy of 200 MeV. We show the initial and final distributions of particles in the horizontal phase space in Fig. 8.29. The evolution of the rms emittances along the cooler are shown in Fig. 8.25, Fig. 8.26 and Fig. 8.27. The closed orbits shown above have a strong correlation between the energy and the horizontal position in only two places around the ring in the adiabatic matching section. These locations, corresponding to 10 m and 80 m from the injection point are the only places where wedge absorbers can be installed. The beta function at these positions is relatively high, but we include wedge absorbers to minimize blow up of the longitudinal plane. The number of wedge absorbers required to achieve the longitudinal cooling is too low. The evolution of transverse brightness is shown in Fig 8.28. The ring cools down transverse emittances by factor 4 per plane. The goal of the adiabatic matching section is to achieve a drift for the injection/extraction and matching into the low beta section in the ring for a broad momentum range. The induction kicker was proposed to be developed for the injection/extraction in the cooler rings [54]. The magnetic field at flat top can be as much as 0.42 T. With the application of adiabatic matching this value can be reduced by at least a factor 2, but stored energy is the same assuming kicker of the same length according to increase of beam size due to large $\beta$ value. Obviously longer straight section (4 m) enables to put longer kicker, than 1m studied in [54] or to put more kicker modules. The details of the injection/extraction remain to be studied, but the required kick might be achievable by conventional strong kickers. With adiabatic matching we have not only reduced the kick strength but have room for more than one kicker modulus in the 4 m long drift section. The lack of longitudinal cooling is a serious drawback of the above design. It can be achieved by increasing the amount of correlation between the position and momentum deviation. This can be achieved in the design with positive dispersion along the ring circumference.

| | |
|---|---|
| Long drif length | 4 m |
| Circumference | 90.1 m |
| Reference muon kinetic energy | 200 MeV |
| Momentum acceptance | $\pm 15\%$ |
| Harmonic number | 14 |
| Wedge absorber angle | 0.7 rad |
| $\gamma_T$ | 2.09 |
| Mean RF gradient | 1.5 MV/m |
| Total transverse acceptance | 2 cm |
| Muon transmission including decay | 69.3% |

Table 8.2: Parameters of the RFOFO ring.

# Chapter 9

# Comparison of scenarios

We discuss muon losses due to decay in the front end and preacceleration. We compare efficiency of scenarios parameterized by the RF frequency and the accelerating phase during cooling and preacceleration. It has to be stressed that the comparisons does not take into account scenarios with bunching. Finaly, we present the design of muon front end based on bunch-to-bucket principle.

## 9.1 Decay losses in the muon front end and preacceleration

The decay losses in the front end depend on the length of the lattice assuming beam transfer at constant energy. The length of phase rotation section and a cooler (or number of turns in the ring cooler) depends on the RF gradient. As assumed previously, the RF gradient is a function of frequency. It follows that, the decay losses depend on RF frequency used in the front end. It is interesting to study the performance as a function of RF frequency. We want to address also a choice of RF phase in the cooler. The need of fast cooling would suggest choosing phase near a crest at maximal acceleration, which enables the largest amount of absorber material to be inserted into a cooler. The high RF frequency offers also a large necessery gradient. This requirement has to be balanced with the area of stable longitudinal phase space, which is zero at crest and has a maximal size at zero acceleration, which does not allow for cooling. At small phase the amount of acceleration enables cooling but a long cooling time would result in too low muon

survival. Also low frequency with its longer bucket enables to accept larger longitudinal acceptance. There should exist an optimum in RF frequency and phase for which the muon current at the end of cooling would be maximal. The decrease of the muon intensity at the exit of a cooling line can be approximated by a simple exponential decay law:

$$N = N_0 e^{-\frac{2T_c}{\gamma\tau_\mu}} \tag{9.1}$$

where $T_c$ is the muon cooling time, $\gamma$ is the relativistic gamma corresponding to mean muon beam energy, and $\tau_\mu$ is the muon lifetime at rest equal to 2.197 $\mu$s. In the above formula we have assumed a cooling factor of $e^2$, which takes two cooling times. If we assume uniform distribution of particles in the longitudinal plane and a bunch perfectly matched into a bucket we can estimate a dependence of the muon intensity as a function of the RF phase:

$$N_c(\phi_s) = AB_a(\phi_s)e^{-\frac{2T_c(\phi_s)}{\gamma\tau_\mu}} \tag{9.2}$$

where $B_a(\phi_s)$ is the bucket area as a function of synchronous phase and A is a normalization constant. The relative muon intensity after cooling for the uniform distribution of particles in the longitudinal plane is plotted in Fig. 9.1 (the values are normalized to 44 MHz stationary bucket at zero phase). We observe a strong dependence on RF phase near a zero phase and a relatively slower fall down to zero again near the crest.

The losses in the phase rotation can be calculated in a similar way:

$$N = N_0 e^{-\frac{L_{PR}}{L_\mu\gamma}} \tag{9.3}$$

where the $L_\mu = c\beta\tau_\mu 660$ m and $L_{PR}$ corresponds to the length of the phase rotation section.

The efficiency of capture and cooling has to be accompanied with efficient acceleration. Because the final scheme of acceleration is still under development, in our study we take into account decay losses in the preacceleration stage from 0.2 GeV to 2 GeV kinetic energy assuming that acceleration is done at the same frequency and phase as cooling. This simplification assumes no longitudinal cooling and corresponds to preacceleration in the ring rather than in the linac, where the phase can be adjusted more freely. The efficiency of preacceleration can be calculated in the following way:

$$N = N_0 \left(\frac{W_0 + m_\mu}{W_{final} + m_\mu}\right)^{-\frac{1}{L_\mu\gamma'}} \tag{9.4}$$

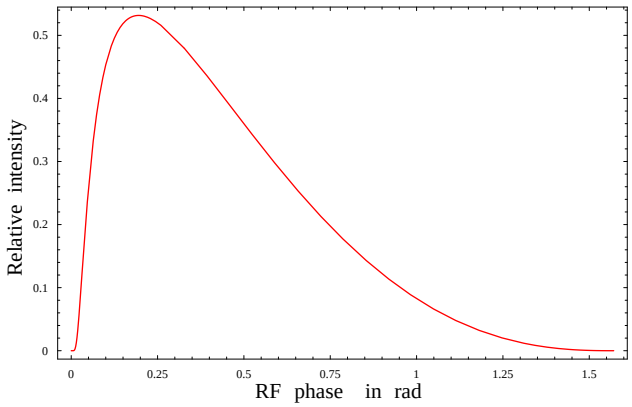


Figure 9.1: Relative muon intensity after cooling in the 44 Mhz cooling section as a function of RF phase. The uniform longitudinal muon distribution has been assumed. The values are normalized to 44 MHz stationary bucket at zero phase. The zero phase corresponds to no acceleration.

where $W_0$ and $W_{final}$ correspond to the initial and final kinetic energies and $\gamma'$ is given by the following equation:

$$\gamma' = \frac{eE_0 sin(\phi)}{m_\mu c^2} \tag{9.5}$$

where $E_0 sin(\phi)$ is the effective accelerating gradient.

## 9.2 Comparing scenarios

The assumption of uniform particle distribution in the longitudinal phase space filling the entire bucket highly favours a low phase region. For the realistic muon bunch at the exit of the decay channel created by a 4 ns long proton beam, a relatively large bucket at low frequency and phase will be only partially filled. We meet again a problem of matching a bunch into a bucket. We run a series of simulations to calculate the amount of particles filling a bucket in various scenarios. We start with scenario with phase rotation, cooling and preacceleration performed at the same frequency. We assume that the RF gradient depends on frequency in the same way as in the study of the phase rotation in the chapter 7. First we apply phase rotation and count particles in the accelerating bucket created by the RF cavities with

the same frequency as thoes used for the phase rotation for various phases. We work with a fixed kinetic energy interval of muons at the exit of the 1.8 T solenoidal decay channel between 20 and 400 MeV, created from pion distribution simulated in the target and horn studies based on MARS code [39]. We normalize the number of accepted muons by total number of muons in this interval. To calculate the final efficiency the capture efficiency is multiplied by loss factors corresponding to muon passage through the phase rotation given by equation 9.3, to exponential muon decay in the cooler given by equation 9.1, and the preacceleration (9.5). In Fig. 9.2 we plot the relative number of muons at the end of preacceleration for various frequencies.

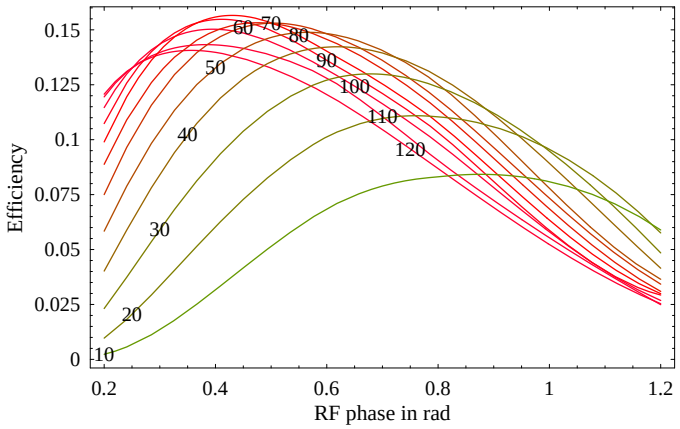


Figure 9.2: Efficiency in the front end with single RF frequency and cooling. Every line is described by frequency in MHz.

We repeat our calculations with a second harmonic phase rotation. It means that we phase-rotate with a harmonic two RF system with respect to cooling. Fig. 9.3 shows the efficiency of a system consisting of a second harmonic phase rotation, cooling and preacceleration

Then we calculate an efficiency in the scenario without phase rotation. We count particles in the bucket at the exit of the decay channel, where we start to cool directly. In this calculation we omit the loss factor corresponding to muon decay in the phase rotation. Fig. 9.4 shows the achieved efficiency.

The phase rotation impoves the final efficiency with comparison to the scenario without phase rotation, specially at low frequency. The improvements are larger for the second harmonic phase rotation scenario. The efficiencies in scenarios without cooling but with the standard phase rotation

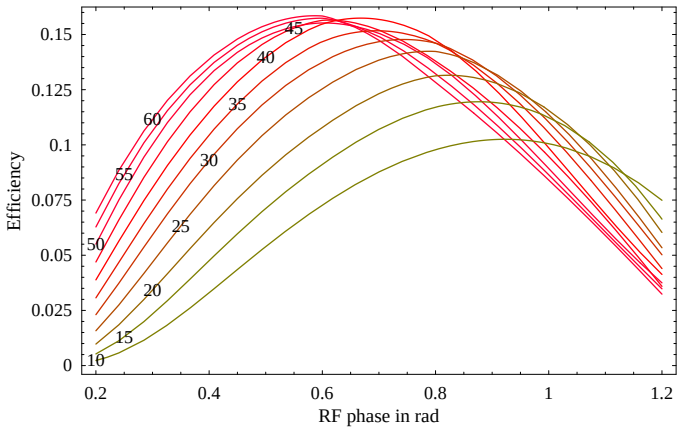


Figure 9.3: Efficiency in the front end with second harmonic phase rotation and cooling. Every line is described by frequency in MHz.

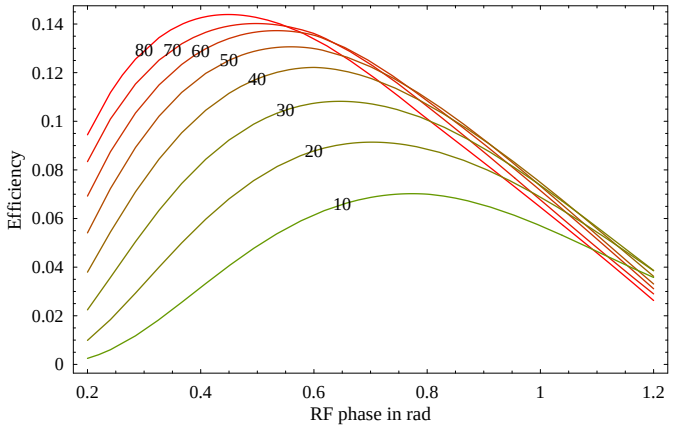


Figure 9.4: Scenario with cooling but without phase rotation. Every line is described by frequency in MHz.

and the second harmonic phase rotation are shown in Figs 9.5 and 9.6, respectively. Finaly in Fig. 9.7 we plot the efficiency in the scenario without phase rotation and cooling. Table 9.1 descibes the frequency of RF systems used in the scenarios confronted in this chapter. Loss factors corresponding to cooling are shown in Fig. 9.8. Higher losses can be clearly seen specially in the low frequency range, which can be understood by the long cooling time. Nevertheless the losses in all systems are still dominated by the acceleration part. It must be stressed that the efficiency factor takes into account

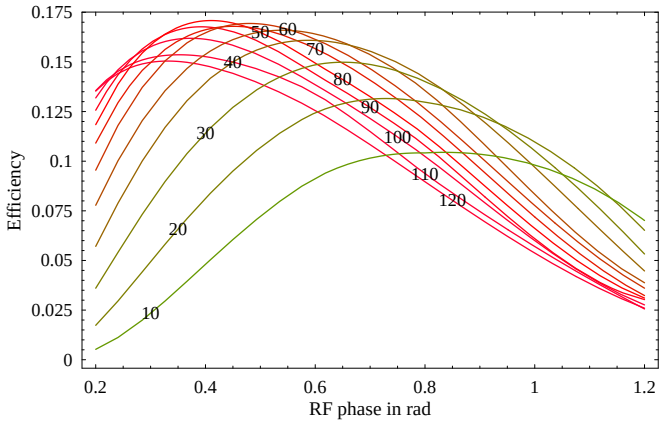


Figure 9.5: Scenario without cooling and with the standard phase rotation. Every line is described by frequency in MHz.

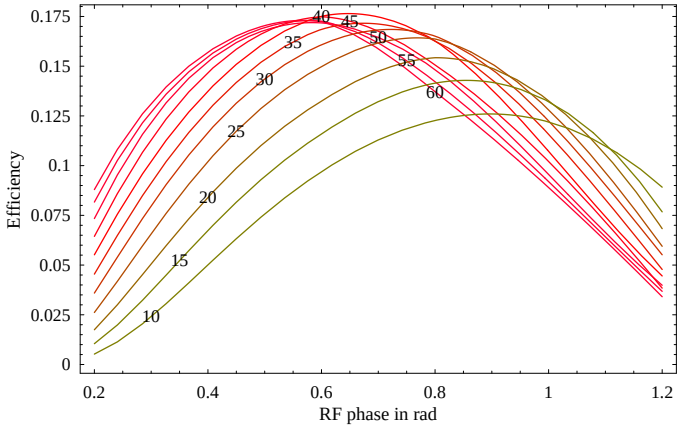


Figure 9.6: Scenario without cooling and with the second harmonic phase rotation. Every line is described by frequency in MHz

only the longitudinal phase plane, not taking into account transverse acceptances. It is clear that acceptance will be different for various frequencies due to limitations in the size of RF cavities. In particular for higher frequencies cooling may be necessary before acceleration. The choice of a higher frequency is beneficial due to higher transmission in the acceleration, cooling time is shorter and transverse damping offered by the ionization cooling enable larger transverse emittances to be accepted. The muon beam would have larger transverse 4D brightness in the presence of cooling.

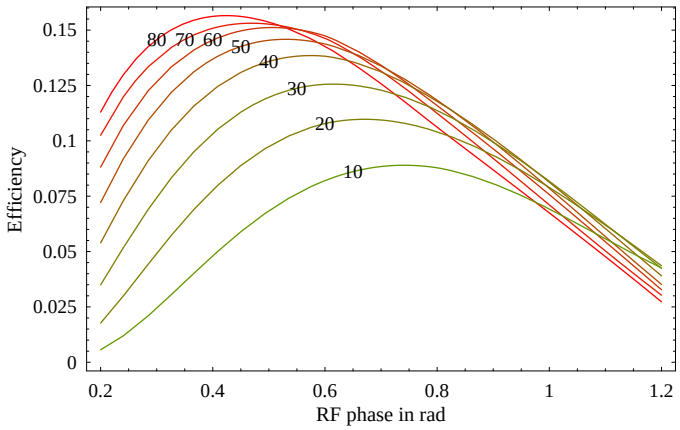


Figure 9.7: Scenario without cooling and phase rotation. Every line is described by frequency in MHz.

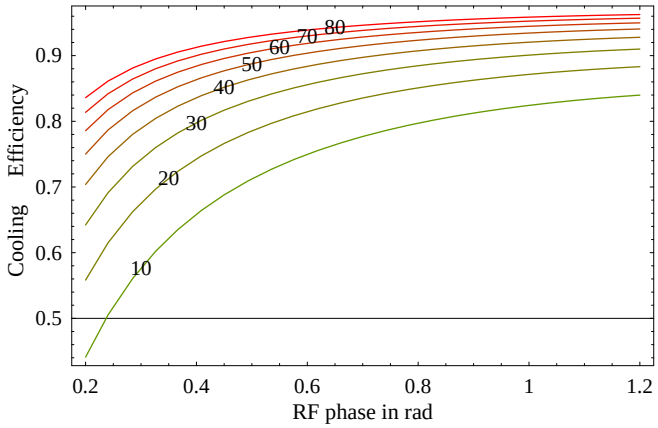


Figure 9.8: Loss factors in cooling. No transverse aperture restrictions are taken into account. Every line is described by frequency in MHz.

We see that with phase rotation and cooling we can end up with a similar number of muons for both the single frequency and second harmonic phase rotation scenarios. The second harmonic phase rotation case offers relatively short phase rotation section and larger transverse acceptances in the cooler and accelerator doe to use of lower frequency RF cavities.

| Scenario | Phase rotation | Cooling | Preacceleration |
|---|---|---|---|
| Single frequency Fig.9.2 | f | f | f |
| With second harmonic phase rotation Fig.9.3 | 2f | f | f |
| With cooling, without phase rotation Fig.9.4 | - | f | f |
| Without cooling, with single frequency phase rotation Fig.9.5 | f | - | f |
| Without cooling, with second harmonic phase rotation Fig.9.6 | 2f | - | f |
| Without cooling and without phase rotation Fig.9.7 | - | - | f |

Table 9.1: Frequency (f) in the RF systems used in various scenarios.

## 9.3 Design example

Fig. 9.9 shows a layout of the front end based on 87.4 MHz 4 MV/m phase rotation and 43.7 MHz 1.5 MV/m cooling as an example of the design with the second harmonic phase rotation. The decay solenoid is matched to the phase rotation with solenoidal focusing. The phase rotation consists of 16 0.9 m long cells. The solenoidal focusing enables a large averaged gradient to be kept in the phase rotation and a small phase advance per cell gives momentum acceptance. The phase rotation section is then matched adiabatically to the cooling ring and dispersions are matched with four bending magnets. For details concerning the cooling ring, see previous chapter. The Larmor beta function and dispersions in the part of muon front end till injection into the cooling ring are shown in Fig 9.10 and Fig 9.11 respectively. We assume 2 cm acceptance in the front-end, as dictated by the injection/extraction to the cooling ring. The acceptance of the proposed scheme could be increased by adding a linear pre-cooling section. To transform this design into a single-frequency case the length of the phase rotation should be properly adjusted as a function of frequency and voltage. Some details concerning the above design can be found in Table 9.2.

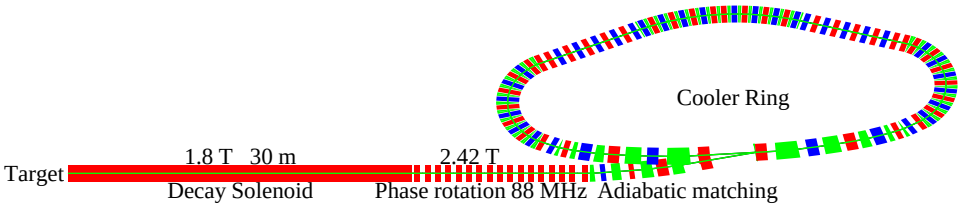


Figure 9.9: Layout of the muon front end

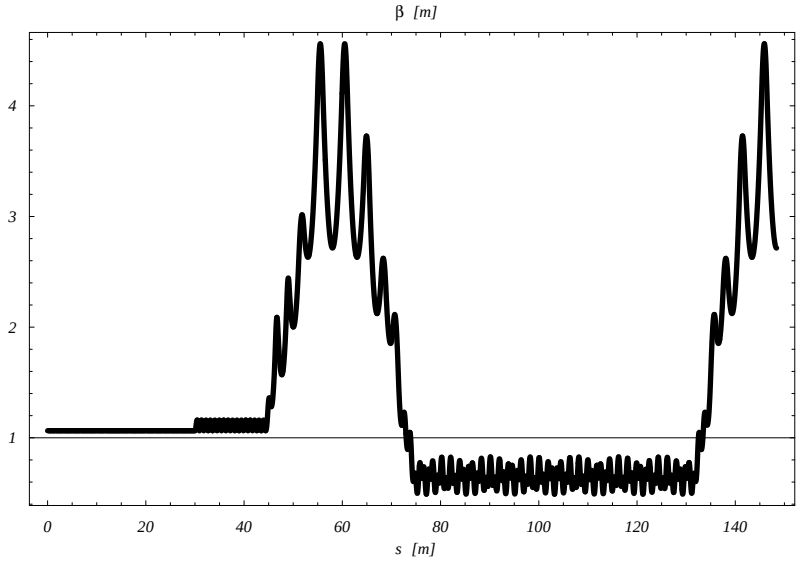


Figure 9.10: Larmor beta function in the front end including the RFOFO cooling ring.

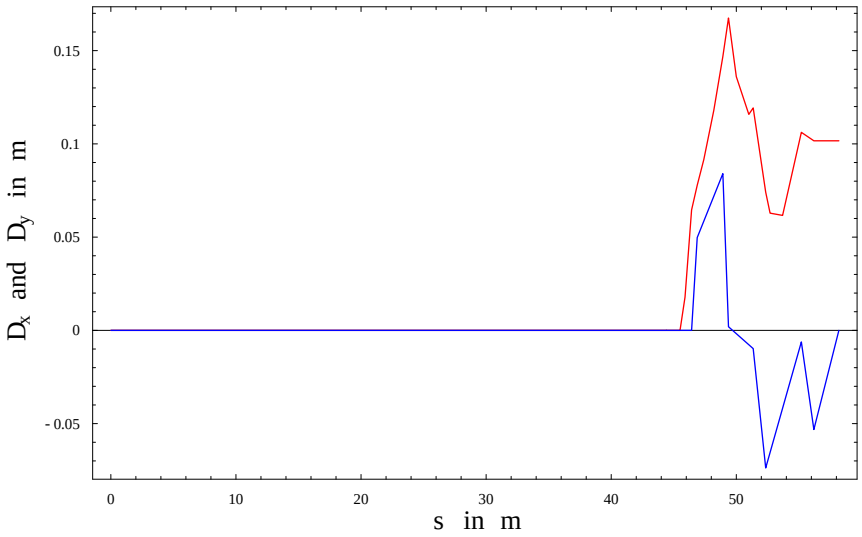


Figure 9.11: Dispersions in the muon front end from the target until the injection to the RFOFO cooling ring

| | |
|---|---|
| Length from the target till the cooling ring injection | 58.2 m |
| Cooling ring circumference | 90.1 m |
| Reference muon kinetic energy | 200 MeV |
| Momentum acceptance | +30/-20% |
| Rf frequency in the phase rotation | 87.14 MHz rad |
| RF frequency in the cooling ring | 43.57 MHz |
| Mean RF gradient in the phase rotation | 4 MV/m |
| Mean RF gradient in the cooling ring | 1.5 MV/m |
| Total transverse acceptance | 2 cm |

Table 9.2: Parameters of the front end with the second harmonic phase rotation.

# Chapter 10

# Conclusions

We have studied the muon front end of the neutrino factory based on RF phase rotation, magnetic compression and ionization cooling. We have described techniques for maximizing the performance of the longitudinal capture of muons at the end of the decay channel into stable RF buckets using the bunch-to-bucket principle or bunching the initial muon bunch into a string of microbunches. The proposed solution with bunching can produce a short muon train consistent with injection into a small cooling or accelerating ring.

Next we studied muon ionization cooling rings and in particular the RFOFO solenoidally focused ring with an adiabatic matching section, which seems to be very promising from the point of view of performance. The adiabatic matching enables to keep relatively long 4 m straight section, providing space for injection/extraction and is also a very interesting to achieve a broad momentum band acceptance. The implementation of wedge absorbers enables longitudinal motion during cooling to be stabilized. Further research on injection/extraction into the cooling ring is of great importance.

Then we studied the performance of the muon front end for various scenarios using the bunch to bucket principle, including decay losses in preacceleration to 2 GeV kinetic energy. However, the lack of detailed knowledge of pion production makes the final design of the muon front end still not possible. As an example we design a muon front end based on the second harmonic phase rotation and the cooling ring. The bunch-to-bucket principle allows an expensive bunching system to be avoided and a compact size to be kept. The transformation into the single-frequency scenario with phase rotation and cooling is straightforward. Both scenarios have similar performance. The single frequency offers faster cooling and acceleration, while the

second harmonic phase rotation case provides a better longitudinal capture and larger transverse acceptances in the cooler and acceleration due to the use of lower frequency RF system.

# Chapter 11

# Acknowledgment

I would like to acknowledge my special thanks to my supervisors: Dr B. Autin, who showed me a beautiful world of accelerator physics and Prof. J. Sobczyk for introducing me to neutrino physics. Many thanks to Prof. J. Łopuszański, Prof. J. Lukierski and Prof. J. Sobczyk, my physics teachers.

I owe thanks for many interesting discussions to members of CERN and other labs: B. Autin, K. Bongardt, C. Carli, F. Dydak, G. Franchetti, H. Haseroth, F. Gerigk, S. Gilardoni, M. Giovannozzi, P. Gruber, A. Lombardi, F. Meot, G. Rees, A. Sato, K. Schindl, H. Schonauer, A. Verdier and many others.

I am very grateful to K. Schindl for his continues encouragement and support. Special thanks to L. Ghilardi, S. Gilardoni, P. Shinnie and I. Waarum for their kind help during writing the thesis.

I want to thank my wife for her patience and say sorry to my little sons for these all late evenings and nights, when they were waiting for me.

The work was founded by Europen Organization for Nuclear Research, AB Department and Institute for Theoretical Physics, University of Wrocław.

# Chapter 12

# Appendix

Compressor line:
Q[0.4,0.704828]
SS[0.1]
Bend[1.2,0.51]
SS[0.1]
Q[0.4,-0.704828]
Sext[2.5]
Q[0.4,-0.704828]
SS[0.1]
Bend[1.2,0.37983]
SS[0.1]
Q[0.8,0.704828]
SS[0.1]
Bend[0.6,0.347356]
Sext[2.5]
Bend[0.6,0.347356]
SS[0.1]
Q[0.4,-0.704828]
Sext[2.45]
Q[0.4,-0.704828]
SS[0.1]
Bend[0.6,0.347356]
Sext[2.5]
Bend[0.6,0.347356]
SS[0.1]

Q[0.8,0.704828]
SS[0.1]
Bend[1.2,0.37983]
SS[0.1]
Q[0.4,-0.704828]
Sext[2.5]
Q[0.4,-0.704828]
SS[0.1]
Bend[1.2,0.51]
SS[0.1]
Q[0.4,0.704828]
Q[0.4,0.704828]
SS[0.1]
Bend[1.2,-0.51]
SS[0.1]
Q[0.4,-0.704828]
Sext[-2.5]
Q[0.4,-0.704828]
SS[0.1]
Bend[1.2,-0.37983]
SS[0.1]
Q[0.8,0.704828]
SS[0.1]
Bend[0.6,-0.347356]
Sext[-2.5]
Bend[0.6,-0.347356]
SS[0.1]
Q[0.4,-0.704828]
Sext[-2.45]
Q[0.4,-0.704828]
SS[0.1]
Bend[0.6,-0.347356]
Sext[-2.5]
Bend[0.6,-0.347356]
SS[0.1]
Q[0.8,0.704828]
SS[0.1]
Bend[1.2,-0.37983]

SS[0.1]
Q[0.4,-0.704828]
Sext[-2.5]
Q[0.4,-0.704828]
SS[0.1]
Bend[1.2,-0.51]
SS[0.1]
Q[0.4,0.704828]

SS[$l$] denotes a drift with length $l$ in m.
Q[$l$, $k$] denotes a quadrupole with length $l$ in m and focusing strength $k$ in $1/m^2$.
Bend[$l$, $\phi$] denotes a sector dipole with length $l$ in m and deflection $\phi$ in rad.

Lattice of half of the RFOFO ring:
SS[2]
Solenoid[1.,1.21156]
SS[0.75]
Bend[2.,0.1]
SS[0.75]
Solenoid[1,-1.289]
SS[0.5]
RF[2,43.5693,0.785398]
Bend[1.4,0.05]
RF[2,43.5693,0.785398]
SS[0.35]
Wedge[0.15, 0.5, 0.7]
Solenoid[1,1.38161]
RF[2,43.5693,0.785398]
SS[0.35]
Bend[0.8,0.1]
RF[2,43.5693,0.785398]
Wedge[0.095, 0.5, 0.7]
SS[0.255]
Solenoid[1,-1.69483]
RF[2,43.5693,0.785398]

SS[0.3]
Bend[0.4,0.07]
SS[0.3]
RF[2,43.5693,0.785398]
Solenoid[0.5,2.66413]
SS[0.25]
Bend[0.2,0.16]
Absorber[0.116]
SS[0.134]
RF[2,43.5693,0.785398]
Solenoid[0.5,-3.33899]
SS[0.3]
SS[0.2]
RF[2,43.5693,0.785398]
Solenoid[0.5,3.95276]
SS[0.075]
Bend[0.125,0.1122]
Bend[0.125,0.086695]
Absorber[0.075]
Solenoid[0.5,-3.95276]
RF[2,43.5693,0.785398]
SS[0.075]
Bend[0.125,0.086695]
Bend[0.125,0.086695]
SS[0.075]
Solenoid[0.5,3.95276]
SS[0.075]
RF[2,43.5693,0.785398]
Bend[0.125,0.086695]
Bend[0.125,0.086695]
SS[0.075]
Solenoid[0.5,-3.95276]
SS[0.075]
Bend[0.125,0.086695]
RF[2,43.5693,0.785398]
Bend[0.125,0.086695]
SS[0.075]
Solenoid[0.5,3.95276]

Absorber[0.075]
Bend[0.125,0.086695]
Bend[0.125,0.086695]
RF[2,43.5693,0.785398]
SS[0.075]
Solenoid[0.5,-3.95276]
SS[0.075]
Bend[0.125,0.086695]
Bend[0.125,0.086695]
SS[0.075]
RF[2,43.5693,0.785398]
Solenoid[0.5,3.95276]
Absorber[0.075]
Bend[0.125,0.086695]
Bend[0.125,0.086695]
SS[0.075]
Solenoid[0.5,-3.95276]
RF[2,43.5693,0.785398]
SS[0.075]
Bend[0.125,0.086695]
Bend[0.125,0.086695]
SS[0.075]
Solenoid[0.5,3.95276]
Absorber[0.075]
Bend[0.125,0.086695]
RF[2,43.5693,0.785398]
Bend[0.125,0.086695]
Absorber[0.075]
Solenoid[0.5,-3.95276]
SS[0.075]
Bend[0.125,0.086695]
Bend[0.125,0.086695]
RF[2,43.5693,0.785398]
SS[0.075]
Solenoid[0.5,3.95276]
SS[0.075]
Bend[0.125,0.086695]
Bend[0.125,0.086695]

Absorber[0.075]
RF[2,43.5693,0.785398]
Solenoid[0.5,-3.95276]
SS[0.075]
Bend[0.125,0.086695]
Bend[0.125,0.086695]
SS[0.075]
Solenoid[0.5,3.95276]
RF[2,43.5693,0.785398]
SS[0.075]
Bend[0.125,0.086695]
Bend[0.125,0.1122]
Absorber[0.075]
Solenoid[0.5,3.95276]
SS[0.2]
RF[2,43.5693,0.785398]
SS[0.2]
Solenoid[0.5,3.95276]
Absorber[0.1]
SS[0.1]
SS[0.2]
RF[2,43.5693,0.785398]
Solenoid[0.5,-3.95276]
SS[0.2]
SS[0.2]
Solenoid[0.5,3.95276]
RF[2,43.5693,0.785398]
SS[0.2]
SS[0.2]
Solenoid[0.5,-3.95276]
SS[0.2]
RF[2,43.5693,0.785398]
Absorber[0.1]
SS[0.1]
Solenoid[0.5,3.95276]
SS[0.2]
SS[0.2]
RF[2,43.5693,0.785398]

Solenoid[0.5,-3.95276]
SS[0.2]
SS[0.2]
Solenoid[0.5,3.95276]
RF[2,43.5693,0.785398]
Absorber[0.1]
SS[0.3]
Solenoid[0.5,-3.95276]
SS[0.2]
RF[2,43.5693,0.785398]
SS[0.2]
Solenoid[0.5,3.95276]
SS[0.2]
SS[0.2]
RF[2,43.5693,0.785398]
Solenoid[0.5,-3.95276]
Absorber[0.1]
SS[0.1]
Bend[0.125,0.0222821]
SS[0.075]
Solenoid[0.5,-3.95276]
RF[2,43.5693,0.785398]
Absorber[0.075]
Bend[0.125,0.0222821]
Bend[0.125,0.0222821]
SS[0.075]
Solenoid[0.5,3.95276]
SS[0.075]
RF[2,43.5693,0.785398]
Bend[0.125,0.0222821]
Bend[0.125,0.0222821]
SS[0.075]
Solenoid[0.5,-3.95276]
SS[0.075]
Bend[0.125,0.0222821]
RF[2,43.5693,0.785398]
Bend[0.125,0.0222821]
SS[0.075]

Solenoid[0.5,3.95276]
SS[0.075]
Bend[0.125,0.0222821]
Bend[0.125,0.0222821]
SS[0.075]
RF[2,43.5693,0.785398]
Solenoid[0.5,-3.95276]
SS[0.075]
Bend[0.125,0.0222821]
Bend[0.125,0.0222821]
Absorber[0.075]
Solenoid[0.5,3.95276]
RF[2,43.5693,0.785398]
SS[0.075]
Bend[0.125,0.0222821]
Bend[0.125,0.0222821]
Absorber[0.075]
Solenoid[0.5,-3.95276]
SS[0.075]
RF[2,43.5693,0.785398]
Bend[0.125,0.0222821]
Bend[0.125,0.0222821]
Absorber[0.075]
Solenoid[0.5,3.95276]
SS[0.0585]
Absorber[0.0165]
RF[2,43.5693,0.785398]
Bend[0.125,0.0222821]

RF[$V$, $f$, $\phi$] denotes a thin RF cavitie with field gradient $V$ in MV/m, frequency $f$ in MHz and phase $\phi$ in rad. Energy gain is calculated assuming cavity length of 1 m.
Absorber[$l$] denotes liquide hydrogen absorber with length $l$ in m.
SS[$l$] denotes a drift with length $l$ in m.
Solenoid[$l$, $B$] denotes a solenoid with length $l$ in m and field $B$ in T.
Bend[$l$, $\phi$] denotes a sector dipole with length $l$ in m and deflection $\phi$ in rad.
Wedge[$l$, $x$, $\phi$] denotes liquide hydrogen wedge absorber with length $l$ in m,

horizontal wedge angle $\phi$ in rad and $x$ is a maximal distance from beam azis in m, where the wedge angle is applied. At the larger distance absorber is again rectangular.

Phase rotation cell ( RF cavities not included):
SS[0.225]
Solenoid[0.45,2.4208]
SS[0.225]

Matching section between the phase rotation and the cooling ring:
SS[0.425]
Solenoid[0.45,2.4208]
SS[0.225]
Bend[0.4,0.0936439]
SS[0.525]
Solenoid[0.45,-2.4208]
SS[0.525]
Bend[0.8,0.00982522]
SS[0.725]
Solenoid[0.45,2.06095]
SS[0.625]
Bend[1,0.0520721]
SS[0.35]
Solenoid[1,1.21757]
SS[0.35]
Bend[1,0.0650729]
SS[1.5]
Solenoid[1.,1.21028]
SS[2]

# Bibliography


[1] Y. Fukuda at al., PRL 81 (1998), 1562.

[2] Q. R. Ahmad at al., PRL 89 (2002), 011301.

[3] K. Eguchi at al., PRL 90 (2003), 021802.

[4] S. M. Bilenky and S. T. Petcov, Rev. of Mod. Phys., Vol. 59, No. 3, Part I, 1987.

[5] Z. Maki, M. Nakagawa and S. Sakata, Prog. Theor. Phys. 28 (1962) 970.

[6] CERN Beams for Long Baseline Neutrino Experiments, A. Ball et al., CERN SL/Note 92-75(BT), 1992.

[7] P. Zucchelli, A Novel Concept for a Neutrino Factory: the Beta-Beam, Phys. Let. B 532(2002) 166-172.

[8] D. G. Koshkarev, CERN ISR/Note 74-62(DI), 1974.

[9] F. Dydak, Physica Scripta., Vol. T93, 91-97, 2001.

[10] S. Geer, Phys. Rev. D 57, 6989, (1998).

[11] M. Apollonio at al., Phys. Lett. B420 (1998) 397.

[12] A. Cervera at al., Golden measurements at a neutrino factory, hep-ph/0002108, 2000.

[13] Editor: M. Vretenar, Conceptual Design of the SPL, the High-Power Superconducting $H^-$ Linac at CERN, CERN 2000-012.

[14] H. Schonauer at al., Proton Drivers for Neutrino Factories, The CERN approach, CERN/NUFACT Note-046.

[15] Editor: K. McDonald, A Proposal for an RD Program for Targetry and Capture at a Muon Collider Source , P951, BNL 1998.
H. Kirk, Targetry at a Mu+Mu- Collider, THP34, PAC 1999.

[16] P. Sievers at al., A Stationary Target for the CERN-Neutrino-Factory, CERN/NUFACT Note-065.

[17] Fermilab Feasibility Study of a Neutrino Source Based on a Muon Storage, http://www.fnal.gov/projects/muon_collider/nu-factory/fermi_study_after_april1st/.

[18] The Neutrino Factory and Muon Collider Collaboration Feasibility Study II, http://www.cap.bnl.gov/mumu/studyii/ .

[19] H. Haseroth at al., CERN Ideas and Plans for a Neutrino Factory, CERN/NUFACT Note-045.

[20] S. A. Bogacz at al., Beam Dynamics of Muon Acceleration for Neutrino Factory, Proceedings of Nufact'02 Conference in London, 2002.

[21] K. R. Symon at al. Phys. Rev. Vol. 103 (1956), No 6, p. 1837.
E. Keil, A. M. Sessler, Muon Acceleration in FFAG, CERN/NUFACT Note-132.

[22] A. Verdier, Geometry of the Muon Storage Ring, CERN/NUFACT Note-13.

[23] L. D. Landau, E. M. Lifshitz, The classical theory of fields.

[24] H. Goldstein, Classical mechanics.

[25] E. D.Courant, H. S. Snyder, Theory of the Alternating-Gradient Synchrotron, Annals of Phys. 3, p. 1 (1958).

[26] J. Rossbach, P. Schmuser, Basic course on accelerator optics, Proceedings of CAS (1992), Fifth General Accelerator Physics Course.

[27] B. Autin at al., BeamOptics: A Program for Analitycal Beam Optics, CERN-98-06.

[28] H. Wiedemann, Particle Accelerator Physics.

[29] F. Willeke, G. Ripken, Methods of beam optics, AIP Conference Proceedings.

[30] G. Franchetti, Solenoidal Channels Linear Dynamics, CERN/NUFACT Note-73.

[31] V. Veksler, J. Phys. USSR 9 (1945), 153.

[32] E. M. McMillan, Phys. Rev. 69 (1945), 143.

[33] P. Lapostolle and M. Weiss, Formulae and Procedures Useful for the Design of Linear Accelerators, CERN-PS-2000-001(DR).

[34] G. E. Lee-Whiting, NIM 83 (1970), p. 232.

[35] NufactJ Feasibility Study, http://www-prism.kek.jp/nufactj/index.html.

[36] D. Neuffer, High-Frequency Buncher and Phase Rotation for the Muon Source, Fermilab Neutrino Factory/Muon Collider Note-0181.

[37] M. G. Catanesi at al., Proposal to Study Hadron Production for the Neutrino Factory and for the Atmospheric Neutrino Flux, CERN/SPSC-99-35.

[38] N. V. Mokhov, The MARS Code System User's guide, Fermilab-FN-628(1995).

[39] S. Gilardoini at al. Updated Results of the Horn Study for the NuFact, CERN/NUFACT Note-42.

[40] J. D. Jackson, Classical electrodynamics, ch. 12.

[41] B. Autin, F. Meot, A. Verdier, Efficiency of an Alternating Gradient Muon Collection Channel, CERN/Nufact Note-128.

[42] W. D. Kilpatrick, Rev. of Scient. Istr. Vol 28, No. 10, p. 824 (1957).

[43] B. Autin, NIM A 503 (2003), p.363 (2003).

[43a] B. Autin at al., Pion and Muon Densities in Decay Channel, Proceedings of Nufact'03 Conference in New York, 2003.

[44] A. Lombardi, A 40-80 MHz system for Phase Rotation and Cooling, CERN/NUFACT Note-034.

[45] R. Garoby, F. Gerigk, Cavitie Design for the CERN Muon Cooling channel, CERN/NUFACT Note-87.

[46] T. O. Raubenheimer, P. Emma, S. Kheifets, Chicane and wiggler based bunch compressors for future linear colliders, SLAC-PUB 6119, 1993.
T. E. D'Amico, G. Guignard, T. Raubenheimer, CLIC Note No.2, 1998.
B. Autin at al., Varying the path length of charged particles using wiggler modules, CERN-Nufact Note-069.

[47] B. Autin at al. NIM A 503 (2003), p. 369.

[48] J. Pasternak, J. Phys. G: Nucl. Part. Phys. 29 (2003) p. 1667.

[49] G. Rees, Muon Front End Chicane and Acceleration , Proceedings of Nufact'02 Conference in London, 2002.

[50] G. Rees, Muon Front End Studies at RAL, Proceedings of Nufact'03 Conference in New York, 2003.

[51] A. N. Skrinsky, Proc. XXth Int. Conf. on High Energy Phys., A. I. P. Conf Proc. 68, 1056 (1980).

[52] Particle Data Group, Phys. Rev. D Vol. 66 No. 1-I (2002).

[53] V. Balbekov, Ring Cooler Update, Fermilab Neutrino Factory/Muon Collider Note-0189.
V. Balbekov, Solenoid Based Ring Coolers, Fermilab Neutrino Factory/Muon Collider Note-0232.
J. S. Berg, R. Fernov. R. B. Palmer, An Alternating Solenoid Focused Ionization Cooling Ring, Fermilab Neutrino Factory/Muon Collider Note-0239.
Y. Fukui at al. Muon Cooling Rings for the $\nu$ Factory and $\mu^+\mu^-$ Collider, Fermilab Neutrino Factory/Muon Collider Note-0262.

[54] R. B. Palmer at al., An Induction Kicker for Muon Cooling Rings, Fermilab Neutrino Factory/Muon Collider Note-0256.

[55] Wolfram Research Inc., www.wolfram.com